CHAPTER 1

INTRODUCTION

This chapter consists of the overall discussion on the mercury issues in which the research topic is concerned, the aims, motivations, as well as the outline of the research scope.

1.1 Mercury

An early document filed about mercury can be related to the death of Emperor Ying Zheng (259-210 BC) that founded the Chinese imperial system and fascinates people with the gigantic Great Wall, the terra-cotta warriors, and horses in China. He was reportedly died of gulping down mercury pills which were believed to lead him an immortal life (Zhao, Zhu, & Sui, 2006). It cannot be denied that the existence of this element has led a long historical lifetime. Mercury with the symbol Hg and atomic number of 80 is also known as quicksilver or hydrargyrum. Mercury has a silvery white colour which freezes into a soft solid at -38.87 °C and boils at 356.9 °C ("Mercury (Hg)," 2011). Being placed in the d-block in periodic table, it is an unusual transition metal which is liquid at room temperature and pressure. It is notable that mercury has high vapor pressure at room temperature (1.9×10^{-3} torr) and the only element that can exist as a monoatomic vapor besides noble gasses (Greenwood & Earnshaw, 1984; Hutchison & Atwood, 2003).

Mercury exists in three different forms: elemental- Hg^0 (zero valent), inorganic- Hg_2^{II} (Hg^I) (monovalent), and Hg^{II} (divalent) as well as organic- RHg. It is interesting to note that the monovalent oxidation state is only found as the diatomic Hg_2^{II}, and never straight as Hg^I (Hutchison & Atwood, 2003). **Table 1.1** summarizes the key properties, transport and fate of different forms of mercury in the environment. In aquatic systems,

mercury exists in elemental, inorganic, and organic forms. Elemental mercury (Hg^0) has high volatility and relatively low water solubility. Aqueous inorganic mercury has two valences, +1 and +2, however mercury with +2 is more widely spread in the environment. Hg(II) consists of both Hg^{2+} free ions and Hg^{2+}complexes. Chloride, hydroxide, sulfide, dissolved organic matter, and other chemicals are found in Hg^{2+} complexes. Aqueous organic mercury can be divided in 2 categories: covalently-bonded organomercurials (methylmercury and dimethylmercury) and mercuric complexes with organic matter (humid substances) (Wang, Kim, Dionysiou, Sorial, & Timberlake, 2004).The common mercury transformation is as below (Okoronkwo, Igwe, & Okoronkwo, 2007):

$$Hg^0 \underset{\text{reduction}}{\overset{\text{oxidation}}{\rightleftharpoons}} Hg^{+1} \text{ or } Hg^{+2} \underset{\text{demethylation}}{\overset{\text{methylation}}{\rightleftharpoons}} HgCH_3 / HgCH_3Hg$$

Table 1.1: Key properties, transport and fate of different forms of mercury (EPA, 1999).

Forms	Elemental or metallic (Hg^0)	Divalent or mercuric (Hg^{2+})	Methylmercury (CH_3Hg^+)
Key Properties	• 95 % of atmospheric mercury is Hg^0 vapor	• Bound to airborne particles • Comprises 5 % of atmospheric mercury • Found in soil and water as a number of complex ions • May form inorganic mercuric salts	• Lipophylic ion produced by bacteria in the water column or sediment • Nearly all mercury in fish is methylated.
Transport and fate	• Tends to remain airborne • Not easily deposited • May travel long distances before conversion to other forms and deposition	• Easily deposited to Earth's surface in dry form or in precipitation • Once in water, may volatilize or partition intoparticulates and be transported to sediment.	• Enters food chain through aquatic biota and uptake into fish tissue • Bioaccumulates as it travels up the food chain, reaching highest concentrations in organisms at highest trophic level.

Mercury also shows a distinct tendency to form strong bonds with sulfur, to the extent that thiol compounds are sometimes known as mercaptans ("mercury capturing"). This can at least partially be explained by the hard soft acid base (HSAB) concept. Sulfur is a quintessential soft base and mercury is one of the best examples of a soft acid (it has even been argued that the methyl mercury ion serves as the "soft" equivalent of the "hard" proton). Therefore, it is expected that mercury and sulfur species would form stable compounds (Hutchison & Atwood, 2003).

Where does mercury come from? Mercury can come from two different sources, *i.e.* natural and anthropogenic sources. **Figures 1.1** and **1.2** depict the evaluation of global mercury emissions by natural and anthropogenic sources (Pirrone, et al., 2010). Among the natural sources, it is obvious that ocean is the main contributor for global mercury emission. On average, coastal waters and Mediterranean Sea have the highest evasional flux, 1.83 and 1.96 ng m^{-2} h^{-1}, respectively (Hedgecock, Pirrone, Trunfio, & Sprovieri, 2006; Pirrone, et al., 2003). Mason reported recent estimates of total mercury evasion from ocean basins and lakes, which account for 2778 Mg yr^{-1} (37 % GEb) of net gaseous mercury evasion to the atmosphere (Mason, 2009). Numerous studies pinpoint that the evasion of elemental mercury from surface waters is primarily driven by (i) concentration gradient of mercury between the top-water microlayer and air above the surface water, (ii) solar irradiation which is responsible for the photo-reduction of oxidized mercury in the top-water microlayer, and (iii) the temperature of the top-water microlayer and air above the surface water (air-water interface) (Hedgecock, et al., 2006; Pirrone, et al., 2003; Pirrone, Sprovieri, Hedgecock, Trunfio, & Cinnirella, 2005). Mercury emission from biomass burning was reported as the second largest contributor after oceans in year 2008. The most recent estimate suggests that about 675 Mg of mercury is released to the atmosphere from biomass

burning every year, (annual average for the period 1997-2006), which accounts for 13 % of the total contribution from natural sources (Friedli, Arellano, Cinnirella, & Pirrone, 2009). On the other hand, the factors which have influenced the mercury emissions from top soil and vegetation are meteorological conditions, historical atmospheric deposition, as well as the type of vegetation and top soil (Pirrone, et al., 2010). According to Rea et al., 2002, mercury emissions from vegetation depend on the mercury uptake from the atmosphere, atmospheric deposition to foliage and mercury uptake from roots (Rea, Lindberg, Scherbatskoy, & Keeler, 2002). Summarizing all the net mercury fluxes from all regions (Forests, Tundra/ Grassland/ Savannah/ Prairie/ Chaparral, Dessert/ Metalliferous/ Non-vegetated Zones and Agricultural areas), the total net global mercury evasion is estimated 1464 Mg yr^{-1} in 2008. Mercury emissions from natural processes (primary mercury emissions-reemissions), including mercury depletion events, is expected to be 5207 Mg yr^{-1}, which constitutes about 4 % of the total mercury emissions from natural sources in 2008. Meanwhile, the contribution from volcanoes varies over time depending on the degassing or eruption phase (Pirrone, et al., 2010). In general, volcanoes and geothermal activities emit nearly 90 Mg yr^{-1} of mercury to the atmosphere (Mason, 2009). Mercury emissions from calderas are important natural source of mercury, for instance, the Phlegrean fields (Pozzuoli, Italy) show fluxes of mercury, as Hg-S complexes, in the range of 0.9 to 19 g day^{-1} (Bagnato, Parello, Valenza, & Caliro, 2009; Ferrara, Mazzolai, Lanzillotta, Nucaro, & Pirrone, 2000). In summary, the global mercury emission by natural sources in 2008 is estimated at 5207 Mg yr^{-1}.

On the contrary, mercury is also discharged from man-made sources to the atmosphere which embraces fossil-fuel fired power plants, gold mining production, ferrous and non-ferrous metals manufacturing, caustic soda production, cement production, vinyl

chloride monomer (VCM) production, medical and industrial waste. The parameters employed to estimate mercury emission from anthropogenic sources are: the bulk material amount, mercury content of the material and the technology adopted to reduce emissions (Pirrone, et al., 2010). Fossil fuel-fired power plants are the largest mercury contributor to the atmosphere. World coal consumption in 2006 was 6118 Tg, responsible for the primary fuel used in electrical power generation facilities (42 %) and attributed for about 27 % of world's energy consumption (EIA: International Energy Outlook 2009, 2009). Wood waste is primarily used to produce heat in the industrial sector, while wood is burned in wood stoves in the residential areas with no emission control in most of the developing countries (Mukherjee, Bhattacharya, Sarkar, & Zevenhoven, 2009). Oil burning as part of the fossil fuels category has also contributed to mercury emissions to the atmosphere. The top five countries which are using oil for power generation comprises of USA, Japan, Russia, China, and Germany. Bulky volumes of distillate and residual oils are burned each year to accommodate the worldwide consumption for electric utilities, commercial and industrial boilers, as well as residential boilers (Pirrone, et al., 2010). Fuel oils contain mercury with concentrations that vary with crude oil type (Wilhelm, 2001). The values are in the intervals between 0.007 to 30 g Mg^{-1}, with a typical value of 3.5 g Mg^{-1} (Mukherjee, et al., 2009; Wilhelm, 2001). It can be envisaged that mercury concentrations in residual oils are higher than those found in distillate oils and the heavier the refinery fractions, the higher the mercury contents (Pirrone, et al., 2010). Natural gas might contain small amount of mercury but it is usually eliminated from the raw gas during the recovery of liquid constituents and hydrogen sulfide removal processes. Hence, it can be assumed that mercury emissions from natural gas combustion are insignificant comparing to other sources (Pirrone, Keeler, & Nriagu, 1996; Pirrone, et al., 2001). The release of mercury

from artisanal and gold mining activities is one of the significant environmental issues as most of the activities are carried out in developing countries. The estimation mercury released from this industry is 17 % out of the total of 2320 Mg yr^{-1}. Whilst, smelting processes to produce metals such as copper, zinc, lead, nickel, as well as gold are believed to be one of the largest mercury contributors, especially in developing countries (Telmer & Veiga, 2009; UNEP, 2002). Combustion temperatures in the smelting boilers, furnaces and roasters are key aspects affecting the amount of mercury discharged into the atmosphere. In cement kilns, coal combustion is also a major source of mercury emissions. The estimation of mercury emissions from this particular source is based on an emission factor of 0.1 g per Mg of cement produced (Pacyna, Pacyna, Steenhuisen, & Wilson, 2006) and an annual cement production of 2315 Gg (2005), which leads to 236 Mg yr^{-1} (10 % of total anthropogenic sources) of mercury emitted to the atmosphere. Besides that, about 135 chlor-alkali plants using mercury cell technology were operated worldwide in 2007, although most of the plants have phased out the application of this technology and have been substituted with membrane technology (Mukherjee, Zevenhoven, Brodersen, Hylander, & Bhattacharya, 2004; World Chlorine Council, 2007). In chlor-alkali plant, mercury can be released from the mercury cell process through emissions to the air, discharge of waste waters and solid wastes. The estimation of mercury emissions from this sector is 163 Mg yr^{-1}, which is 7 % of the total mercury contribution from anthropogenic sources (Mukherjee, et al., 2009; Streets, Hao, Wang, & Wu, 2009). Primary mercury production is also another direct source of mercury emission to the atmosphere. Currently, most of the primary mercury mines are located in Algeria, the People's Republic of China, Kyrgzstan, and Spain in order to cater the vast mercury demand, while Italy, Mexico, Slovakian, Slovenia and Turkey reserve as a consequence of former mining activities. In

2000, approximately 1800 Mg of mercury were produced (Maxson, 2006) which led to global mercury emissions of 50 Mg yr^{-1} (Pirrone, et al., 2009). Apart of the major mercury emissions from the aforementioned industrial sectors, mercury is also emitted through cremation, agricultural activities, and other minor uses (Maxson, 2004; UNEP, 2002).

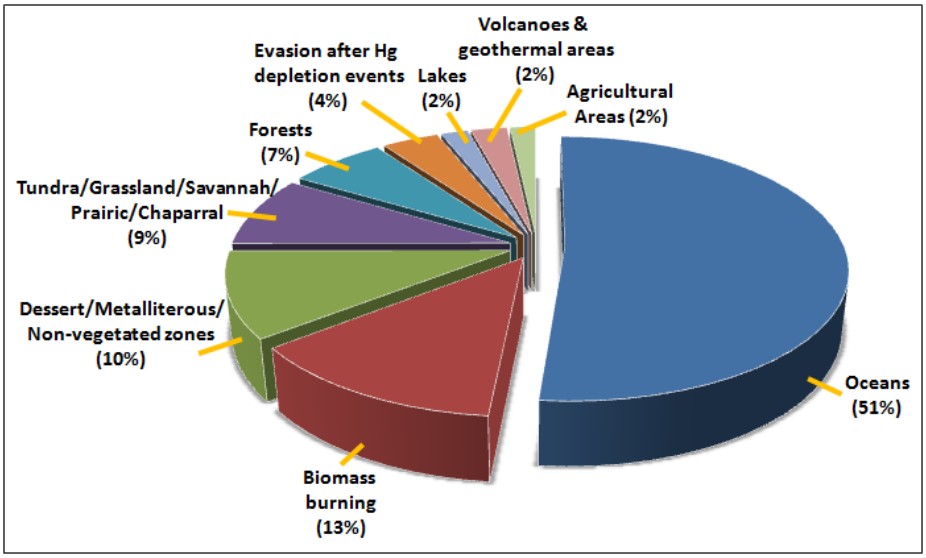

Figure 1.1: Global mercury emissions from natural sources in 2008.

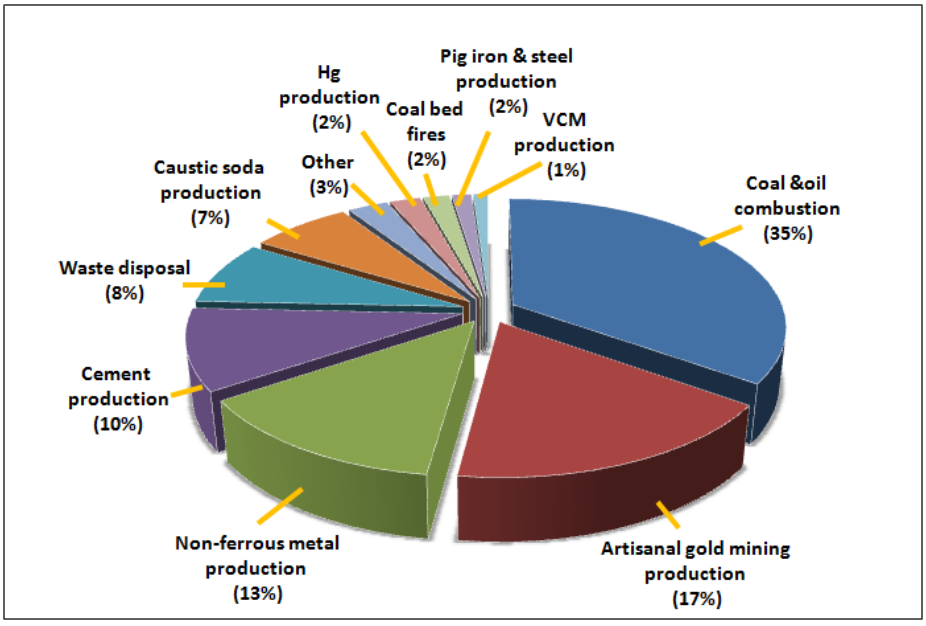

Figure 1.2: Global mercury emissions from anthropogenic sources in 2008.

1.2 Applications of Mercury

Mercury is found to encompass a diverse number of applications since the past few decades. Mercury is believed to have been used to extract precious metals, such as gold, silver, and other metals from ores as early as 2700 BC (Malm, 1998). Due to its uniform thermal expansion and contraction, mercury is an ideal thermometric medium for thermometers. It has also been widely used as barometers and manometers for pressure measurement (Charlton, et al., 1994).

Another vital industrial application of mercury is the lighting industry where most fluorescent lamps use mercury vapor, along with an inert gas, convert electrical discharge to useful light. The mercury is excited by the electron flow between the electrodes and radiates in UV region. This UV radiation excites in turn the phosphorescent material coating the bulb, generating visible light (Finn & Ouellette, 1992; van Dijk, Hartgers, Jonkers, & van der Mullen, 2000). Besides that, mercury is also an important component in electrolytic cells, widely used in the Chlor-alkali industry. In the Chlor-alkali plant, mercury serves as an anode in the electrolysis of brine which converts the sodium cations to sodium metal, amalgamates the sodium, and carries it into another reaction vessel, where it reacts with purified water to form sodium hydroxide (Swaddle, 1997).

On top of that, mercury cell batteries were also once extensively flooded in the market. In a typical mercury cell battery, it consists of a mercury/ zinc amalgam as the anode and a mercuric oxide/ graphite cathode. Mercury can also be found in zinc-silver cell batteries (normally used in watches), where a mercury/zinc amalgam forms the anode (Jones, McGugan, & Lawerence, 1977/1978).

Moreover, organomercurials have been broadly used as pesticides (Murphy & Aucott, 1999) or fungicide for the treatment of seeds. The catastrophic incident which

occurred in Iraq in the late 1960's to early 1970's was a concrete proof of mercury poisoning due to the application of methyl mercury as fungicide during the transport of 'wonder wheat' from Mexico to Iraq. Moreover, mercury is also added to paints as fungicide (Sunderland & Chmura, 2000) and pharmaceuticals as an antimicrobial/ antibacterial agent (Márquez, Silva, & Perez-Bendito, 1988). In addition, mercury is also present as thimerosal (sodium ethylmercurythiosalicylate) in contact lens solutions and vaccines (Procopio, Silva, Asensio, Sevilla, & Hernandez, 1992). Furthermore, mercury is also well known for its application in dental industry. It can easily form amalgam with silver, copper, or other metals to build dental fillings.

Recently, VCM is also found to be one of the major components in contributing global mercury demand. This can be seen in the pie chart (Pirrone, et al., 2010) in **Figure 1.3** where the demand of mercury for VCM industry has shot up to 21 % in 2005 with insignificant contribution in year 2000. VCM is an intermediate feedstock in manufacturing polyvinyl chloride (PVC). There are two processes employed to manufacture vinyl chloride, one of them is the acetylene process which uses mercuric chloride on carbon pellets as a catalyst, while the other does not involve the use of mercury (Pirrone, et al., 2010). The pie charts shown in **Figure 1.3** illustrate the global mercury demand in year 2000 and 2005. Although some of the industries such as batteries and chlor-alkali sectors have demonstrated a gradual decrease in the usage of mercury from year 2000 to 2005, there are still other industries like VCM, gold and mining sectors which have contributed significantly to the mercury demand in year 2005.

Although mercury has found a diverse range of applications throughout the past, mercury pollution is still a serious and enduring menace not only to the environment, but also to the organisms especially along the food chain. Consequently, policy makers have to

take advantage on the updated information about the global mercury emissions from time to time in view of the adverse effects of this highly toxic pollutant on human health and ecosystems.

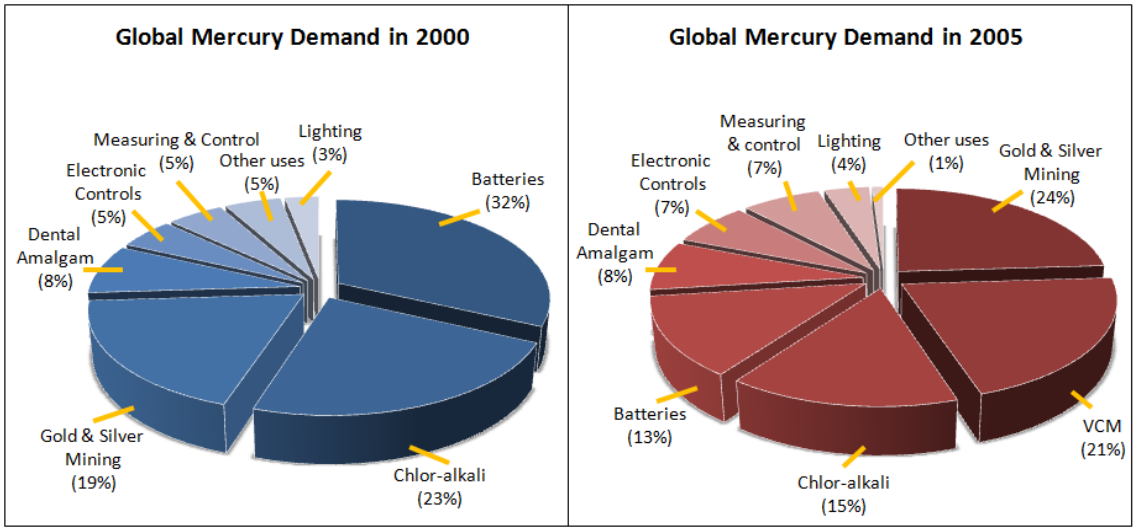

Figure 1.3: Percentages of global mercury demand by use category in 2000 and 2005. Global demand was 3386 Mg and 3415 Mg respectively in 2000 and 2005 (from Maxson (2004) and UNEP (2006)).

1.3 Impacts of Mercury

In this particular section, the impacts of mercury will be highlighted. Two key aspects need to be focused here when discussing the impacts of mercury exposures, namely the ecosystems (humans, organisms and environment), as well as the industry sector. One of the important aspects of the impact of mercury to the environment is its ability to build up in the organisms and along the food chain. Methylmercury is the most vulnerable mercury form which can be easily absorbed and accumulated along the food chain in comparison to other forms of mercury. Inorganic mercury can also be absorbed, but in a much slower rate and lower efficiency than methylmercury (US EPA, Dec 1997). The progressive build up of methylmercury has a significant effect on the impact of animals and humans. Fish and some of the seafood are found to bind methylmercury strongly and most of the

methylmercury in fish tissue is covalently bound to protein sulfhydryl groups. Mercury concentrations in individuals of a given fish species tend to increase with age as a result of slow elimination of methylmercury and increased consumption, particularly with larger size fish. Older fish usually have higher mercury concentrations in the tissues than younger fish of the same species. At the top levels of the aquatic food web are fish-eating species, such as humans, seabirds, seals and others which is typically prone to the threat of methylmercury. Methylmercury is a central nervous system poison and the kidneys are the most susceptible organ to the damage from inorganic mercury. Neurological impairment were already seen in animals from the catastrophic Minamata phenomenon (1956), prior to the identification of mercury poisonings found on humans, where birds were found to experience difficulty in flying besides showing signs of abnormal behaviours. Serious effect is also found on reproduction due to mercury poisoning as methylmercury leads to risk in developing fetus since it can readily cross the placenta barrier and destroy the developing nervous system (UNEP, 2002).

The toxicity of mercury depends on its chemical form, and symptoms are quite different with regards to the exposure to elemental mercury, inorganic mercury compounds or organic mercury compounds. For alkylmercury compounds, primarily methylmercury, is highly toxic, and the nervous system is the greatly affected system. In adults, non-specific symptoms like paresthesia, malaise, and blurred vision can be detected at early stage of methylmercury exposure. The signs appear, such as concentric constriction of visual field, deafness, dysarthria, ataxia, coma, and ultimately death with growing exposures (Harada, 1995). Meanwhile, for infants with highly exposures during pregnancy can result in microcephaly, hyperreflexia, gross motor, mental impairment, and sometimes coupled with blindness or deafness (Harada, 1995; Takeuchi & Eto, 1999). In milder cases, the

symptoms become more apparent later during the development as psychomotor and mental impairment, as well as persistent pathological reflexes (Methylmercury, 2000; WHO/IPCS, 1990). A report of methylmercury poisoning due to Minamata disease which occurred in Minamata, Japan claimed that the overall prevalence rate for the Minamata region for neurological and mental disorders was 59 %. Most of the affected adults were suffering from paresthesia, ataxia, sensory disturbances, tremors, hearing impairment and difficulty in walking. In the extensive studies of congenital Minamata disease, severe disturbances of nervous function were mentioned, and the affected offsprings were very late in reaching developmental milestones (Boca Raton, 1997; Harada, 1995; Tsubaki & Takahashi, 1986; WHO/IPCS, 1990). Nevertheless, exposure to elemental and inorganic mercury can lead to neurological, renal, neoplastic (cancer), respiratory, cardiovascular, body immunity, reproductivity and genotoxicity effects in humans. The most important source of elemental mercury for the general population is dental amalgam, but exposure at work may sometimes exceed this by many times. For inorganic mercury compounds, diet is the important source for the majority of people. The use of skin-lightening creams and soaps that contain mercury and use of mercury in traditional medicine can also lead to substantial exposures to inorganic or elemental mercury (UNEP, 2002).

Although the adverse impacts of mercury exposures towards the entire ecosystems which include the food chains, food webs and the environment are catching global concerns, the impacts of mercury emissions towards the industry sector should not be neglected. In some of the industrial sectors, mercury compounds are labeled as the culprit in demolishing their profit margins. Mercury is found in nearly all oil and gas reservoirs. For instance in oil and gas industry, mercury compounds can present as many forms in some crude oils, namely, elemental mercury, mercuric chloride, mercuric sulfide, mercuric selenide,

dimethylmercury, diethylmercury, and etc. In most of the oil and gas reservoirs, elemental mercury can cause corrosion/ embrittlement with the metal made reactors. The mechanisms involved are amalgamation, amalgam corrosion, liquid metal embrittlement, and galvanic corrosion. Mercury can cause damage on aluminium heat exchangers, usually used in LNG plants, cryogenic hydrocarbon recovery plants, and petrochemical plants. It can also concentrate and drop out as liquid in the colder sections of the plant which lead to difficulty in plant maintenance. Several production plants experienced sudden heat exchanger failures resulting in plant shutdowns, repairs, fires, and even explosions (Markovs & Clark, 2005). Skikda explosion which occurred in Skikda, Algeria, is a concrete evidence of mercury corrosion at liquefaction plant resulting in the rupture of tubes used in heat exchangers and the specific plant had to shut down. On top of that, mercury also tends to contaminate gas treatment processes such as molecular sieve and glycol dehydration units, chloride removal systems, as well as acid gas removal systems. In the petrochemical plants, mercury can deactivate downstream catalyst and poison catalysts in ethylene, aromatics and olefins manufacture (Visvanathan, 2003). Even sometimes mercury can present at very low concentrations, its presence in the feedstock and accumulates on the catalyst can result in permanent (irreversible) poisons on precious metals, such as palladium supported on alumina catalyst which is commonly used for selective hydrogenation of acetylenes. Catalyst poisoning is known to decrease production yields and shorten catalyst lifetime. Therefore, it is viable that a vigilant mercury removal system is designed to avoid unnecessary accident and economical loss in the aforementioned production plants.

1.4 Mercury Remediation

It is now appropriate to consolidate the ideas of mercury remediation after the detailed discussion of mercury impacts in preceding section. Numerous remediation technologies have been introduced for the past few decades since mercury menace is not a common issue nowadays. The remediation technologies applied vary with the mediums where mercury is found in. In general, mercury can exist in different mediums, such as air, soil, oil, gas, as well as water (ocean, river, lake, and waste water) systems. Interestingly, a novel route for eliminating mercury from crematoria exhaust in Sweden is the addition of a selenium ampoule to the casket. The statistical analysis shows that less mercury was emitted from the coffins treated with selenium and a controlled simulation (with selenium and mercury amalgam but no cadaver) implies that about 85 % of mercury is bound by the process (Hogland, 1994).

Conventionally, the remediation method used for contaminated soils is excavation and disposal. The contaminated soil is manually removed and deposited in a landfill (it may leach back into the environment), roasted, or washed to recover the mercury (Hong Kong Environmental Protection Department, 2002; STS Consultants; Vector Group Inc.). Phytoremediation, the use of plants to clean up pollution, is also a good remediation idea where a species of plant life is introduced and cultivated onto the contaminated area in this process. The plants habitually absorb the contaminants via their root system, and either detoxify or sequester them after a period. This technique has already widely exploited to clear out contaminated sites by organic contaminants (TNT, PCP, trichloroethylene), and metals (cadmium, nickel, and lead) (Macek, Macková, & Kás, 2000; Meagher, 2000). Yet, mercury imposes a major safety issue as it is toxic to most plants and humans as well. Hence, many species could not survive long enough to remediate the mercury contaminants in the

polluted sites. However, one example-water hyacinth (Riddle, Tran, Dewitt, & Andrews, 2002) found which can safely hyperaccumulate mercury and studies shown that these plants can accumulate up to 4435ppb mercury in their roots and 852 ppb mercury in their shoots. It is believed that the mercury accumulates in the roots, where it is bounded by carboxylate molecules; partial mercury migrates to the shoots, where it is bounded by sulfur biochelates. Nevertheless, the problem is still retained as the mercury-saturated plants which contain toxic waste are still the issues (Hutchison & Atwood, 2003).

In addition, bioremediation (use of microscopic organisms to clean up contamination) appeared as a promising route to remediate the polluted sites. Some bacteria are believed to convert inorganic and methyl mercury to elemental mercury. In the literature, a system has been developed for the bioremediation of waste water streams emanating from chlor-alkali plants (Wagner-Döbler, von Canstein, Li, Timmis, & Deckwer, 2000). This process is relatively cheap and has been found to effectively remove mercury from water streams. However, the mercury concentration in the wastewater must be regulated as if the concentration is too high, it can overpower the bacteria's defence system and kill them. Furthermore, this technique needs an extensive reactor setup and as a result it is not suitable for in situ remediation. Another method is to modify bacteria by genetic engineering of polyphosphate kinase (ppk) gene into some bacteria that already contained the mercury transport mer genes but not the reduction enzyme (Pan-Hou, Kiyono, Kawase, Omura, & Endo, 2001). Principally, the bacteria were engineered to replace the merA enzyme, so that when mercury levels were increased tremendously within the bacteria, polyphosphate was synthesized. The phosphate chelated the mercury and prevented it from interfering with the processes within the cell. This way, the treated bacteria has the ability to hyperaccumulate the metal without itself affected. Although this is an excellent filter system, it faces similar

problems as other filters, which is it could be saturated and would have to be replaced. Another vital point is that bio-accumulating bacteria are perhaps not a good choice for in situ remediation as they will involve in the local food chain and could in fact increase the bioactivity of the mercury (Hutchison & Atwood, 2003).

The suggestion to remediate a mercury waste site is not only limited to the disciplines of phyto- and bio-remediation, but it also engrosses the area of filtration. A few points concerning the filtration methods should be highlighted before a comprehensive discussion begins. Filtration methods involve either physically or chemically absorbing mercury to the filters and the filters will be saturated eventually. As a result, they will have to be either replaced or regenerated (Hutchison & Atwood, 2003). The typical mercury sorbent is activated carbon and it is reasonably effective at purifying vapor streams, but it is quite poor for aqueous mercury waste (Gash, et al., 1998; Hollerman, et al., 1999). A better sorbent for aqueous mercury waste is ion exchange resin which utilizes sulfur based group to bind mercury. An assessment of these resins was carried out to find that most resins tested were superior to the carbon (Hollerman, et al., 1999). One of the examples of the most effective resin is believed to be TMR (for Total Mercury Removal) from *Rohm and Haas* (Dujardin, Cazé, & Vroman, 2000). It is a styrene-divinylbenzene copolymer with pendant aryl thiol groups and it has the ability to adsorb 0.7 g of mercury per gram of resin. After the saturation is reached, the resin can be regenerated by treatment with concentrated hydrochloric acid (Hutchison & Atwood, 2003). However, this introduces a problem where a new batch of mercury contaminated waste is created after the treatment with hydrochloric acid and the disposal of this secondary waste could be costly. Therefore, an attempt to curb this problem has been done by regenerating the filters via a thermally activated redox reaction (Gash, et al., 1998). When a solution containing Hg^{II} is passed through the ion

exchange compounds of the formula Li_xMS_2, it formed a black compound with the formula of Hg_yMoS_2. Upon heating to 425 °C, the mercury was released as mercury vapor (trapped for reuse or disposal) and MoS_2 was left behind and this could be reactivated with n-butyl lithium and reused. Another effective filter design is the use of functionalized mineral or mineral-like matrixes as filters and the well known matrix is mesoporous silica (X. Feng, et al., 1997; Nooney, Kalyanaraman, Kennedy, & Maginn, 2001). The filter is designed in such a way that the silica is treated with mercapto or chloroalkyl trimethyl silanes to functionalize them. This compound is proved very good at purifying simulated waste streams. At neutral or high pH, the silica filter could lower mercury concentrations by as much as four orders of magnitude in ppm concentration solutions but its efficiency is decreased at lower pH due to the protonation of the thiol (Nooney, et al., 2001).

Waste gas is usually treated for mercury by passing the gas or condensate via a bed of adsorbent. Among the adsorbent materials, inorganic materials such as alumina, molecular sieves (Shafawi, Ebdon, Foulkes, Stockwell, & Corns, 2000), zeolite, and bentonite (Jurng, et al., 2002) can be considered as the efficient mercury removal agents. Competent removal efficiency can be achieved with the use of activated carbon, especially if the carbon was impregnated with sulfur and treated with a little amount of potassium iodide (Henning, Keldenicht, Knoblauch, & Degel, 1988). Current studies suggest that wood char has almost similar removal efficiency as activated carbon and the sulfur impregnated wood char is found to have the same lifetime as the sulfur impregnated activated carbon (Jurng, et al., 2002). Since all the processes applying adsorbents as the mercury removal agent, the adsorbents will eventually become saturated after the mercury is adsorbed onto the adsorbent. Hence, the adsorbents are required to be replaced from time to time. It is also notable that the mercury removal efficiency, lifetime, as well as the long term stability

increases upon the impregnation of sulfur as the process is transformed from physisorption to chemisorptions (Hutchison & Atwood, 2003).

Meanwhile, another prospective mercury removal matrix is biopolymers as they are reasonably cheap. For example, cellulose can be brominated, and thiolated with NaSH and used as a mercury filter (Marchant, 1974). It is proved effective especially at high pH but it could not be regenerated. Thiolated corn stick powder also exhibited good mercury removal efficiency, giving greater than 97 % mercury removal (Bonnet, Choe, Lee, Masse, & Verdier, 1986). Anyhow, less work has been done on biopolymers compared to synthetic polymer supports.

Another idea to remediate the mercury-polluted site in water system is by precipitation so that it can be extracted from the waste stream. The essence of this method is to reduce the Hg^{II} to the far less soluble Hg^{0}. A simple compound applied with this principle is powdered zinc metal (Ku, Wu, & Shen, 2002). However, it is still necessary to recover the resulting metallic mercury after the redox reaction from divalent mercury in the solution and to further treat the waste stream which contains extremely high zinc levels. Another nearly similar idea is the photoreduction of mercury with a titanium oxide catalyst (Bussi, Ohanian, Vázquez, & Dalchiele, 2002). Under the sunlight, the metallic mercury and Hg_2Cl_2 are plating out onto the TiO_2 particles. The contaminated catalyst can be regenerated to TiO_2 after treatment with acid but unfortunately, it is inhibited by the presence of Ca^{II} and Mg^{II} ions. The same scenario occurs where the generated elemental mercury is still required to be removed. Furthermore, addition of a ligand to precipitate the mercury compounds is also one popular method of mercury extraction. The example for this application could be sodium or potassium dimethyldithiocarbamate (DMDTC) (Tassel, Rubio, Misra, & Jena, 1997). This compound will form insoluble complexes with mercury, precipitate, and the

complexes are removable from the water. The problem with this compound is the long-term stability of these precipitates as the studies shown that application of DMDTC to the contaminated site will result in a sudden drop of mercury level, but the mercury level begins to increase if the precipitates are not removed from the water. This indicates that the mercury is leaching out (Matlock, Henke, & Atwood, 2002). DMDTC is also known to decompose into by-products, such as thiram which are harmful to fish. Consequently, this is not a good choice for in-situ remediation. There are two other commercial precipitating agents, such as sodium thiocarbonate (TC) and 2, 4, 6-trimercaptotriazine (TMT) which also exhibit ability to precipitate mercury, but they are not as effective as DMDTC.

Another approach is to add complexing surfactants, which will combine with mercury and other toxic metals and change their solubility so that they can be extracted into an organic solvent (Schwuger, Subklew, & Woller, 2001). The surfactants tested were mostly nitrogen and oxygen based ligands, and the organic solvents used were kerosene, decane, and 1-decanol. Although this method is proven to be effective, it requires some significant infrastructure and it could only practically be conducted at a wastewater treatment site. On the other hand, this method is generating new metal contaminated organic layers which the author fails to see advantage of this method over simple precipitation method (Hutchison & Atwood, 2003).

A synthetic compound- MetX was created and patented at the University of Kentucky (David, Brock, & Matlock, 2002). MetX consists of various types of benzenediethanthiolates which can irreversibly bond with soft heavy metals and form insoluble, non-leaching precipitates. Most importantly, the precipitates are not viable to be attacked by methylating bacteria. Various studies showed that MetX is effective in binding Cd, Hg, and Pb. Its ability has been tested over aqueous field samples from battery recycling

plants (Matlock, Howerton, & Atwood, 2002b), gold-mining effluent (Matlock, Howerton, Robertson, & Atwood, 2002; Matlock, Howerton, Van Aelstyn, Nordstrom, & Atwood, 2002), dental waste solutions, soil-bound mercury (Matlock, Howerton, & Atwood, 2003), and acid mine drainage (Matlock, Howerton, & Atwood, 2002a). The levels of Cd, Ce, Fe, Pb, and Mn decreased within the six hours of treatment at near neutral pH, with some of them below the limit of ICP instrument. The leaching experiments of MetX over 30-day period at various pH from 0-10 and none of the Cd, Hg, or Pb precipitates leached. Only Fe-compound was found to leach (less than 10 %) at acidic pH.

In 2002, another promising sorbent, thiol-functionalized nanoporous silica material which is known as thiol functionalized Self Assembled Monolayers on Mesoporous Silica (thiol-SAMMS) has also demonstrated its effectiveness in removing mercury. Two waste streams which consisted of mercury concentrations that ranged from ~700 ppm to ~5 ppm respectively were tested. The results implied that thiol-SAMMS was effective in reducing mercury concentrations in the two waste streams to the limit of ≤ 0.2 ppm and can selectively scavenge strongly complexed mercury from dilute to relatively concentrated waste matrices (Fryxell & Cao, 2007).

Recently, porous zinc tin sulfide aerogel material (ZTS) which was synthesized through metathesis reaction was found to possess high affinities toward soft heavy metal which includes mercury. The heavy metal removal experiments indicate that this zinc chalcogel is able to remove soft heavy metal ions, such as Hg^{2+}, Cd^{2+}, and Pb^{2+} from aqueous media (Oh, Bag, Malliakas & Kanatzidis, 2011).

In a nutshell, mercury issue can be likened to a grenade which will explode one day if mercury emissions phenomenon persists without any appropriate effort or action being taken. Although more and more reports from the trusted organizations have revealed that

worldwide mercury concentrations have increased dramatically throughout the centuries, this life-threatening alarm does not seem to alert the entire global population in view of the fact that mercury pollution due to anthropogenic sources is still growing exponentially with time. Therefore, lenient environmental standards and weaker environmental regulations should be strongly enforced to shun the historical mercury catastrophe to be repeated.

1.5 Motivations

Hereby, two open questions have been addressed: What type of material is suitable to trap mercury in the water aqueous system and why it is being chosen? In this work, metal sulfide has been selected as the material to capture mercuric ion in the aqueous system. The key reason is that mercury and its compounds are very soft Lewis acid, and hence, both kinetically and thermodynamically "prefer" to undergo reaction with soft bases, e.g S^{2-} based on *Hard Soft Acid Base (HSAB)* theory. In this case, the soft acid (mercury species) reacts faster and forms stronger bonds with soft bases (sulfur species).

Besides that, metal sulfide is a naturally occurring compound which can be easily synthesized or obtained from natural sources. In addition, there were supporting facts from the literature that metal sulfides are good candidates towards heavy metal sorption. Among the metal sulfides systems, only Fe_xS: *Pyrite* (FeS_2), *Pyrrhotite* ($Fe_{1-x}S_x$), *Mackinawite* (FeS), and Mo_xS have established deep studies on the interaction between mercuric ion and the trapping systems. Thus, a complete coverage of studies should have been done on other metal sulfide system, for instance, Cu_xS.

It is expected that the formation of *cinnabar* (HgS) might be the end product after mercury trapping based on the HSAB theory coupled with the unique property of copper as the sulfide tuning agent. In general, *cinnabar* (HgS) is the most stable form of mercury in

the environment with $K_{sp} = 2 \times 10^{-53}$. It is the most ideal compound for storing mercury compounds because it is relatively insoluble and less volatile than other forms of mercury.

Moreover, another open question regarding the structural, physical and chemical properties of the potential candidate (CuS) which has the ability to remove Hg(II) in aqueous system is still unknown. This has indirectly broadened the research opportunity in this discipline.

1.6 Objectives of Research

The aims in this research include:

- To design Cu_xS adsorbent as a mercury trapping media in aqueous system.
- To control and optimize synthesis parameters for the formation of CuS system by hydrothermal process.
- To study the stability of copper sulfide as a function of oxidative condition.

1.7 Outline of Research Work

Overall, there are three main sections in this mercury management research project which involve the method development of mercuric ion determination by complexation using UV-Vis spectrophotometry, synthesis and characterization of unsupported copper sulfide, as well as performance testing on the application of phase pure unsupported copper sulfide in trapping Hg(II) in aqueous system. The method development and performance testing of the materials synthesized have been primarily covered by *John Au Yoong Yow Loo*. Whilst, the main focus in this research work is on the synthesis and characterization of unsupported copper sulfides. In order to achieve the aims mentioned in **Section 1.6**, there are four well-organized

work scopes which need to be investigated carefully, namely, synthesis of copper sulfides at different synthesis parameters, materials characterization, further studies on phase pure copper sulfides, and phase stability studies of CuS. The overview of the work scope is illustrated in **Figure 1.4**.

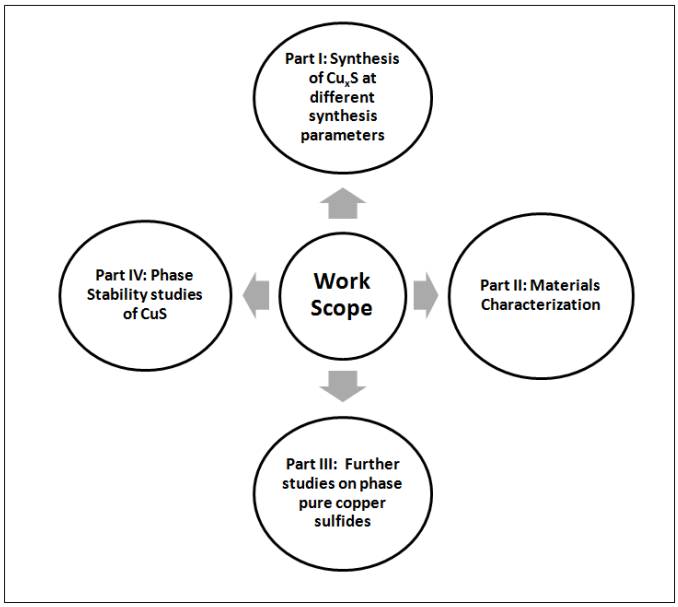

Figure 1.4: Overview of work scope.

Part I: Synthesis of Cu_xS at Different Synthesis Parameters

In this part, the synthesis of the material has been done via hydrothermal route by employing the rotating furnace. The copper source used in the preparation of copper sulfide was copper (II) nitrate, while the sulfur source applied was sodium thiosulfate. Three approaches of synthesis parameters were systematically studied in order to accomplish the aim of designing a phase pure CuS which will be an effective phase to trap mercury in aqueous system. The synthesis parameters are list:

a) Synthesis Temperature - [25, 35, 65, 95, 155] °C

b) Mole ratio of Cu: S - [1:1, 1:1.5, 1:2, 1:2.5, 1:3, 1:3.5, 1:5]

c) Synthesis Time - [1, 3, 6, 8, 12] hours

The detailed procedures used to prepare the products are discussed in **Chapter 3- Research Methodology**.

Part II: Materials Characterization

The products synthesized were subjected to series of characterizations after hydrothermal treatment. With the goal of understanding the structural, chemical, and thermal properties of the materials synthesized, three primary analyses were carried out: structural analysis, chemical analysis, and thermal analysis. The structural analyses discussed in this dissertation are powder X-ray Diffraction (PXRD), Field Emission Scanning Electron Microscopy (FESEM), High Resolution Transmission Electron Microscopy (HRTEM) and Brunauer-Emmett-Teller (BET) gas adsorption methods. Meanwhile, the chemical analyses include X-Ray Fluorescence (XRF), and Energy Dispersive X-Ray Spectroscopy (EDX) techniques. The thermal analyses applied in this work are Thermogravimetric-Mass Spectrometry Analysis (TGA-MS) and Differential Scanning Calorimetry (DSC). Typically, all the materials synthesized from the three synthesis parameters are subjected for powder XRD, FESEM-EDX, and XRF measurements in order to identify the crystal phase, morphology, and elemental composition of the as formed products. For phase pure products, additional analyses (BET, HRTEM, TG-MS and DSC) are carried out to provide a better understanding on the structural and thermal properties of the sample. The principle and the measuring conditions of each measurement are discussed in **Chapter 3- Research Methodology**.

Part III: Further Studies on Phase Pure Copper Sulfide (Cu_xS)

After a series of systematic studies, two phase pure copper sulfides (Cu_xS), i.e. Cu_9S_5-*digenite* and CuS-*covellite* were successfully prepared. The phase pure copper sulfide (*covellite*) has been tested for its performance towards mercury trapping. At the same time, the phase pure copper sulfides which have been synthesized were further characterized in additional two approaches to further identify the properties of the phase pure products:

a) Structural analyses: microstructural, surface area, total pore volume, average pore size determination
b) Thermal analyses: thermal stability

Part IV: Phase Stability Studies on *covellite* (CuS)

The prepared single phase *covellite* was found to transform to a mixed phase of copper sulfide (CuS) and copper sulfate ($CuSO_4$) after a certain period. Various characterization techniques such as powder XRD, EDX, and TGA-MS have proven that *covellite* was transformed into a mixed phase compound. Therefore, a systematic study was carried out to investigate the stability of this material with time in ambient condition.

CHAPTER 2

LITERATURE REVIEW

In the preceding chapter, several sections about mercury which comprise the sources of mercury emissions, applications of mercury, impacts of mercury exposures, and mercury remediation have been discussed in detail. Moreover, the motivations, objectives, as well as the outline of the research work have been unveiled in the first chapter. Meanwhile, the deliberations on the overview of copper sulfides family, applications, and methodologies of its preparations will be discussed in this Chapter.

2.1 Types of Copper Sulfides (Cu_xS)

Copper sulfides describe a family of chemical compounds and minerals with the formula Cu_xS_y. However, copper sulfide is used to describe as the compound which consists of mixed copper-iron sulfide ores, i.e. *chalcopyrite*- $CuFeS_2$ (Palache, Berman, & Frondel, 1944), *bornite*- Cu_5FeS_4 (Palache, et al., 1944), and *cubanite*- $CuFe_2S_3$ in the mining industry. In chemistry, copper sulfide or binary copper sulfide means that any binary chemical compound of the elements copper and sulfur. Most of the copper sulfides such as *chalcopyrite*- $CuFeS_2$, *bornite*- Cu_5FeS_4, *covellite*- CuS (Wells, 1984), and *chalcocite*- Cu_2S (Wells, 1984) are economically important feedstock for copper ores.

Copper sulfides can be classified into three different categories based on the Cu_zS nomenclature and **Table 2.1** summarizes the classifications of copper sulfides. The first category is copper disulfide where its z value is 0.5. Copper disulfide compounds consist of S which is present as S-S units (S_2^-) and its crystal structure is analogous to *pyrite* (FeS_2). Copper disulfide has incomplete occupancy of sulfur p band and it is a metallic conductor.

The second category is mixed copper mono-disulfide where the z value lies between $1.5 \leq z < 1.5$. The examples include CuS, Cu_9S_8 or $Cu_{1.12}S$, and $Cu_{39}S_{28}$ or $Cu_{1.39}S$. In this category, the compounds contain (S^{2-}), (S_2^{-}), and (S_2^{2-}) anions. They usually consist of alternating sulfide anions with copper ions coordinated in trigonal and tetrahedral interstices. They can be either metallic conductor or semiconductor. The last category is copper monosulfides with z value lies between $1.5 \leq z \leq 2.0$ and it includes Cu_7S_4or $Cu_{1.75}S$, Cu_8S_5 or $Cu_{1.6}S$, Cu_9S_5 or $Cu_{1.8}S$, $Cu_{31}S_{16}$ or $Cu_{1.96}S$, and Cu_2S. In the crystal structures of these compounds, S-S units are absent and sulfide anions (S^{2-}) are arranged either in hcp or fcc lattices. The copper ions are coordinated with both trigonal and distorted tetrahedral manner. These compounds are conductors at slightly elevated temperatures (semiconductor) (Greenwood & Earnshaw, 1984).

Table 2.1: Classifications of copper sulfides.

Category	*z* value	Cu_xS_y	Cu_zS
Copper disulfide	**0.5**	**CuS_2**	**$Cu_{0.5}S$**
Mixed copper mono-disulfide	**$1.0 \leq z < 1.5$**	**CuS** **Cu_9S_8** **$Cu_{39}S_{28}$**	**CuS** **$Cu_{1.12}S$** **$Cu_{1.39}S$**
Copper monosulfide	**$1.5 \leq z \leq 2.0$**	**Cu_8S_5** **Cu_7S_4** **Cu_9S_5** **$Cu_{31}S_{16}$** **Cu_2S**	**$Cu_{1.6}S$** **$Cu_{1.75}S$** **$Cu_{1.8}S$** **$Cu_{1.96}S$** **Cu_2S**

Copper sulfides with different stoichiometry can be obtained naturally as minerals or it can be prepared synthetically. Some of the copper sulfides occur as pure binary copper sulfide minerals (*villamaninite*- CuS_2 (Wells, 1984), *covellite*- CuS, *yarrowite*- Cu_9S_8 (R. J. Goble, 1980), *spionkopite*- $Cu_{39}S_{28}$ (R. J. Goble, 1980), *geerite*- Cu_8S_5 (R. J. Goble & Robinson, 1980), *anilite*- Cu_7S_4 (Wells, 1984), *roxbyite*- $Cu_{89}S_{50}$ (Ralph & Chau), *digenite*-

Cu_9S_5 (Wells, 1984), *djurleite*- $Cu_{31}S_{16}$ (Wells, 1984), *chalcocite*- Cu_2S (Wells, 1984), and etc which are yet to be discovered); while there are some naturally occurring mixed metal binary copper sulfide ores, such as *chalcopyrite*- $CuFeS_2$ (Palache, et al., 1944), *bornite*- Cu_5FeS_4 (Palache, et al., 1944), *villamaninite*- $Cu_{0.47}Ni_{0.25}Fe_{0.12}Co_{0.08}S_{2.08}$ (Schoeller & Powell, 1920). **Table 2.2** gives a summary on the pure and mixed binary copper sulfides respectively. The stoichiometries of pure binary copper sulfides (Cu_xS_y) are ranging from copper- rich *chalcocite* (Cu_2S) to copper- deficient *villamaninite* (CuS_2), of which, there are five intermediates which are stable at room temperature, *i.e*. *covellite*- CuS, *anilite*- $Cu_{1.75}S$, *digenite*- $Cu_{2-x}S$, x ranges from 0.18 to 0.25, *djurleite*- $Cu_{1.95}S$, and *chalcocite*- Cu_2S (Kashida & Yamamoto, 1991).

Table 2.2: Types of copper sulfides.

Types	Cu_xS_y/ $Cu_xM1_bM2_cM3_dS_y$	Cu_zS	Common name
Pure binary copper sulfides	**CuS_2**	**$Cu_{0.5}S$**	***villamaninite***
	CuS	**CuS**	***covellite***
	Cu_9S_8	**$Cu_{1.12}S$**	***yarrowite***
	$Cu_{39}S_{28}$	**$Cu_{1.39}S$**	***spionkopite***
	Cu_8S_5	**$Cu_{1.6}S$**	***geerite***
	Cu_7S_4	**$Cu_{1.75}S$**	***anilite***
	$Cu_{89}S_{50}$	**$Cu_{1.78}S$**	***roxbyite***
	Cu_9S_5	**$Cu_{1.8}S$**	***digenite***
	$Cu_{31}S_{16}$	**$Cu_{1.96}S$**	***djurleite***
	Cu_2S	**Cu_2S**	***chalcocite***
Mixed metal binary copper sulfides	**$CuFeS_2$**	-	***chalcopyrite***
	Cu_5FeS_4	-	***bornite***
	$Cu_{0.47}Ni_{0.25}Fe_{0.12}Co_{0.08}S_{2.08}$	-	***villamaninite***

2.2 Applications of Copper Sulfides

Copper sulfides have been of intense attention due to its unique and excellent physical and chemical properties. Owing to the characteristics of showing metallic conductivity and to transform into a superconductor at 1.6K (Zhang, Wen, & Yang, 2003), copper sulfides show a promising and prospective economical value especially for their applications as p-type semiconductors in solar cell (Johansson, Kostamo, Karppinen, & Niinistö, 2002; Reijnen, Meester, Goossens, & Schoonman, 2003), photovoltaic and photodetector (Sartale & Lokhande, 2000), nonlinear optical material (Malyarevich, et al., 2000), optical filter (Li, et al., 2002; Nair & Nair, 1989) superionic material (Li, et al., 2002; Nair & Nair, 1989; Wakamura, 1997, 2002), nanometer scale switches (Sakamoto, Sunamura, & Kawaura, 2003) for programmable IC and logic circuits. In addition, copper sulfides are potential cathode material in lithium rechargeable batteries (Chung & Sohn, 2002), thermoelectric cooling material (Chivers, 1996), conductivity increasing coatings for polymer surfaces, and coatings for microwave shields in the forms of thin films (Cardoso & et al., 2001). Besides that, copper sulfides are also commonly applied as catalyst (Kuchmii & Korzhak, 2001; Raevskaya, Stroyuk, Kuchmii, & Kryukov, 2004), chemical sensor (room temperature ammonia sensor) (Sagade & Sharma, 2008), pigment or coloured indicator of nigrosine, biological labeling and so forth.

In line with the specific application of copper sulfides in this project, reviews of copper sulfides on the adsorption of mercury in water aqueous system have been done. According to Martellaro et al., Cu_2S has been used in removing Hg(II) in water aqueous system. The studies showed that the quantity of Hg^{2+} removed from solution corresponds directly with the quantity of Cu_2S dissolved. This suggests that the Hg(II) are removed

through precipitation with dissolved sulfide ion from metal sulfide. This also indicates that in acidic solutions there is no physical or chemical adsorption of Hg^{2+} onto Cu_2S (Moore, Martellaro, Peterson, Abbott, & Gorenbain, 2001). Another study which was conducted by Martellaro et al., CuS was also used to remove Hg(II) in aqueous water system under batch equilibration studies. The results showed that cinnabar, HgS does not form as end product and mercuric ion is not removed by precipitation. No reaction mechanism is deduced for CuS to remove Hg(II) from aqueous water solution (Moore, Martellaro, & Peterson, 2000).

Hg(II) adsorption onto CuS has been deeply described in Phillips, H. O. et al., 1965 (Phillips & Kraus, 1965). Continuous column chromatographic technique has been applied to investigate the sorption of Hg^{2+} and Ag^{+} onto CuS. Their studies showed that both Hg(II) and Ag(I) adsorb onto CuS via ion-exchange displace reaction and their selectivity is related primarily to the solubility of sulfides formed and being displaced (K_{sp}). In adsorption of Hg(II) onto CuS, formation of white colored double salt, $2Hg_2S{\cdot}Hg(NO_3)_2$ is observed in addition to the mercury sulfide formed. The formation of the double salt is mainly due to the adsorption of $Hg(NO_3)_2$ onto the HgS or Hg_2S formed during the reactions.

Competitive adsorption of Hg(II) and other radioactive tracer metal ions onto CuS have been studied under both batch and continuous column chromatography technique (Wu & Yang, 1976). Results shows that 100 % removal efficiency of Cu(II) onto CuS can be achieved in column chromatography while it decreases in batch experiments. For Hg(II), the adsorption capability decreases in both batch and column chromatography experiments.

Industrial applications of CuS/C and CuS/Al_2O_3 to remove Hg(II) in wastewater has been found in US patent: 5080799 (Yan, 1992). Dynamic flow system has been employed in the process and HgS is claimed to be formed during the reaction. An interesting finding

is that the reacted adsorbent was successfully regenerated by heating the reacted powder in a stream of hot gases (flue gas, steam, and etc) preferably at 149 $^{\circ}$C or higher or by oxidative regeneration.

In short, adsorption of Hg(II) onto CuS has been investigated by researchers in the past three decades. However, there are still many open questions regarding the structural, physical and chemical properties of this potential candidate (CuS) which has the ability to adsorb Hg(II) in water aqueous system. This has indirectly broadened the research opportunity in this discipline.

2.3 Historical Development of Hydrothermal Synthesis

The term hydrothermal is purely of geological origin which was first used by the British Geologist, Sir Roderick Murchison (1792-1871), to describe the action of water at elevated temperature and pressure in bringing about changes in the earth's crust leading to the formation of various rocks and minerals (Murchison, 1840s). A majority of the minerals formed in the postmagnetic and metasomatic stages in the presence of water at elevated pressure and temperature conditions are said to be "of hydrothermal origin". This covers a vast number of mineral species including ore deposits. It is well known that the largest single crystal formed in nature (beryl crystal of > 1000 gm) and some of the largest quantities of single crystals created by man in one experimental run (quartz crystals) are both of hydrothermal origin. An understanding of the mineral formation in nature under elevated pressure and temperature conditions in the presence of water led to the development of the hydrothermal technique. Geologists carried out the earliest work on the hydrothermal techniques in the 19th century in order to understand the genesis of rocks and minerals by simulating the natural conditions existing under the earth crust. However,

materials scientists popularized the technique, particularly during 1940's. It was successfully adopted by Schafthaul (1845) to obtain quartz crystals upon transformation of freshly precipitated silicic acid in Papin's digestor (Schafthaul, 1845). Thus, the hydrothermal technique became a very popular means to simulate the natural conditions existing under the earth's crust and synthesizing them in the laboratory.

The first successful commercial application of hydrothermal technology began with mineral extraction or ore beneficiation in the previous century. The use of sodium hydroxide to leach bauxite was invented by *Karl Josepf Bayer* (1871-1908) as a process for obtaining pure aluminium hydroxide which can be converted to pure Al_2O_3 suitable for processing to metal (Goranson, 1931). Even today, over 90 million tons of bauxite ore is treated annually by this process (Habashi, Dec. 5-7, 1994). Similarly, *ilmenite*, *wolframite*, *casiterite*, *laterites*, a host of uranium ores, sulfides of gold, copper, nickel, zinc, arsenic, antimony and so on, are treated by this process to extract the metal. Further importance of the hydrothermal technique for the synthesis of inorganic compounds in a commercial way was realized soon after the synthesis of large single crystals of quartz by *Nacken* (1946) and zeolites by *Barrer* (1948) during the 1930's and 1940's, respectively (Barrer, 1948; Nacken, 1946). The sudden demand for the large size quartz crystals during World War II forced many laboratories in Europe and North America to grow large size crystals. Subsequently, the first synthesis of zeolite that did not have a natural counterpart was carried out by *Barrer* in 1948 and this opened altogether a new field of science, molecular sieve technology (Barrer, 1962). The success in the growth of quartz crystals has provided further stimuli for hydrothermal crystal growth (Nacken, 1950).

In the last decade, the hydrothermal technique has offered several new advantages like homogeneous precipitation using metal chelates under hydrothermal conditions,

decomposition of hazardous and/ or refractory chemical substances, monomerization of high polymers like polyethylene terephthalate, and a host of other environmental and chemical engineering issues dealing with recycling of rubbers and plastics (instead of burning), and so forth. However, the main disadvantage of the hydrothermal system is the black box nature of the apparatus, as one cannot observe directly the crystallization processes. Nevertheless, in the recent years, remarkable progress has been made in this area through the modeling of the hydrothermal reactions, and the study of kinetics of the hydrothermal processes, which have greatly contributed to the understanding of the hydrothermal technique.

Today, the hydrothermal technique has found its place in several branches of science and technology, and this has led to the existence of several related techniques such as, hydrothermal synthesis, hydrothermal growth, hydrothermal alteration, hydrothermal treatment, hydrothermal metamorphism, hydrothermal dehydration, hydrothermal decomposition, hydrothermal extraction, hydrothermal sintering, hydrothermal reaction sintering, hydrothermal phase equilibria, hydrothermal electrochemical reaction and so forth. All these hydrothermal related techniques have involved materials scientists, earth scientists, materials engineers, metallurgists, physicists, chemists, biologists. The success of the hydrothermal technique after passing through several ups and downs can be largely attributed to the rapid advances in the apparatus involved in hydrothermal research and also the entry of a large number of physical chemists, who have contributed greatly to the understanding of hydrothermal chemistry (Byrappa, 1994). Further, the modeling and intelligent engineering of the hydrothermal process have also greatly enhanced our knowledge in the field of hydrothermal research (Byrappa & Yoshimura, 2001; Eckert, Hung-Houston, Gersten, Lencka, & Riman, 1996; Lencka, Anderko, & Riman, 1995).

In this work, batch hydrothermal method is selected to synthesize copper sulfides for several reasons. This approach is of favored advantage because only mild reactants like water soluble salts such as copper (II) nitrate and sodium thiosulfate are involved; unlike in other methods where the need of employing strong reactants like hydrogen sulfide (Brelle, Torres-Matinez, McNulty, Mehra, & Zhang, 2000; Chen, et al., 2003), ammonium sulfide (Tsamouras, Dalas, Sakkopoulos, & Koutsoukos, 1998), and sodium sulfide (Gao, et al., 2008; Kore, Kulkarni, & Haram, 2001; Wang, et al., 2007) are necessary. These strong reactants are tedious in handling which might lead to safety issue as well as posing environmental issues due to the liberation of toxic gasses. In addition, the hydrothermal batch route does not involve additional procedure like the purging of argon gas (Brelle, et al., 2000; Tezuka, et al., 2007), nitrogen gas (Wang, et al., 2007; Zhang, Wu, & Chen, 2006), or additional of hydrazine sulfate (Tsamouras, et al., 1998) as required in most of the precipitation synthesis to avoid sulfide oxidation. In comparison with other synthesis methods used to synthesize copper sulfides, hydrothermal batch route is a simpler, more economical, hassle-free, and eco-friendly method.

2.4 Reviews on Copper Sulfide Synthesis Methods

In nature, sulfides are one of the most abundant minerals whose origin is closely related to hydrothermal-high pressure and temperature. The experimental studies on the growth of sulfides began in the 19^{th} century; however a systematic study began after the discovery of their technological potential, especially as photo semiconductors and piezoelectric properties (Byrappa & Yoshimura, 2001).

In general, copper sulfide can be prepared through three different reactions, namely solid state, liquid phase, and gaseous phase reactions. These reactions cover up numerous

synthetic methods which include hydrothermal (Chen, Yu, & Li, 2009; Cheng, Wang, Si, & Geng, 2010; Li, Wu, & Shi, 2010), solvothermal (Du, et al., 2007; Li, Bi, Kong, & Qin, 2009; Liu & Xue, 2009), microemulsion (Gao, et al., 2004; P. Zhang & Gao, 2003), sol-gel/ precipitation (Kalyanikutty, Nikhila, Maitra, & Rao, 2006; Simonescu, Patron, Teodorescu, Brezeanu, & Capatina, 2006; Xu, Wang, Zhu, & Zhou, 2006), photochemical (Mathew, Rajesh, Ichimura, & Udayalakshmi, 2008), microwave irradiation (Liao, Zhu, & Chen, 2001; Ni, et al., 2004; Thongtem, Phuruangrat, & Thongtem, 2007), sonication (Singh, Martinez-Morales, Bozhilov, & Ozkan, 2007; Xu, Xu, Geng, Li, & Zhu, 2006), chemical vapor deposition (Kunita, et al., 2002), spray pyrolysis (Krunks, Mellikov, & Bijakina, 1997) and so forth. On top of that, preparation of copper sulfide by using additives such as surfactants/ templates (An, Wang, He, & Wang, 2008; Chen, et al., 2009; Zou, Zhang, Zhang, Zhao, & Huang, 2007), capping agents (Brelle, et al., 2000; Gautam & Mukherjee, 2006; Lim, Wong, Ang, Low, & Chin, 2006), and composite (An, et al., 2008; Huang, Xiao, Chen, & Wang, 2009) have been reported.

To date, the types of copper and sulfur sources used in synthesizing copper sulfide have been reviewed. The copper sources are divided into three main categories, *i.e*, elemental copper (Feng, et al., 2007; Tezuka, et al., 2007; Wang, Li, Li, Wang, & Chen, 2007), inorganic copper salts which comprise of copper (II) nitrate (Liu & Xue, 2009; Wang, et al., 2009), copper (II) sulfate (Cheng, et al., 2010; Li, et al., 2010), copper (II) chloride (L. Chen, et al., 2009; Roy, Mondal, & Srivastava, 2008), copper (II) bromide (Gao, et al., 2008; Xu, Chen, Ma, & Gao, 2009), copper (II) oxide (Tang, et al., 2004; Zhang, Qiao, & Hu, 2004), copper (I) chloride (Wang, et al., 2007), copper (I) bromide (Thongtem, et al., 2007), as well as organic copper salts like copper acetate (An, et al., 2008; Li, et al., 2010), copper acetylacetonate (Ghezelbash & Korgel, 2005; Zhang, et al.,

2006)). For sulfur sources, the sulfur sources which have been studied previously included elemental sulfur (Feng, et al., 2007; Kuzuya, et al., 2007), sodium sulfide (Kalyanikutty, et al., 2006; Xu, et al., 2009), hydrogen sulfide (Brelle, et al., 2000), ammonium sulfide (Tsamouras, et al., 1998), carbon bisulfide (Cheng, et al., 2010; Roy, et al., 2008), sodium thiosulfate (An, et al., 2008; Mathew, et al., 2008), thiourea (Huang, et al., 2009; M. Li, et al., 2010), thioacetamide (Chen, et al., 2009; Wang, et al., 2009), as well as polysulfide species (sodium tetrasulfide, potassium tetrasulfide and etc).

Overall, the development of the hydrothermal synthesis of copper sulfide can be divided into two categories, namely hydrothermal treatment with assisting agent and hydrothermal treatment without using assisting agent. **Table 2.3** summarizes the literature reviews done on the synthesis of copper sulfides by employing different copper, and sulfur sources, as well as the assisting agent via hydrothermal route. For hydrothermal synthesis which involves the use of assisting agents, *Z. Cheng et al* .have successfully prepared CuS 3D flower-like nanoarchitecture where these CuS nanoarchitectures can be described as the combination of several similar hexagonal nanoplates by using copper (II) sulfate ($CuSO_4$), carbon bisulfide (CS_2) as well as polyvinylpyrrolidone (PVP), sodium hydroxide (NaOH), and ethanol (C_2H_5OH) as assisting agent (Cheng, et al., 2010). Besides that, *L. Chen et al.* have reported that tubular and flower-like CuS microcrystals can be synthesized by using copper (II) chloride, thioacetamide and CTAB (Chen, et al., 2009). In addition, *Qin et al.* have revealed that CuS submicroncrystals can be prepared with ball-, rod-, chrysanthemum-like shape by using copper nitrate, thiourea, and ethanol (Qin, Fang, Ou, Liu, & Su, 2005).

On the other hand, the hydrothermal synthesis without involves the use of assisting agents was carried out by *K. Tezuka et al.* with the preparation of polycrystalline CuS from

elemental copper and sulfur in water (Tezuka, et al., 2007). Similar approach was reported by *Y. Ni et al* for the synthesis of CuS nanowires by employing copper (II) sulfate and thiourea as reactants in the absence of any assisting agent (Ni, Liu, Cao, Wei, & Hong, 2007). Meanwhile, the synthesis of sphere-, urchin-, and tube-like CuS nanocrystallites applying copper (II) sulfate and sodium thiosulfate without any further addition of assisting agent was discussed by *Y.C. Zhang et al* (Zhang, Hu, & Qiao, 2004).

Table 2.3: Summary on the synthesis of copper sulfides by using different copper source, sulfur source and assisting agent.

Reference	Cu source	S source	Assisting agent	CuS (PDF no.)
(Cheng, et al., 2010)	$CuSO_4$	CS_2	PVP, NaOH, C_2H_5OH.	Hexagonal *covellite* (06-0464)
(Li, et al., 2010)	$Cu(ac)_2$, $CuSO_4$	$(NH_2)_2CS$	chitosan, acetic acid	Hexagonal covellite (06-0464)
(Chen, et al., 2009)	$CuCl_2$	C_2H_5NS	CTAB	Hexagonal *covellite* (06-0464)
(Huang, et al., 2009)	$CuSO_4$	$(NH_2)_2CS$, urea	PSA, PVP	Hexagonal *covellite* (06-0464)
(Ding, et al., 2009)	$CuCl_2$	$(NH_2)_2CS$	SDBS	Hexagonal *covellite* (78-0876)
(Wang, Fang, & Lin, 2009)	$CuCl_2$	C_2H_5NS	NaOH	Hexagonal *covellite* (78-0876)
(Zou, Zhang, Zhang, Zhao, & Huang, 2007)	$Cu(ac)_2$	$(NH_2)_2CS$	citric acid, C_2H_5OH	Hexagonal *covellite* (06-0464)
(Roy & Srivastava, 2006)	$CuCl_2$	DTO	C_2H_5OH, NH_4OH	Hexagonal *covellite* (78-0876)
(Gong, Yu, Qian, Luo, & Liu, 2006)	$CuCl_2$	C_2H_5NS	acetic acid	Hexagonal *covellite* (78-2121)
(Jiang, et al., 2005)	Copper powder	$Na_2S_2O_4$	acrylamide & SDBS	Hexagonal covellite (78-2121)

Table 2.3, continued.

(Qin, et al., 2005)	$Cu(NO_3)_2$	$(NH_2)_2CS$	C_2H_5OH	Hexagonal *covellite* (06-0464)
(Ji, et al., 2005)	$CuCl_2$	$(NH_2)_2CS$	PEG20000	Hexagonal *covellite* (06-0464)
(Tezuka, et al., 2007)	Cu powder	S powder	-	Hexagonal *covellite* (06-0464)
(Ni, et al., 2007)	$CuSO_4$	$(NH_2)_2CS$	-	Hexagonal *covellite* (78-0876)
(Li, Xie, & Xue, 2007)	$CuCl_2$	$C_3H_7NO_2S$	-	Hexagonal *covellite* (06-0464)
(Chen, Zhang, Wang, Wan, & Qian, 2006)	$CuSO_4$	$C_3H_7NO_2S$	-	Hexagonal *covellite* (06-0464)
(Chen, et al., 2004)	$CuSO_4$	$(NH_2)_2CS$	-	Hexagonal *covellite* (78-0876)
(Zhang, Hu, et al., 2004)	$CuSO_4$	$Na_2S_2O_3$	-	Hexagonal *covellite* (06-0464)
(Zhang, Qiao, et al., 2004)	CuO, $CuSO_4$, $CuCl_2$	$Na_2S_2O_3$	-	Hexagonal *covellite* (06-0464)
(Tang, et al., 2004)	CuO	$(NH_2)_2CS$	-	Hexagonal *covellite* (79-2321)

From the reviews, copper (II) sulfate, copper (II) chloride, and copper (II) acetate have been frequently used as copper source to produce *covellite*. Whilst, for sulfur source, the most popular salts used are thiourea, thioacetamide, and sodium thiosulfate. In our work, copper (II) nitrate and sodium thiosulfate have been selected as the main reactants in the synthesis. This is because they are relatively soluble in water and can be easily obtained from the market. Most importantly, the nitrate ion can be washed off easily during the washing or calcination procedure. Besides that, both of the salts are mild reactants which

impose no safety issues during the synthesis. These reasons made both of the salts the good candidates as raw materials in hydrothermal treatment.

On the other hand, it is clear that assisting agent plays an important role in directing the special features of copper sulfides produced. Various studies have demonstrated that copper sulfides with specific morphology and size can be produced by employing different copper and sulfur sources with the aid of assisting agent. However, without the use of assisting agent, the desired features of the copper sulfide can be still achieved with systematic studies on the optimization of synthesis parameters. Therefore, we have chosen a simpler approach which does not require the addition of assisting agent throughout the hydrothermal synthesis. This can be done by varying the synthesis parameters, thereby optimizing the properties of the materials synthesized. Throughout the studies, a profound understanding on the growth mechanism can be developed. The synthesis parameters which govern the structural and chemical properties of the final product formed can be identified as many basic questions in this field are still unanswered.

CHAPTER 3

RESEARCH METHODOLOGY

This chapter gives details on the materials and instruments used in this research. Besides that, the procedures used to synthesize the powder, the methods used to carry out the phase stability studies of CuS, coupled with the principle and the characterization techniques are also enclosed in this particular chapter.

3.1 Materials Synthesis

3.1.1 Raw Materials

In these experiments, copper nitrate heptasemihydrate and sodium thiosulfate pentahydrate were the key reactants used in the preparation of the Cu_xS powder. Silica gel was used as the drying agent to dry the precursor; while nitrogen gas was used as a blanket to keep the active component from reacting with the oxygen as well as the moisture in the air. The chemicals and gas used for the Cu_xS powder preparation are displayed in **Table 3.1**.

Table 3.1: List of chemicals and gas used in the experiments.

Chemical/ Gas	Brand	Molecular Formula	Molecular Weight (g/mol)	Purity (%)
Copper nitrate pentasemihydrate	*Riedel de Häen*	$Cu(NO_3)_2.2.5H_2O$	232.59	98.000
Sodium thiosulfate pentahydrate	*Merck*	$Na_2S_2O_3.5H_2O$	248.21	99.500
Silica gel	*Bendosen*	-	-	-
Mercury (II) chloride	*Merck*	$HgCl_2$	271.50	≥ 99.5
Sodium hydroxide	*Merck*	NaOH	40.00	≥ 99
Nitric acid	*Merck*	HNO_3	-	≥ 65
Purified nitrogen gas	*MOX*	N_2	-	99.999

3.1.2 Synthesis Equipments

There were several devices and instruments used in the Cu_xS preparation and performance testing which are summarized in **Table 3.2**.

Table 3.2: Instruments and devices involved during Cu_xS preparation and performance testing.

Instruments/ Devices	Purpose
Rotating furnace (custom-made by ITQ)	For hydrothermal reaction under high pressure and temperature
Vacuum pump (DOA-P504-BN, GAST)	For isolating the sample from filtrate in vacuum
Furnace	For sample drying
Vacuum desiccator	For sample drying without air at room temperature
Stainless steel Teflon-lined tubes	For hydrothermal reaction
Thermocouple	For measuring the synthesis temperature
pH electrode (DG-114, Mettler Toledo)	For pH measurement
Orbital shaker (OLS200, Grant)	For performance testing
Mercury Analyzer (MA-2000, NIC)	For measuring the concentration of Hg^{2+} after adsorption experiment

3.1.3 Sample Preparation

In this study, Cu_xS powder was prepared via hydrothermal route by using the rotating furnace. The overview of the research methodology is displayed in **Figure 3.1**. There are two important steps that need to be carried out before a sample is screened. The first step involves the preparation of the Cu_xS powder, and the second step is the characterization of the synthesized material. Both of these steps will be discussed in detail in **Sections 3.2.2 and 3.3** respectively. On the other hand, the screening of the materials in this study was

done by *John Au Yoong Yow Loo*. In order to further understand on the interaction between the synthesized powder and Hg(II) in water aqueous system, only a stable and phase pure material was subjected to the screening process. This screening was carried out to investigate the performance of the synthesized powder in treating Hg(II) in aqueous system.

The phase pure CuS synthesized previously was found to be not stable in the air in which it has been transformed to a phase mixture of pentahydrate copper sulfate and copper sulfide instead of a phase pure *covellite* initially. It is suspected that the as-formed material might contain traces of inner water which leads to recrystallographic changes or *covellite* itself is not persistent and stable enough to withstand the high humidity and oxidic condition in the atmosphere. Therefore, a systematic study which is described in **Section 3.2.3** has been carried out to study the deactivation of this material with time.

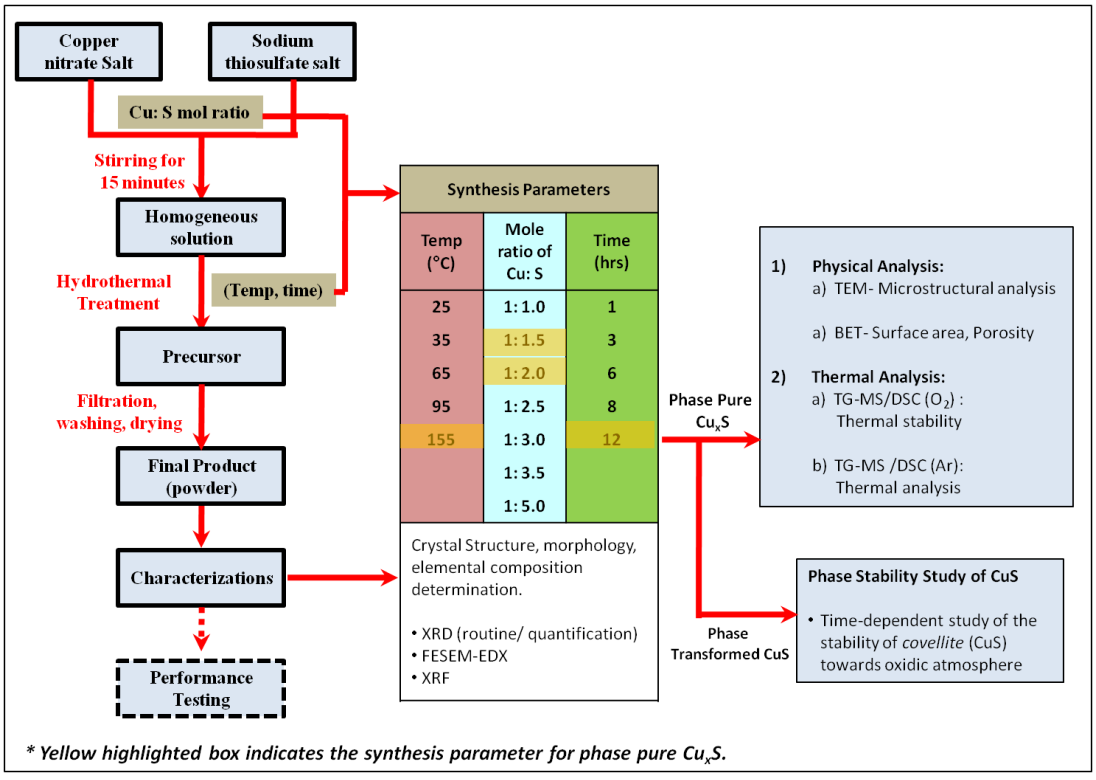

Figure 3.1: Schematic diagram of overview of research methodology.

(a) Synthesis of Copper Sulfides

All reagents used are of analytical grade from the commercial market and were used without further purification. Sodium thiosulfate ($Na_2S_2O_3.5H_2O$, *Merck*) was selected as the sulfur source while copper nitrate ($Cu(NO_3)_2.2½\ H_2O$, *Riedel de Häen*) was used as the copper source. In the typical procedure (as illustrated in **Figure 3.2**), copper sulfide was prepared by reacting copper nitrate with sodium thiosulfate in mol ratio of copper nitrate to sodium thiosulfate (abbreviated as Cu:S) of 1: 2 in 40.00 mL of deionized water. The solution was then mixed thoroughly under constant stirring for 15 minutes using magnetic stirrer; homogeneous yellow slurry was formed, which was then evenly transferred into two separate 50 mL Teflon-lined stainless steel tubes. The Teflon-lined stainless steel tubes were sealed and put into the rotating furnace. The rotating furnace was maintained at 155.0 °C for 12 hours. In order to measure the synthesis temperature during the reaction, a thermocouple was placed inside the furnace to measure the real reaction temperature for every one hour through an injection port without opening the furnace. After 12 hours, the Teflon-lined stainless steel tube was allowed to cool at ambient temperature. Then, the Teflon lined stainless steel tube was disassembled. The obtained yields which were black in colour (found in colourless filtrate) were filtered, washed with batches of deionized water until the final filtrate showed conductivity of less than 10 µS/cm. The collected product was dried overnight in a vacuum desiccator which consists of silica gel as a drying agent at ambient temperature. In this study, three synthesis parameters were varied to investigate the effects of each parameter towards the structural and chemical properties of the final crystal structure formed:

i. Different synthesis temperature

ii. Different Cu: S mol ratio

iii. Different synthesis time

The experiments were repeated by keeping the other two synthesis parameters at constant. The details of the modified synthesis parameters are outlined in **Tables 3.3, 3.4 and 3.5**. After the synthesis process, the products formed at different synthesis parameters were subjected for a series of characterizations which are discussed in **Section 3.3.1** in more details. All the samples synthesized from different synthesis parameters were characterized with four primary characterization tools, namely, powder XRD, FESEM, XRF, and EDX techniques. Meanwhile, additional analysis, i.e. BET, TGA-MS, DSC, and HRTEM were carried out for phase pure samples.

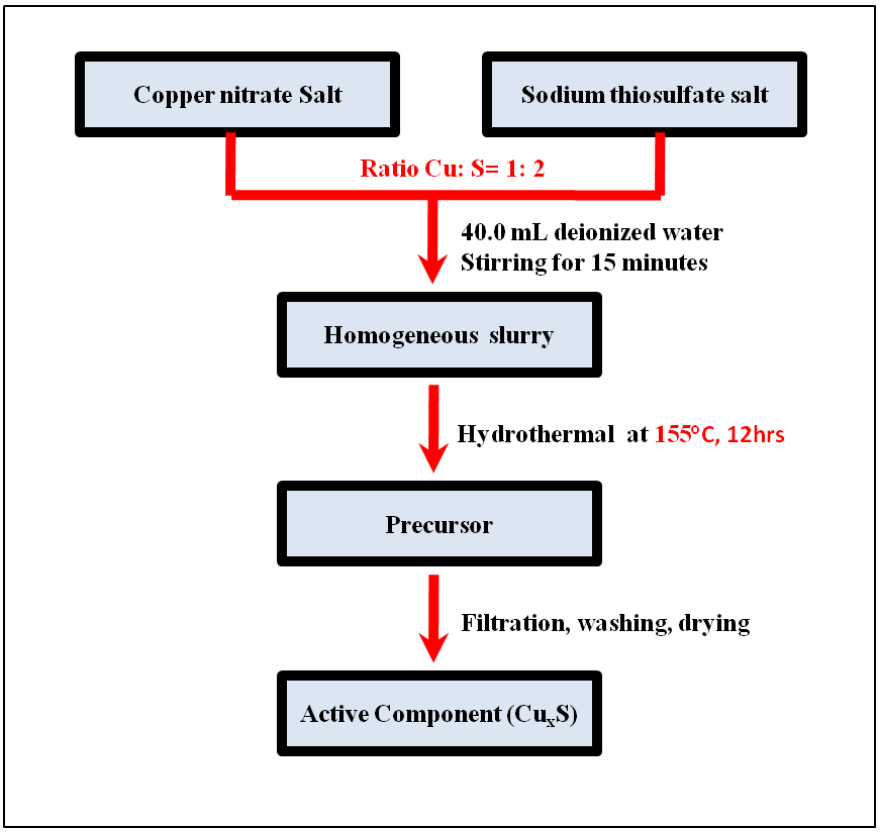

Figure 3.2: Diagram of the typical preparation procedure of Cu_xS powder.

Table 3.3: Details of the reactants prepared for synthesis temperature parameter.

Sample ID	No. of mol of $Cu(NO_3)_2$ (mol)	No. of mol of $Na_2S_2O_5$ (mol)	Mass of $Cu(NO_3)_2$ (g)	Mass of $Na_2S_2O_5$ (g)	Volume of H_2O (mL)	Synthesis Temperature (°C)
H01	0.0250	0.0500	5.8148	12.4105	40.00	**25.0**
H02	0.0250	0.0500	5.8148	12.4105	40.00	**35.0**
H03	0.0250	0.0500	5.8148	12.4105	40.00	**65.0**
H04	0.0250	0.0500	5.8148	12.4105	40.00	**95.0**
H05	0.0250	0.0500	5.8148	12.4105	40.00	**155.0**

Table 3.4: Details of the reactants prepared for Cu: S mol ratio parameter.

Sample ID	No. of mol of $Cu(NO_3)_2$ (mol)	No. of mol of $Na_2S_2O_5$ (mol)	Mass of $Cu(NO_3)_2$ (g)	Mass of $Na_2S_2O_5$ (g)	Volume of H_2O (mL)	Cu: S mol ratio
H06	0.0250	0.0250	5.8148	6.2053	40.00	**1: 1.0**
H07	0.0250	0.0375	5.8148	9.3079	40.00	**1: 1.5**
H05	0.0250	0.0500	5.8148	12.4105	40.00	**1: 2.0**
H08	0.0250	0.0625	5.8148	15.5131	40.00	**1: 2.5**
H09	0.0250	0.0750	5.8148	18.6158	40.00	**1: 3.0**
H10	0.0250	0.0875	5.8148	21.7184	40.00	**1: 3.5**
H11	0.0250	0.1250	5.8148	31.0263	40.00	**1: 5.0**

Table 3.5: Details of the reactants prepared for synthesis time parameter.

Sample ID	No. of mol of $Cu(NO_3)_2$ (mol)	No. of mol of $Na_2S_2O_5$ (mol)	Mass of $Cu(NO_3)_2$ (g)	Mass of $Na_2S_2O_5$ (g)	Volume of H_2O (mL)	Synthesis Time (hrs)
H12	0.0250	0.0500	5.8148	12.4105	40.00	**1**
H13	0.0250	0.0500	5.8148	12.4105	40.00	**3**
H14	0.0250	0.0500	5.8148	12.4105	40.00	**6**
H15	0.0250	0.0500	5.8148	12.4105	40.00	**8**
H05	0.0250	0.0500	5.8148	12.4105	40.00	**12**

(b) Phase Stability Studies of *covellite* over Time

The overview of the phase stability studies of CuS over time is illustrated in **Figure 3.3**. The product synthesized from the working procedure described in **Section 3.1.3 (a)** was used as the control study. At the same time, another batch of the product prepared in the similar way was subjected for additional storage method (purging with nitrogen gas for 3 minutes) before drying in the vacuum desiccator. The additional storage method was done by allowing the flow of purified nitrogen gas for 3 minutes through a tube connecting into a sample holder which consisted of sample. Meanwhile, the same synthesis procedures as indicated in 3.1.3(a) were repeated twice up to the washing step where the freshly prepared materials were then washed with 2 different methods, deionized water and ethanol; deionized water for a few times until the final filtrate showed conductivity of less than 10μS/cm; the collected black precipitate was subjected to two different drying methods- ambient condition in vacuum desiccators; at 50 ℃ for 6 hours in furnace respectively. The as-formed products from the four working procedures were then capped in a separate sample bottle and stored in a cool and dark place for selected time intervals as stated below:

a) 1week
b) 4 weeks
c) 12 weeks

The resultant products from the procedures above were subjected for Powder X-Ray Diffraction (PXRD) analysis to determine the crystalline phase and its phase purity.

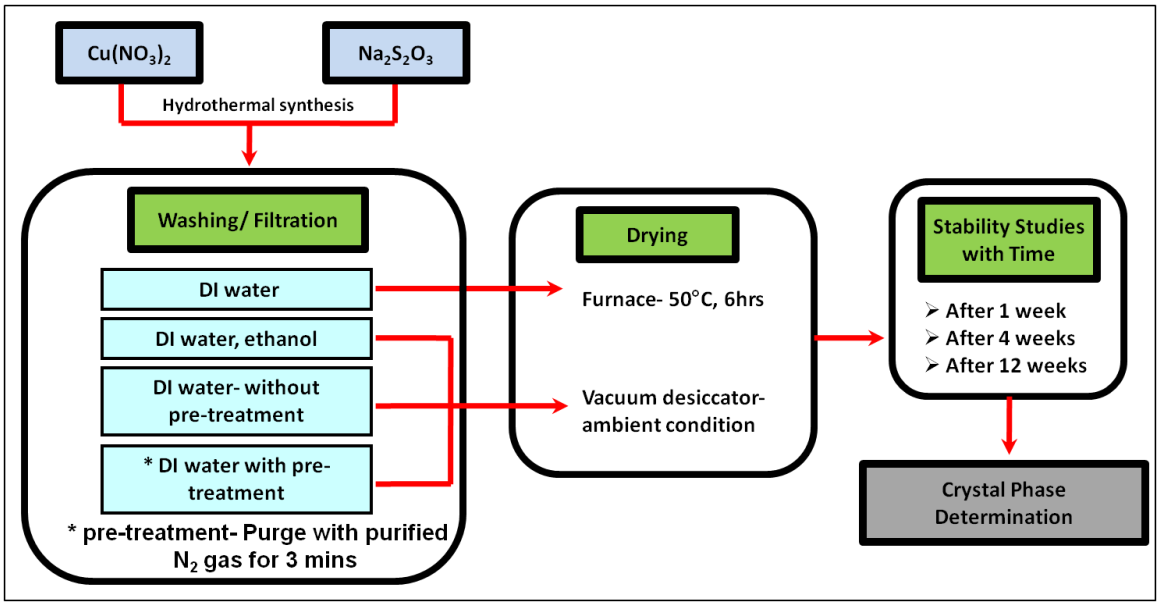

Figure 3.3: Overview of work procedure for phase stability study over time.

Table 3.6: Details of the samples prepared for phase stability study.

Sample ID	Washing medium	Drying medium	Duration (weeks)
H16	Deionized H_2O	Furnace	1
H17	Deionized H_2O	Furnace	4
H18	Deionized H_2O	Furnace	12
H19	Deionized H_2O, C_2H_5OH	Vacuum Desiccator	1
H20	Deionized H_2O, C_2H_5OH	Vacuum Desiccator	4
H21	Deionized H_2O, C_2H_5OH	Vacuum Desiccator	12
H22	Deionized H_2O	Vacuum Desiccator	1
H23	Deionized H_2O	Vacuum Desiccator	4
H24	Deionized H_2O	Vacuum Desiccator	12
H25	Deionized H_2O	N_2 gas purging + Vacuum Desiccator	1
H26	Deionized H_2O	N_2 gas purging + Vacuum Desiccator	12
H27	Deionized H_2O	N_2 gas purging + Vacuum Desiccator	24

(c) Application of *covellite* in Mercury Removal- Adsorption experiment

The method employed here is based on the methodology described elsewhere by *Au Yoong Yow Loo* (Au Yoong, et al., 2012). Phase pure *covellite* was used in the assessment for its application on trapping mercury in aqueous system. In this adsorption experiment, 1000 ppm of $HgCl_2$ stock solution was prepared with 1.000 g of $HgCl_2$ in 1.00 m^3 of deionized water using a 1.00 L volumetric flask. The working solution was prepared by diluting the stock solution with deionized water. After that, 100 mL of predetermined concentration of $HgCl_2$ was added into 4 different conical flasks using pipette. The pH of the solution was then adjusted with pH probe by employing HNO_3 and NaOH. Next, the 4 well-adjusted solutions were purged with purified nitrogen gas for 3 minutes. Meanwhile, 0.100 g of the synthesized phase pure CuS powder was weighted and added into the 4 different conical flasks. The 4 conical flasks were then sealed with parafilm and put into a controlled orbital shaker. The shaker was set at 25.0 °C and 155 rpm for 15 hours reaction. After 15 hours, the conical flasks were removed from the shaker and the solution in the conical flasks was filtered with filter paper. The filtrate was then collected and kept in a dark bottle for further concentration determination. The concentration of Hg^{2+} was measured with mercury analyzer. The procedures above were repeated twice to obtain a reproducible result. The amount of Hg(II) adsorbed (sorption capacity) at equilibrium, Q_e, was calculated from the mass balance equation:

$$Q_e = \frac{(C_0 - C_e)V}{m}$$

Where C_0 is the initial metal concentrations (mg/ L), V is the volume of solution used (L) and m is the mass of sorbent (g) used.

3.2 General Characterization Techniques

This section discusses the characterization techniques which were employed in this work in order to comprehend the properties of the powders prepared. Hence, the principles of the characterizations techniques and the parameters set to characterize the powders are described and recorded. In order to probe the information from a solid sample, three different approaches of the characterization techniques will be discussed here, namely, structural, chemical, and thermal analyses.

3.2.1 Structural Analysis

(a) Powder X-Ray Powder Diffraction (PXRD)

In Powder X-Ray Diffraction (PXRD), a collimated beam of X- rays, with wavelength λ = 0.5-2 Å, is incident on a specimen and is diffracted by the crystalline phases in the specimen according to Bragg's law ($\lambda = 2d \sin \theta$), where d is the spacing between atomic planes in the crystalline phase). The intensity of the diffracted X-rays is measured as a function of the diffraction angle 2θ and the specimen's orientation. This diffraction pattern is used to identify the specimen's crystalline phases and to measure its structural properties, including strain (which is measured with great accuracy), epitaxy, the size and orientation of crystallites (small crystalline regions). PXRD can also determine concentration profiles, film thickness, and atomic arrangements in amorphous materials and multilayers. It also can characterize defects. To obtain this structural and physical information from thin films, PXRD instruments and techniques are designed to maximize the diffracted X-ray intensities, since the diffracting power of thin films is small. A brief summary of this technique is described as below (Brundle, Evans, & Wilson, 1992):

Table 3.7: Brief summary of PXRD technique (Brundle, et al., 1992).

Information	Descriptions
Range of elements	All, but not element specific. Low Z elements maybe difficult to detect.
Probing depth	Typically a few µm but material dependent; monolayer sensitivity with synchrotron radiation.
Detection limits	Material dependent, but ~3 % in a two phase mixture; with synchrotron radiation can be ~0.1 %.
Destructive	No, for most materials.
Depth profiling	Normally no, but this can be achieved.
Sample requirements	Any material, greater than ~0.5 cm, although smaller with microfocus.
Lateral resolution	Normally none; although ~10 µm with microfocus.
Main use	Identification of crystalline phases; determination of strain, crystallite orientation and size; accurate determination of atomic arrangements.
Specialized use	Defect imaging and characterization; atomic arrangements in amorphous materials and multilayers; concentration profiles with depth; film thickness measurements.

Fundamentals and theoretical details

X-ray powder diffraction is nowadays used as the main characterization tool whenever solid materials are synthesized (Herein, 2008). When there is constructive interference from X rays scattered by the atomic planes in a crystal, a diffraction peak is observed. The condition for constructive interference from planes with spacing d_{hkl} is given by *Bragg's Law*:

$$\lambda = 2d_{hkl} \sin \theta_{hkl}$$

where θ_{hkl} is the angle between the atomic planes and the incident (and diffracted) X-ray beam, λ is the wavelength of the X-ray photons, d is the distance between lattice planes (hkl). For diffraction to be observed, the detector must be positioned so the diffraction

angle is $2\theta_{hkl}$ and the crystal must be oriented so that the normal to the diffracting plane is coplanar with the incident and diffracted X-rays and so that the angle between the diffracting plane and the incident X-rays is equal to the Bragg angle θ_{hkl} (Brundle, et al., 1992).

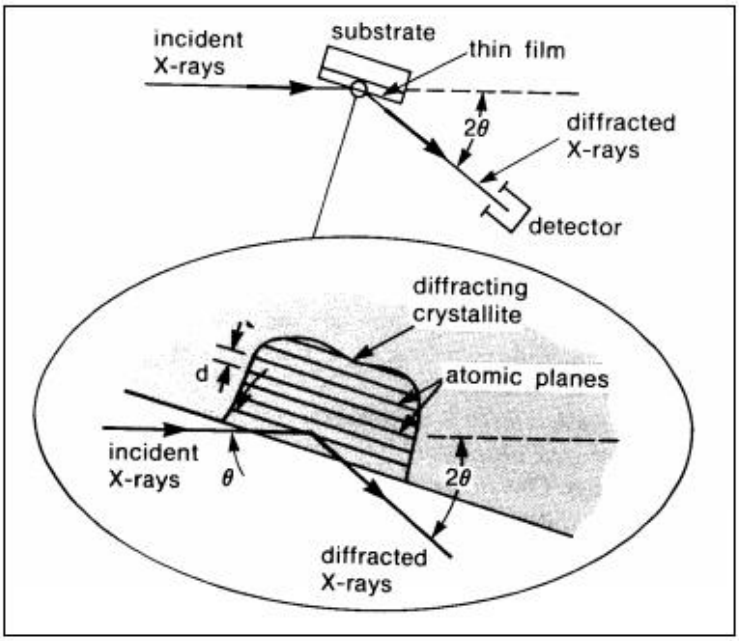

Figure 3.4: Basic features of a typical PXRD experiment (Brundle, et al., 1992).

Different features in an idealized PXRD pattern can provide important information to determine the structural properties of a solid material. **Table 3.8** summarizes the information contents of the feature which can be found on a PXRD pattern. PXRD analysis can provide qualitative, quantitative analysis in a crystalline mixture, as well as quantification of crystalline vs. amorphous material. Qualitative analysis is phase identification based on the comparison of line positions and intensity distributions of a set of reflections of the catalyst sample with a database. The *Powder Diffraction File* (PDF), distributed by the *International Centre for Diffraction Data* (ICDD) (formerly ASTM, then JCPDS), is the most commonly used and is often distributed together with or included in the most common X-ray powder diffraction software for data analysis.

Table 3.8: Information content of an idealized diffraction pattern (Girgsdies, 2009).

Features	Information
Peak position	d-spacing, lattice parameter (metrics of the unit cell)
Peak height (maximum intensity)	approximation for peak intensity
Peak area (integral intensity)	crystal structure (contents of the unit cell), phase amount (in a mixture)
Peak width	crystallite size, defects (strain, disorder)
Peak shape	crystallite size, defects (strain, disorder)

Peak profile analysis is also known as crystallite size and strain or micro-strain analysis (Young, 1993).Diffraction peak profile analysis is done by fitting one or more diffraction lines with a specific peak profile function, leading to information about the peak position, Full Width at Half Maximum (FWHM), the peak maximum intensity and the peak area. Calculations using the *Scherrer* equation always result primarily in crystallite sizes and not in particle sizes. The FWHM of a diffraction peak is a function of the coherent scattering domain size, which is equivalent to the grain size in a solid material. The FWHM is used to calculate the crystallite sizes using the *Scherrer* equation [Eq. (1)] and / or the micro-strain using the Wilson equation [Eq. (2)]:

$$FWHM = \frac{K\lambda \times 57.3}{D\cos\theta} \qquad (1)$$

$$FWHM = 4\varepsilon\tan\theta \qquad (2)$$

where *FWHM* is in °θ, *K* is the crystallite shape form factor (for spherical crystallites K = 0.94), λ is the X-ray wavelength, *D* is the crystallite size, θ is the *Bragg* angle corresponding to the maximum of the diffraction peak (in θ) and ε is the micro-strain.

Quantitative phase analysis is based on the determination and calculation of the absolute intensities of one or more phases identified in the catalyst sample. Quantitative

phase analysis requires the calculation of scattering power of one diffraction line or a set of diffraction lines of one phase. An internal standard phase has to be added to the sample and used for quantitative phase analysis. The absolute amount of the catalyst phase can then be calculated from the ratio of the peak areas of the internal standard phase and the sample catalyst phase considering their scattering power. The use of an internal standard for qualitative phase analysis allows one, in addition, to prove whether additional X-ray amorphous phases are present in the catalyst sample or not. Quantitative phase analysis can be done without an internal standard phase if at least two crystalline phases in the sample are identified. This method then results in relative weight amounts of each separate phase. However, no information about additional X-ray amorphous part of the sample is obtained if this method is used (Herein, 2008).

Full X-ray Powder Pattern Analysis, which is also known as the *Rietveld* method (Rietveld, 1967, 1969; Young, 1993) provides important improvements in the analysis of powder diffraction data. It allows the capture of a great deal of information from the study of the whole powder diffraction patterns and is mainly used for refining the structure of crystalline phases and for performing quantitative analysis of multiphase samples. The *Rietveld* method requires a starting model in the form of single crystal data which can be obtained from qualitative phase analysis (Herein, 2008). *Rietveld* fitting can be used to quantify crystalline compounds in a mixture. The accuracy of the fit will not only depend from the usual factors like data quality (signal/ noise ratio) and detection limits, but also from the appropriateness of the structure models used. The level of accuracy is usually unknown, unless the procedure can be checked with known mixtures. “100 %” corresponds to the total of all phases accounted for in the fit, which is not necessarily identical to 100 % of the sample (PXRD amorphous material, unknown phases, known phases without crystal

structure model are neglected). The results may be re-scaled using a known amount of an internal diffraction standard. Unlike in spectroscopy, the diffraction intensities of the components in a phase mixture are not strictly proportional to the concentration of the compounds (Girgsdies, 2009).

Measuring conditions: The PXRD analysis in this work has been performed using a Bruker X-ray Diffraction model D-8 equipped with *EVA Diffract* and *Topas* softwares for data acquisition. The PXRD measurements were done by using a CuK_{α} monochromatized radiation source (λ = 1.5406 Å) operated at 40 kV and 40 mA at ambient temperature. The measured samples were grinded into fine powder and placed in the sample holder. The surface of the sample was flattened and smoothened before putting it into the sample chamber of the diffractometer. A continuous 2θ scan mode from 4-80 °, with step time of 1 s and step size of 0.02 ° was set for the PXRD measurement. For peak profile analysis, step time was increased to 5 s in order to improve signal/ noise ratio. The diffraction patterns generated were matched with the database of *Powder Diffraction File* (PDF) and *Inorganic Crystal Structure Database* (ICSD).

(b) Scanning Electron Microscopy (SEM)

The Scanning Electron Microscope (SEM) is often the first analytical instrument used when a "quick look" at a material is required as the light microscope no longer provides adequate resolution. In the SEM, an electron beam is focused into a fine probe and subsequently raster scanned over a small rectangular area. As the beam interacts with the sample, it creates various signals (secondary electrons, internal currents, photon emission, etc.), all of which can be appropriately detected. These signals are highly localized to the area directly under the beam. By using these signals to modulate the brightness of a cathode

ray tube, which is raster scanned in synchronism with the electron beam, an image is formed on the screen. This image is highly magnified and usually has the "look" of a traditional microscopic image but with a much greater depth of field. With ancillary detectors, the instrument is capable of elemental analysis. The summary of SEM technique is described as the following (Brundle, et al., 1992):

Table 3.9: Brief summary of SEM technique (Brundle, et al., 1992).

Information	Descriptions
Main use	High magnification imaging and composition (elemental) mapping.
Destructive	No, some electron beam damage.
Magnification range	10-300 000 ×; 5 000-100 000 × is the typical operating range.
Beam energy range	500 eV-50 keV; typically 20-30 keV
Sample requirements	Minimal, occasionally must be coated with a conducting film; must be vacuum compatible.
Sample size	Less than 0.1 nm, up to 10 cm or more.
Lateral resolution	1-50 nm in secondary electron mode.
Depth sampled	Varies from a few nm to a few µm, depending upon the accelerating voltage and the mode of analysis.
Bonding information	No. Depth profiling capabilities only indirect.

Fundamentals and theoretical details

In the technique of scanning electron microscopy (SEM), the image is obtained by scanning a finely focused probe in a raster pattern on the specimen surface in synchrony with writing the detector signal into a matrix to form a digital image. Magnification is determined by the ratio of the area scanned to the display area. The most commonly used imaging mode makes use of secondary electrons (SEs) that are emitted when the sample is excited by the

electron beam. These are low energy electrons (0-100 eV), making their collection very easy by means of an appropriately biased scintillator. Due to the low energy, the electron have a small mean free path ensuring that the signal comes from the surface region of the specimen. Another imaging mode within an SEM makes use of backscattered electrons (BSEs). These electrons have energies comparable to those in the incident beam (1-30 keV) and hence have larger mean free paths. Therefore, the signal is less sensitive to the surface topography, and instead the image intensity depends on the composition of the specimen. The higher energies of the BSEs make them more difficult to collect than the low energy SEs, which can be collected efficiently by applying a bias voltage to a grid in front of the detector. Resolution in the SEM is determined by the size of the incident electron beam and the beam-specimen interactions (Datye, Hansen, & Helveg, 2008).

Measurement conditions: The surface morphology of the samples was studied by using a Quanta 200 FEI FESEM instrument. The powder samples were adhered to the aluminium made stub using a small piece of carbon conductive tape before loaded to the sample chamber of the instrument. The detailed parameters of the measurement were as follow:

Accelerating voltage : 5 kV

Vacuum mode : High vacuum

Working distance : 8-10 mm

Spot size : 3

Type of detector : LFD

Cone : X-ray

(c) Transmission Electron Microscopy (TEM)

In this analysis, a thin solid specimen (≤ 200 nm thick) is bombarded in vacuum with a highly-focused, monoenergetic beam of electrons. The electromagnetic lenses then magnifies this transmitted electron signal and the diffracted electrons are observed in the form of a diffraction pattern beneath the specimen. Transmitted electrons form images from small regions of sample that contain contrast, due to scattering mechanisms associated with interactions between electrons and the atomic constituents of the sample. Analysis of transmitted electron images yields information about atomic structure and defects present in the material (Brundle, et al., 1992).

Table 3.10: Brief summary of TEM technique (Brundle, et al., 1992).

Information	Descriptions
Main use	Atomic structure and microstructural analysis of solid materials, providing high lateral resolution.
Destructive	Yes, during specimen preparation
Accuracy	Lattice parameters to four significant figures using convergent beam diffraction.
Detection Limits	One monolayer for relatively high Z-materials
Sample requirements	Solid conductors and coated insulators. Typically 3 mm diameter, < 200 nm thick in the center.
Chemical bonding information	Sometimes, indirectly from diffraction and image simulation.
Lateral resolution	Better than 0.2 nm on some instruments.
Depth resolution	None, except there are techniques that measure sample thickness.

Fundamentals and theoretical details

In TEM, a thin specimen is irradiated with a parallel electron beam and magnified images of the sample are formed by combining the transmitted electrons by means of an electromagnetic objective lens. The lens produce a 2D diffraction pattern of the sample in its focal plane and these diffracted beams recombine to form the image. A magnified image or the diffraction pattern on a detection device (CCD camera or photographic film) is observed by varying the excitation of a series of projection lenses. The most commonly used TEM instruments operate in the 100-400 KV range; the higher the energy, the better the resolution (Datye, et al., 2008). TEM offers two operating modes: conventional TEM (CTEM) and high resolution TEM (HRTEM). In CTEM, two imaging modes are possible: bright field and dark field. In bright field imaging, all diffracted electrons are excluded by the aperture in forming the image. In order to detect the presence of metallic particles, this image mode is preferred. If the image is formed from diffracted electrons alone and the central beam is excluded by the objective aperture, a dark field image is obtained. Two beam imaging refers to the condition where the crystal is oriented to yield transmitted and diffracted beams of equal intensity. The bright field, dark field, and two beam imaging modes are broadly applied in studying defects and morphology of thin crystals (Smith, 2005; Hirsch, Howie, Nicholson, Pashley, & Whelan, 1965). Meanwhile, HRTEM technique is performed using an objective aperture which allows diffracted beams to interfere with the axial transmitted beam to form the image. Phase contrast imaging is the preferred imaging mode for resolving the atomic lattice of the specimen (Datye, et al., 2008).

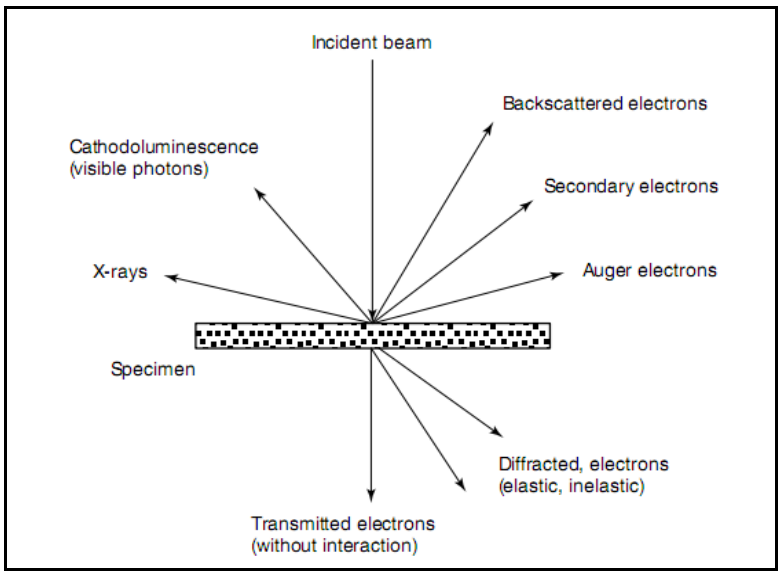

Figure 3.5: Interaction of an electron beam with a thin foil (Karlik, 2001).

Measurement conditions: The TEM specimens were prepared without using any liquids on Ni grids covered with amorphous carbon film. A Philips CM200FEG microscope operated at 200 kV and equipped with a field emission gun, the Gatan imaging filter and EDAX spectrometer was used in this analysis. For the particle size measurements and phase identification images of representative areas of the sample were taken at different magnifications with a CCD camera, and selected image areas were processed to obtain the power spectra (square of the Fourier transform of the image). The power spectra (PS) were used for measuring interplanar distances (+/- 0.5 %) and angles (+/- 0.5 °) for phase identification.

(c) Nitrogen Adsorption Measurement (BET)

Physical adsorption isotherms are measured near the boiling point of a gas (e.g. nitrogen at 77 K). From these isotherms, the amount of gas needed to form a monolayer can be determined. If the area occupied by each adsorbed gas molecule is known, then the surface area can be determined for all finely divided solids, regardless of their chemical

composition. The summary of the description of this technique is shown below (Brundle, et al., 1992):

Table 3.11: Brief summary of physisorption measurement (Brundle, et al., 1992).

Information	Descriptions
Range of elements	Not element specific.
Sample requirements	Vacuum compatible solids, stable to 200 °C, any shape.
Destructive	No.
Chemical bonding information	None.
Depth examined	Surface adsorbed layers only.
Detection limits	Above about 1 m^2/g.
Precision	1 % or better.
Quantification	Standards are available.
Main use	Surface areas of any stable solids, e.g. oxides used as catalyst supports and carbon black.

Fundamentals and theoretical details

Gas adsorption measurements are widely used for determining the surface area and pore size distribution of a variety of different solid materials, such as industrial adsorbents, catalysts, pigments, ceramics, and building materials. Physisorption (physical adsorption) is a general interfacial phenomenon which occurs whenever a gas (the adsorptive) is brought into contact with the surface of a solid (the adsorbent). The forces involved in physisorption include the long range London dispersion forces and the short range intermolecular repulsion. The amount, *n*, of gas adsorbed by unit mass of the adsorbent is dependent on the equilibrium pressure, *p*, the temperature, *T*, and the nature of the gas-solid system. If the particular gas is below its critical temperature and the adsorbent is

maintained at a constant temperature, the adsorption isotherm for the given gas-solid system is

$$n = f\left(\frac{p}{p^0}\right)_T$$

where p^0 is the saturation pressure of the adsorptive at *T*. The adsorption isotherm is thus the relationship, usually presented in graphical form, between the amount adsorbed and the equilibrium pressure or relative pressure, at the known temperature. The first step in the interpretation of a physisorption isotherm is inspection of its shape (Neimark, K. S. W. Sing, & Thommes, 2008). The classification of physisorption isotherms was proposed by IUPAC (Sing, et al., 1985).

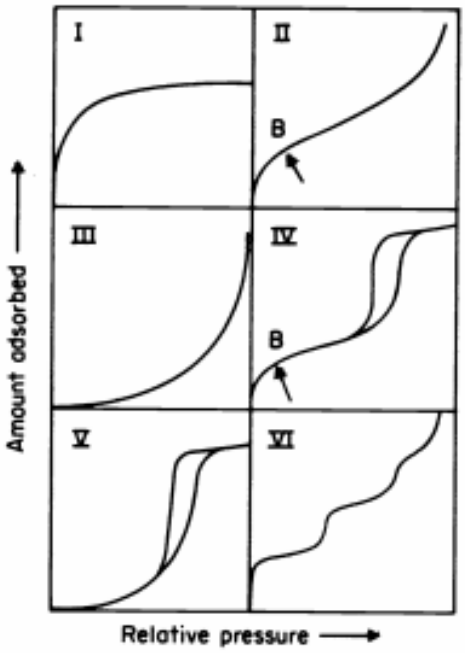

Figure 3.6 : Types of physisorption isotherms (Sing, et al., 1985).

Table 3.12: Classification of physisorption isotherms (Neimark, et al., 2008; Sing, et al., 1985).

Type of Isotherms	Descriptions
Reversible Type I	Given by microporous adsorbents such as zeolites and many activated carbons. The limiting uptake at the plateau is maily dependent on the accessible micropore volume rather than on the internal surface area. If the plateau is almost flat, multilayer adsorption is only possible on a small external surface. A steep uptake at very low p/p^0 is due to enhanced adsorbent-adsorbate interactions in ultramicropores, resulting in micropore filling at very low p/p^0.
Reversible Type II	Given by the physisorption of gases on most non-porous or macroporous adsorbents. The shape is the result of unrestricted monolayer-multilayer adsorption up to high p/p^0. If the knee is sharp, point B- the beginning of the middle almost linear section- usually corresponds to the completion of monolayer coverage. A more gradual curvature (less distinctive point B) is an indication of a significant amount of overlap of monolayer coverage and the onset of multilayer adsorption.
Reversible Type III	Is convex to the p/p^0 axis over its entire range and therefore does not exhibit a Point B. Isotherms of this type are not common, but there are a number of systems (e.g. nitrogen on polyethylene) which give isotherms with gradual curvature and an indistinct Point B. In such cases, the adsorbate-adsorbate interactions play an important role.
Type IV	Given by mesoporous adsorbents (e.g. many oxide gels). The initial monolayer-multilayer adsorption on the mesopore walls is followed by capillary condensation. Characteristic feature of most Type IV isotherms is the appearance of H1 or H2 hysteresis loops.
Type V	Is uncommon; is related to the type III isotherms in the low p/p^0 range. At higher p/p^0 range, molecular clustering is followed by nanopore filling. Type V water isotherms are given by some activated carbon.
Type VI	Is representative of layer-by-layer adsorption on a highly uniform surface. The step height represents the capacity for each adsorbed layer, whereas the sharpness of the step is dependent on the system and the temperature. The best examples of Type VI isotherms are those obtained with argon or krypton at low temperature on graphitized carbon blacks.

The *Brunauer-Emmett-Teller* (BET) gas adsorption method has become the most widely used standard procedure for the determination of the surface area of finely-divided and porous materials, in spite of the oversimplification of the model on which the theory is based. It is customary to apply the BET equation in the linear form:

$$\frac{p}{n^a(p^0-p\ )} = \frac{1}{n_m^a \cdot C} + \frac{(C-1)}{n_m^a \cdot C}\frac{p}{p^0}$$

where n^a is the amount adsorbed at the relative pressure p/p^0 and $n^a{}_m$ is the monolayer capacity. The BET equation requires a linear relation between $p/\ n^a\ (p^0 - p)$ and p/p^0 (*i.e.* the BET plot). The range of linearity is restricted to a limited part of the isotherm- usually not outside the p/p^0 range of 0.05-0.30. Some adsorption systems give linear (or nearly linear) BET plots over several ranges of p/p^0, but it is only in the region $\theta = 1$ that the BET plot can be expected to yield the true value of $n^a{}_m$. This range is shifted to lower relative pressures in the case of systems having high adsorption energies, especially if the surface is energetically homogeneous, e.g. for the adsorption of nitrogen or argon on graphitized carbon or xenon on clean metal films.

BET method is applied in the calculation of the surface area (often termed the BET area) from the monolayer capacity. This requires knowledge of the average area, a^m (molecular cross-sectional area), occupied by the adsorbate molecule in the complete monolayer. Thus,

$$A_s(BET) = n_m^a \cdot L \cdot a_m$$

and

$$a^s(BET)\ =\ A_s\ (BET)/m$$

where $A_s\ (BET)$ and $a^s\ (BET)$ are the total and specific surface areas, respectively, of the adsorbent (of mass m) and L is the Avogadro constant. At the present time, nitrogen is

generally considered to be the most suitable adsorptive for surface area determination and it is usually assumed that the BET monolayer is close-packed, giving $a_m(N_2) = 0.162$ nm^2 at 77 K. With a wide range of adsorbents it appears that the use of this value leads to BET areas which are within 20 % of the true surface areas. In view the fact that the full nitrogen isotherms may be conveniently measured at temperatures ≈ 77 K, it is recommended that nitrogen should continue to be used for the determination of both surface area and mesopore size distribution. The standard BET procedure requires the measurement of at least three and preferably five or more points in the appropriate pressure range on the N_2 adsorption isotherm at the normal boiling point of liquid nitrogen. If the standard BET procedure is to be used, it should be established that monolayer-multilayer formation is operative and is not accompanied by micropore filling, which is usually associated with an increase in the value of C (> 200, say). It should be appreciated that the BET analysis does not take into account the possibility of micropore filling or penetration into cavities of molecular size. These effects can thus falsify the BET surface areas and in case of doubt their absence should be checked by means of an empirical method of isotherm analysis or by using surface area reference samples (Sing, et al., 1985).

Measurement conditions: The specific surface area, total pore volume and average pore size of the samples were determined by using Quantachrome Autosorb Automated Sorption System (for AS-3 and AS-6, Version 1.23) instrument according to *Brunauer, Emmer, Teller* (BET) theory. The sample of known weight was placed in a sample tube of known volume and degassed under vacuum for 5 hours at 120 °C. After outgassing, the sample was weighed again to record the actual sample weight. The sample tube was then placed in the analysis station, cooled in liquid nitrogen. A known amount of nitrogen gas with cross

section area of 16.2 Å was introduced into the sample. N_2 adsorption/ desorption isotherms were obtained after the measurement.

3.3.2 Chemical Analysis

(a) X-Ray Fluorescence (XRF)

In X-Ray Fluorescence (XRF), an X-ray beam is used to irradiate a specimen, and the emitted fluorescent X-rays are analyzed with a crystal spectrometer and scintillation or proportional counter. The fluorescent radiation normally is diffracted by a crystal at different angles to separate the X-ray wavelengths and therefore to identify the elements; concentrations are determined from the peak intensities. For thin films XRF intensity-composition-thickness equations derived from first principles are used for the precision determination of composition and thickness. This can be done also for each individual layer of multiple-layer films. A brief description of XRF technique is explained as below (Brundle, et al., 1992):

Table 3.13: Brief summary of XRF technique (Brundle, et al., 1992).

Information	Descriptions
Range of elements	All but low Z elements: H, He, and Li.
Accuracy	± 1 % for composition, ± 3 % for thickness.
Destructive	No.
Depth sampled	Normally in the 10 µm range, but can be a few tens of Å in the total reflection range.
Depth profiling	Normally no, but possible using variable-incidence X rays.
Detection limits	Normally 0.1 % in concentration.
Sensitivity	10-10^5 Å in thickness can be examined.
Lateral resolution	Normally none, but down to 10 µm using a microbeam.
Chemical bond information	Normally no, but can be obtained from soft X-ray spectra.
Sample requirements	≤ 5.0 cm in diameter.
Main use	Identification of elements; determination of composition and thickness.

Fundamentals and theoretical details

In the bulk analysis of catalytic materials by classical wet chemistry methods, gravimetric and titrimetric techniques are employed (Beamish, 1966; Beamish & Van Loon, 1972; Beamish, Van Loon, & Lewis, 1977). However, these methods are time consuming and a broad spectrum of practical expertise and experimental skills of well-trained specialists has to be provided in the chemical laboratory. During the last few decades, improved performance in instrumental analytical techniques was achieved. Typical requirements are to provide, as far as possible, a non-destructive, rapid analysis, with easy calibration and high precision and accuracy (Albers, 2008). Excellent agreement of analytical data obtained by both gravimetric and spectroscopic techniques (XRF, ICP) was reported by industrial (Wissmann & Nordheim, 1993) and university (Nogier, 1994; Serwicka, 2000) laboratories. In XRF, the catalyst is irradiated with X-rays from a primary source and electrons from inner levels are released. The remaining positive hole is filled within 10^{-15} s by electrons from upper levels, leading to the emission of X-ray photons characteristic of the element. The X-ray fluorescence is measured with wavelength or energy dispersive detectors. XRF allows an accurate and simultaneous determination of major and minor elements in a catalyst over a wide concentration range (from 100 % down to 0.001-0.01 %). Qualitative and quantitative analysis of solid and liquid samples is possible. Usually, a powdered solid sample is pressed into a wafer or a sample is mixed with an organic binder such as a copolymer-wax and pressed into a pellet for analysis. Usually, semiquantitative information is sufficient as a compromise between speed of analysis and the actually useful precision. XRF has the advantage that a sample does not have to be dissolved. For a semiquantitative XRF analysis, no standards are needed. The costs of the analysis are lower

than for ICP techniques. Wavelength dispersive XRF is faster (because of the easier sample preparation) than ICP, but less sensitive (Albers, 2008).

Measuring conditions: The bulk elemental composition of the samples was performed by employing a Bruker X-ray Fluorenscence Model S4 Explorer equipped with *Spectra*^{plus} V1.64 software. The measurement was done using X-ray generator source operating at 1 kW at ambient temperature. The analysis was carried out using semi-quantitative method. The sample was grinded into fine powder and pressed into a pellet (pressure) and placed onto the sample holder before loaded to the sample chamber of the instrument. The accuracy of the XRF analysis is typically from 0.1 to 1 % in relative.

(b) Energy Dispersive X-Ray Spectroscopy (EDX)

When the atoms in a material are ionized by a high energy radiation they emit characteristic X-rays. EDX is an acronym describing a technique of X-ray spectroscopy that is based on the collection and energy dispersion of characteristic X-rays. An EDX system consists of a source high energy radiation, usually electrons; a sample; a solid state detector, usually made from lithium-drifted silicon, Si (Li); and signal processing electronics. EDX spectrometers are most frequently attached to electron column instruments. X-rays that enter the Si (Li) detector are converted into signals which can be processed by the electronics into an X-ray energy histogram. This X-ray spectrum consists of a series of peaks representative of the type and relative amount of each element in the sample. The number of counts in each peak may be further converted into elemental weight concentration either by comparison with standards or by standardless calculations. The summary of this technique is described as follow (Brundle, et al., 1992):

Table 3.14: Brief summary of EDX technique (Brundle, et al., 1992).

Information	Descriptions
Range of elements	Boron to uranium
Destructive	No
Chemical Bonding information	not readily available
Quantification	Best with standards, although standardless methods are widely used
Accuracy	Nominally 4-5 %, relative, for concentrations > 5 % wt.
Detection limits	100-200 ppm for isolated peaks in elements with Z > 11, 1- 2 % wt. for low Z and overlapped peaks
Lateral resolution	0.5-1 µm for bulk samples; as small as 1 nm for thin samples in STEM
Depth sampled	0.02 to µm, depending on Z and keV
Imaging/ mapping	in SEM, EPMA and STEM
Sample requirements	Solids, powders, and composites; size limited only by the stage in SEM, EPMA and XRF; liquids in XRF; 3 mm diameter thin foils in TEM.
Main use	To add analytical capability to SEM, EPMA and TEM

Fundamentals and theoretical details

Energy dispersive X-ray (EDX) analysis, also known as energy dispersive spectroscopy (EDS), is the most commonly used analytical technique in a microscope. Electron excitation at the voltages typically used in microscopes cause ionization within the sample leading to X-ray emission that can be analyzed with a solid-state energy dispersive detector (Datye, et al., 2008). X-rays are produced as a result of the ionization of an atom by high energy radiation where an inner shell electron is removed. To return the ionized atom to its ground state, an electron from a higher energy outer shell fills the vacant inner shell and, in the process, releases an amount of energy equal to the potential energy difference between the two shells. The excess energy which is unique for every atomic transition will be

emitted as an Auger electron. Thus, in an atom with many shells, many emissions can result from a single primary ionization. A spectrum can be obtained from almost any sample, as long as it can be put on the specimen stage of this microscope. The choice of accelerating voltage should be determined by the type of sample one is studying, since the X-ray generation volume depends on the electron range in the material. The ultimate goal in using an EDS analytical system is to be able to measure the concentrations of all the elements in the sample. To this end, a series of measurement are made in which the peak intensity from each element in the sample is compared to the peak intensity obtained from a reference standard using the same operation conditions. A major advantage of energy dispersive spectrometer is that it can be positioned very close to the sample and can present a large solid angle for the collection of emitted X-rays. With EDS, more X-ray photons will be collected per incident electron. EDS is an extremely powerful analytical technique of special value in conjunction with electron column instruments. In a few seconds a qualitative survey of the elements present in almost any sample can be made, and in only a few minutes' sufficient data can be collected for quantification (Brundle, et al., 1992).

Measuring conditions: The surface elemental composition and elemental mapping of the samples were determined by using INCA Energy 400 software with the images captured by Quanta 200 FEI microscope instrument. The powder samples were adhered to the aluminium made stub using a small piece of carbon conductive tape before loaded to the sample chamber of the instrument. The detailed parameters of the measurement were as following:

Accelerating voltage : 5 kV

Vacuum mode : High vacuum

Type of detector : SATW (silicon)

3.3.3 Thermal Analysis

(a) Thermogravimetric analysis (TGA) coupled to Mass Spectrometry (MS)

Thermogravimetric analysis (TGA) is a technique in which the weight or the mass of a sample is measured as a function of sample temperature or time. Additional technique-mass spectrometry is coupled to TGA to characterize substances by identifying and measuring the intensity of molecular fragment ions of different mass-to-charge ratio (m/z).

Fundamentals and theoretical details

In TGA analysis, the sample is usually heated at a constant heating rate or held at a constant temperature. The choice of the temperature program depends upon the type of information required about the sample. Moreover, the options of the environment employed in the TGA experiment can be reactive, oxidizing, or inert, and the changes in the environment during a measurement can be made when necessary. There are three different designs of thermobalances available as shown in **Figure 3.7**. These days, compensation balances are mostly used. The position of the sample remains the same even when the mass changes with this type of balance. In the horizontal arrangement, simple moving coil systems have the disadvantage that samples that move horizontally while heating which generate an apparent change in mass. Balances are categorized as semicron-(10 μg), micro-(1 μg), or ultramicro- (0.1 μg) balances according to the desirable resolution. Thermogravimetric measurements are influenced by several factors as the following (Gabbott, 2008b):

Table 3.15: Factors which influence thermogravimetric measurements:

Parameters	Descriptions
Method parameters	Heating rate, environment (air, nitrogen, argon; pressure, humidity)
Sample preparation	Sample size, homogeneity and morphology of the sample: coarse crystals, fine powder
Crucible type	Alumina, sapphire, platinum
Instrumental effects	Buoyancy and gas flow. Can be reduced or eliminated by performing blank curve substraction.
Changes in physical properties	Changes in physical properties of the sample during measurement. For example, a change in emissivity (affects the heat transfer within the sample and from the furnace to the sample) or the volume (leads to change in buoyancy)
Artifacts	Sample may 'spit', or move and artefacts caused by such events can be minimized by grinding the sample or covering it with a platinum mesh.

The results of a TGA measurement are usually displayed as a TGA curve in which mass or per cent mass is plotted against temperature or time. An alternative presentation is to use the first derivative of the TGA curve with respect to temperature or time. This exhibits the rate at which the mass change and is known as the differential thermogravimetric or DTG curve. Mass changes when the sample looses material in different ways or reacts with the surrounding environment. This generates steps in the TGA curve or peaks in the DTG curve. A sample can lose, or gain mass with the different effects as the following (Gabbott, 2008b):

- Evaporation of volatile constituents; drying; desorption and adsorption of gases, moisture and other volatile substances; loss of water of crystallization.
- Oxidation of metals in air or oxygen.
- Oxidative decomposition of organic substances in air or oxygen.
- Thermal decomposition in an inert atmosphere with the formation of gaseous products.
- Uptake or loss of water in a humidity controlled experiment.

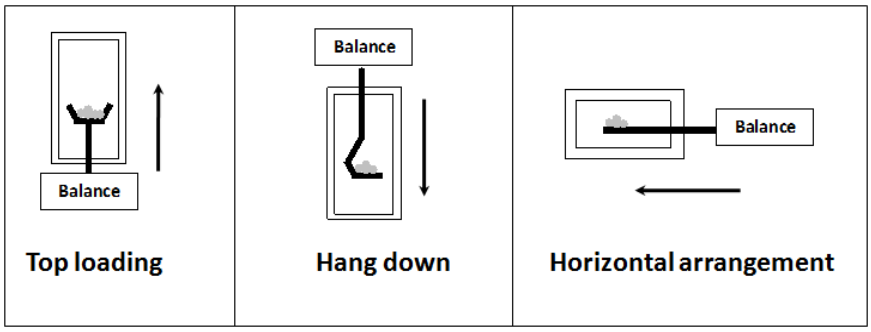

Figure 3.7: Thermobalance designs in different arrangements.

TGA is a technique which provides quantitative information on the change in mass of a sample as a function of time as it is heated, cooled or held at constant temperature. However, TGA by itself is not an identification technique for unknown samples. Combination of TGA and mass spectrometry (MS) allows the nature of the gaseous products formed to be investigated in further details. The schematic diagram of thermogravimetric analysis coupled to mass spectrometry is illustrated in **Figure 3.8**. When several compounds are evolved, the MS can track their evolution profiles as the spectra generated can be used to characterize the substance or class of substance through spectral interpretation and comparison with database reference spectra. Decomposition pathways can therefore be illuminated. The gas molecules entering the mass spectrometer from the thermobalance are first ionized in the ion source and the positive molecular ion and fragment ions formed are then separated according to their m/z value by a combination of magnetic and electrostatic fields. In a TGA-MS system, the mass spectrometer is usually set to monitor individual m/z values that are characteristic of specific structural features (Gabbott, 2008b).

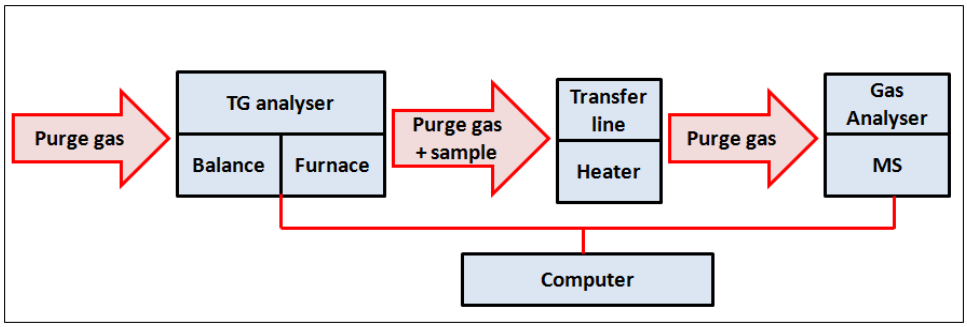

Figure 3.8: Schematic diagram of thermogravimetric analysis coupled to mass spectrometry (TGA-MS).

Measuring conditions: The thermal behavior of the phase pure samples was analyzed with TGA-MS/ DSC techniques using NETZSCH STA 449C device, equipped with an ultra-microbalance and thermocouple for direct measurement of the temperature at the sample crucible. STA (Simultaneous Thermal Analysis) here refers to the application of two techniques to a single sample analyzed at the same time. The TGA/ DSC results were acquired using this instrument with Al_2O_3 crucibles. A heating rate of 5 K/ min was used in the experiments. Argon gas of 30 cm^3 /min was used as protective gas of TGA-DSC furnace. The NETZSCH STA 449 C TGA-DSC unit is coupled with Quadrupole Mass Spectrometer (Thermostar, Balzers) in order to characterize the evolved gas products.

The thermal studies of the phase pure materials were conducted in two different environments as shown in the following:

Inert environment: A linear ramp from 298-873 K at heating rate of 5 K/ min, in the flow of 100 % Ar gas at 70 cm^3 /min.

Oxidic environment: A linear ramp from 298-873 K at heating rate of 5 K/ min, in 21 % O_2 gas (21 cm^3 /min) and Ar gas (49 cm^3 /min) flow.

(b) Differential Scanning Calorimetry (DSC)

A DSC analyser measures the energy changes that occur as a sample is heated, cooled or held isothermally, together with the temperature at which these changes occur. The energy changes can measure the transitions that occur in the sample quantitatively. One of the advantages of DSC is that samples are very easily encapsulated, usually with little or no preparation, so that measurements can be quickly and easily made. It has found use in many applications which cover polymers and plastics, food and pharmaceuticals, glasses and ceramics, proteins, and life science materials (Gabbott, 2008a).

Fundamentals and theoretical details

There are two types of DSC designs are commonly available, namely power compensation DSC, and heat flux DSC. For power compensation DSC, it has two small identical furnaces, one for the sample and one for the reference (normally an empty pan). These are both heated at a pre-programmed heating (or cooling) rate, the difference in energy flowing into the sample furnace is compared to the inert reference and plotted as a function of temperature or time. This design measures flow of energy directly in *mW* or *J/s* and the fundamental equation involved is:

$$DSC\ signal\ (W/g) = Heat\ capacity\ (J/kg) \times Scanning\ rate\ (K/s)$$

$$dH/dt = dH/dT \times dT/dt$$

Hence, the raw heat flow signal can be viewed as a form of heat capacity. Practically, it reflects the changes occurring in heat capacity, and the absolute value is obtained when the method used takes into account the contribution of the empty pans and reference together with the scan rate. This technique measures energy changes directly (Gabbott, 2008a).

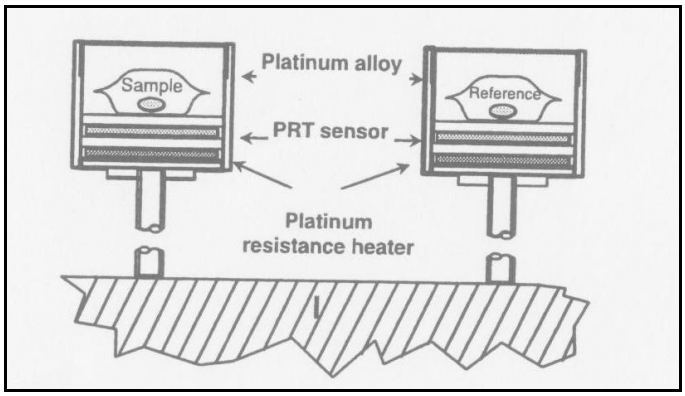

Figure 3.9: Diagram of a power compensation DSC (Gabbott, 2008a).

Another design of DSC is heat flux DSC where it is of a single furnace design with a temperature sensor (or multiple sensors) for each of the sample and reference pans placed within the same furnace. When transitions in the sample are detected, a temperature difference is created between sample and reference. It is the difference in temperature or Δt signal that is the basic parameter measured. The difference in temperature is converted to an energy equivalent by the analyzer giving the familiar DSC signal in *mW* (Gabbott, 2008a).

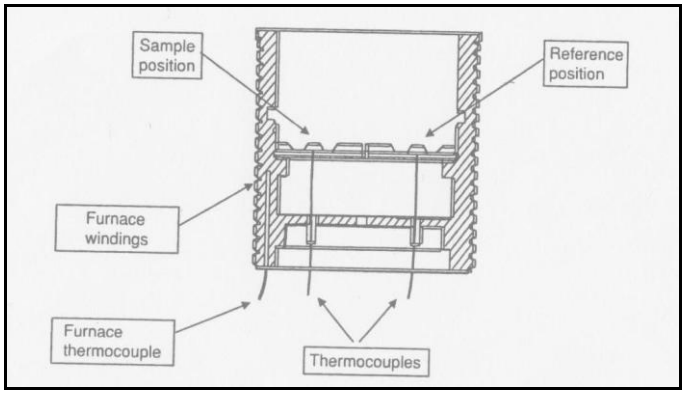

Figure 3.10: Diagram of a heat flux DSC (Gabbott, 2008a).

Measuring conditions: The measuring conditions of DSC analysis are similar with TGA-MS analysis. Please refer **Section 3.3.3 (a) – Measuring Conditions** for details.

CHAPTER 4

RESULTS & DISCUSSION

All the samples discussed in this chapter have been reproduced at least three times. The related results and characterization data of the samples are demonstrated in 5 different sections in this chapter, namely **4.1 Effects of synthesis temperature**, **4.2 Effects of Cu: S mole ratio**, **4.3 Effects of synthesis time**, **4.4 Further studies on phase pure copper sulfides**, and **4.5 Phase stability studies of *covellite***. The results are carefully interpreted and discussed in details in the respective sections.

4. 1 Effects of Synthesis Temperature

Hydrothermal process of temperature vs time profile at different temperatures is shown in **Figure 4.1**. The plot indicates that the temperature was well controlled during the 12 hours synthesis. The temperatures remained constant throughout the synthesis time for each run but varied by 10 °C from the nominal temperature for runs conducted at 65.0 °C and above. The variation of the synthesis temperature mentioned above is most probably due to the uneven heating in the furnace at high temperature. This led to the unstable temperature reading recorded during thermocouple measurement.

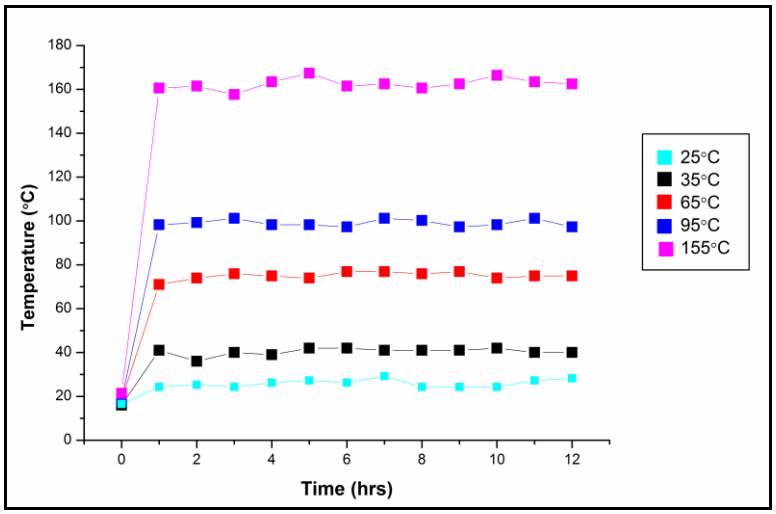

Figure 4.1: Temperature vs time profile of hydrothermal reaction measured by thermocouple.

4. 1. 1 Powder X-ray Diffraction

Powder XRD patterns of the products prepared at different synthesis temperatures are shown in **Figure 4.2**. The fittings of the respective samples' diffractograms are displayed in *Appendix A*. Meanwhile, **Table 4.1** summarizes the results of *Rietveld* quantification analysis which indicates the relative amount of crystal compounds found in the products. From **Table 4.1**, the *Rietveld* quantification analysis shows that CuS is present for all synthesis temperatures. This reveals that CuS is a thermodynamically stable product which can be easily obtained. At 25.0 °C, the major crystal compound formed is a royal blue mineral, *krohnkite* $[Na_2Cu(SO_4)_2(H_2O)_2]$, followed by *covellite* (CuS), pentahydrate copper sulfate ($CuSO_4.5H_2O$), and cyclooctasulfur (S_8). The powder XRD pattern as shown in **Figure 4.2(b)** indicates that the same crystal compounds were found in a higher temperature (35.0 °C) with almost similar amounts except for the presence of trihydrate copper sulfate ($CuSO_4.3H_2O$) which was not found at 25 °C. The products at room temperature and 35.0 °C seem to give similar crystal phases since 5-10 °C does not make a significant temperature range. However, it is found that CuS was not present as a single

phase crystal product at low temperature. The percentage amount of CuS can be increased significantly at higher temperature. This is due to the fast rate (kinetic reason) of formation of CuS at higher temperature. When the temperature was increased to 65.0 and 95.0 °C, only poorly crystalline copper sulfide and cyclooctasulfur (S_8) molecules were detected in the powder. As the temperature was increased to 155.0 °C, a highly crystalline single phase covellite was formed (**Figure 4.2e**). All the characteristic peaks in this pattern correspond well to the phase pure CuS in the space group of *P63/mmc* which can be well indexed to hexagonal *covellite* (PDF 06-464, a= 3.792 Å, c= 16.34 Å). This is further confirmed in the *Rietveld* refinement quantification analysis (**Table 4.1e**) where the pattern matches to 100 % CuS with *ICSD* 63327. No other crystalline phase was detected in the material at this temperature, indicating the high purity of the product synthesized.

Table 4.1: Crystal structures determination by powder XRD for products formed at different temperatures[†].

Sample ID	Set T (°C)	Measured T (°C)	*Rietveld* Quantitative Analysis (ICSD)
H01	25.0	25.0	60 % $Na_2Cu(SO_4)_2(H_2O)_2$ (1915) 23 % CuS (63327) 14 % $CuSO_4.5H_2O$ (4305) 4 % S_8 (412326)
H02	35.0	35.0	57 % $Na_2Cu(SO_4)_2(H_2O)_2$ (1915) 17 % CuS (36155) 17 % $CuSO_4.5H_2O$ (4305) 5 % $CuSO_4.3H_2O$ (34679) 4 % S_8 (412326)
H03	65.0	75.0	93 % CuS (63327) 7 % S_8 (412326)
H04	95.0	105.0	76 % CuS (63327) 24 % S_8 (412326)
H05	155.0	165.0	100% CuS (63327)

[†]*All the syntheses were done with Cu: S mole ratio fixed at 1:2 and synthesis time for 12 hours.*

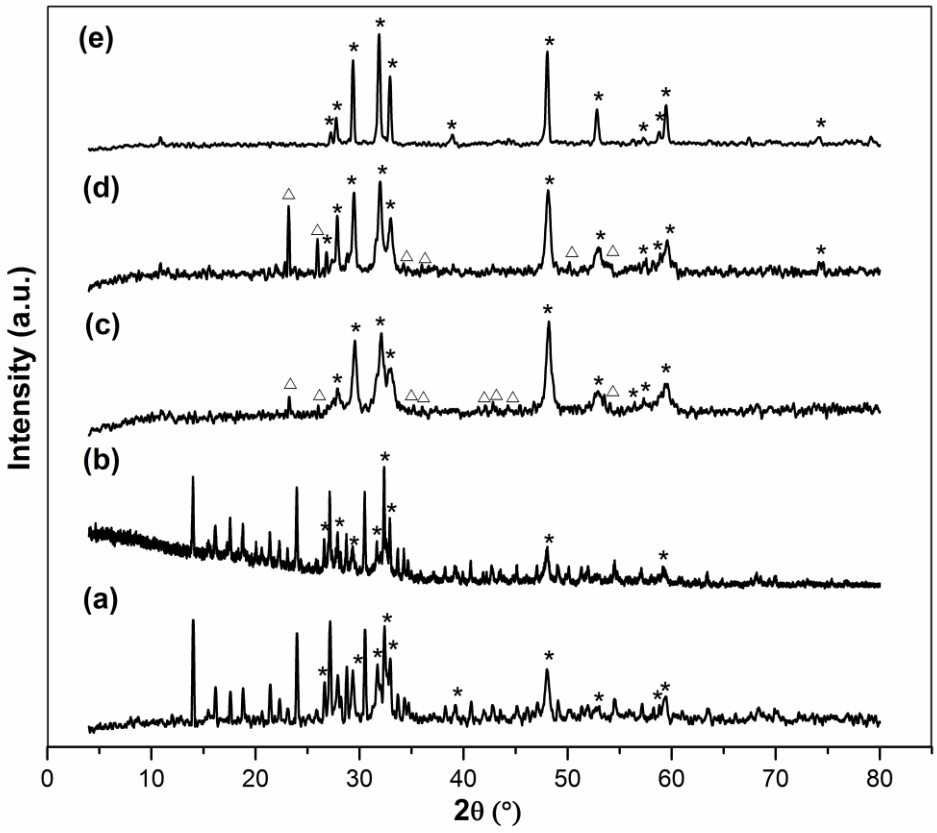

Figure 4.2: Powder X-Ray Diffraction (PXRD) patterns of the as-prepared products at (a) 25.0 °C (b) 35.0 °C (c) 65.0 °C (d) 95.0 °C (e) 155.0 °C
* denotes the characteristic peaks of hexagonal *covellite* (CuS-PDF 06-0464);
$^{\Delta}$ denotes the characteristic peaks of face-centered orthorhombic sulfur (S_8- PDF 86-2600).

4. 1. 2 X-ray Fluorescence Spectroscopy and Energy Dispersive X-ray Spectrometry

The bulk and surface elemental composition of the products formed were determined by X-Ray fluorescence (XRF) and Energy Dispersive X-Ray Spectrometry (EDX) techniques respectively. The details of the EDX analysis for each sample are attached in *Appendix B*. The bulk chemical analysis of the samples prepared at different temperatures is tabulated in **Tables 4.2 and 4.3**. For simplicity, the data tabulated in **Tables 4.2 and 4.3** are redrawn as shown in **Figure 4.3 and Figure 4.4**.The results indicate that the Cu: S ratio from XRF and EDX analyses are in great difference except for the sample formed at 155.0 °C. From

Figure 4.4, it can be spotted that the Cu: S ratio was almost similar at all synthesis temperatures, implying that the distribution of Cu and S was quite even on the surface regardless of the heat applied. However, the XRF result illustrates that the products from 25-95 °C have more sulfur content in bulk (S ratio is more than 1) rather than on the surface. This supports the deduction from *Rietveld* quantification analysis where other sulfur compounds such as cyclooctasulfur, and copper sulfate are present in the respective products. A very crucial point to be mentioned here is that the product prepared at the highest temperature (155.0 °C) shows that the Cu: S ratio is almost 1: 1 determined from XRF and EDX analyses. Both of these analyses explain that indeed CuS compound occurs uniformly on the surface and in bulk which is in good agreement with the stoichiometric formula of *covellite* (CuS).

Table 4.2: XRF analysis of samples formed at different temperatures.

Sample ID	Temp (°C)	Element	Concentration (wt %)	No. of Moles†	Calculated Atomic ratio (Cu / S)†	Cu: S†
H01	25.0	Cu S	52.8 47.2	8.309×10^{-3} 1.472×10^{-2}	0.56	1: 1.77
H02	35.0	Cu S	49.6 50.4	7.804×10^{-3} 1.572×10^{-2}	0.50	1: 2.00
H03	65.0	Cu S	59.3 40.7	9.332×10^{-3} 1.269×10^{-2}	0.74	1: 1.36
H04	95.0	Cu S	46.9 53.1	7.380×10^{-3} 1.656×10^{-2}	0.45	1: 2.24
H05	155.0	Cu S	65.2 34.8	1.026×10^{-2} 1.089×10^{-2}	0.94	1: 1.04

† *For example of calculation, please refer Appendix B.*

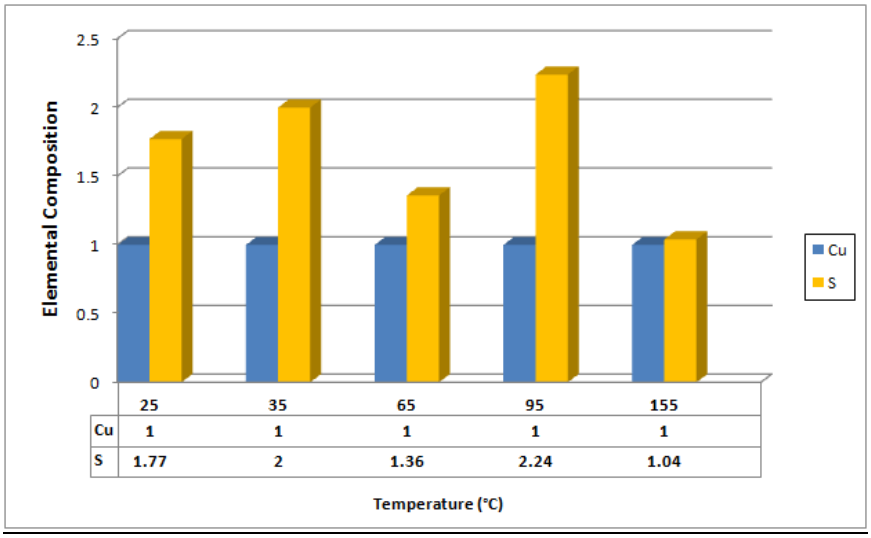

Figure 4.3: XRF analysis of products formed at different synthesis temperatures.

Table 4.3: EDX analysis of samples formed at different temperatures.

Sample ID	Temp (°C)	Element	Conc. (at%-A)	Conc. (at%-B)	Conc. (at%-average)†	Calculated Atomic ratio (Cu / S)†	Cu: S†
H01	25.0	Cu S	47.01 52.99	46.83 53.17	46.92 53.08	0.88	1: 1.13
H02	35.0	Cu S	47.11 52.89	47.79 52.21	47.45 52.55	0.90	1: 1.11
H03	65.0	Cu S	48.84 51.16	49.57 50.43	49.205 50.795	0.97	1: 1.03
H04	95.0	Cu S	48.1 51.9	50.34 49.66	49.22 50.78	0.97	1: 1.03
H05	155.0	Cu S	48.47 51.53	48.06 51.94	48.265 51.735	0.93	1: 1.07

† *For example of calculation, please refer Appendix B.*

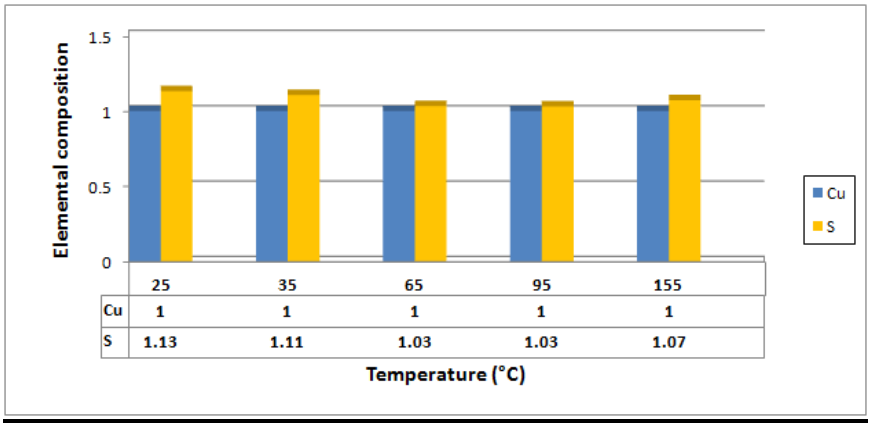

Figure 4.4: EDX analysis of products formed at different synthesis temperatures.

4. 1. 3 Field Emission Scanning Electron Microscopy

Figures 4.5, 4.6, and **4.7** show the change in morphology of the products at 3 different FESEM magnifications, *i.e.* (15000, 30000, 60000 ×). **Figure 4.5(a)** shows the morphology of the powder which resembles the shape of 'paper flower' from *Bougainvillea* Genus. As depicted in the higher magnification of micrograph in **Figure 4.6(a)**, many of the uniform clusters of 'paper flowers' were observed, and each cluster of the 'flower' was actually surrounded by 3 or 4 thin bracts/petals (**Figure 4.7a**).When the synthesis temperature was increased to 35.0 °C, the structure of the 'paper flower' shows changes as seen in **Figure 4.5(b)**. Both of the powder shown in **Figure 4.5 (a)** and **(b)** seem to show similar morphology. However, micrograph 4.5 (b) shows that the number of petals of the 'flower' has decreased, while the size of the petal has significantly increased compared to the one observed in **Figure 4.5 (a)**. A close up view illustrates that there was fine powder tabulated within the petals in **Figure 4.6 (b)**, but this was not found in the product formed at 35.0 °C (**Figure 4.6a**). It is very obvious that as temperature was increased to 65.0 °C, the petal shape was not found in the micrograph. A more agglomerated structure is observed as depicted in **Figure 4.5 (e)** where there are many uniform ball-like particles which are

actually made up of a large amount of rod shape nanocrystallites are observed from the micrograph. Similar structure was found for powder formed at 95.0 °C which is displayed in **Figure 4.5 (d)**. At temperature of 155.0 °C, it is very clear that the as-formed product exhibits a highly agglomerated morphology as depicted in **Figure 4.5 (e)**. Higher magnified images in **Figures 4.6 (e)** and **4.7 (e)** indicate that the particles were essentially built up by several irregular hexagonal shape nanoplates which assembled, and interlaced perpendicular among each other. The hexagonal nanoplates have a mean edge length of *ca.* 1-1.5 μm and an average thickness of *ca.* 50-100 nm.

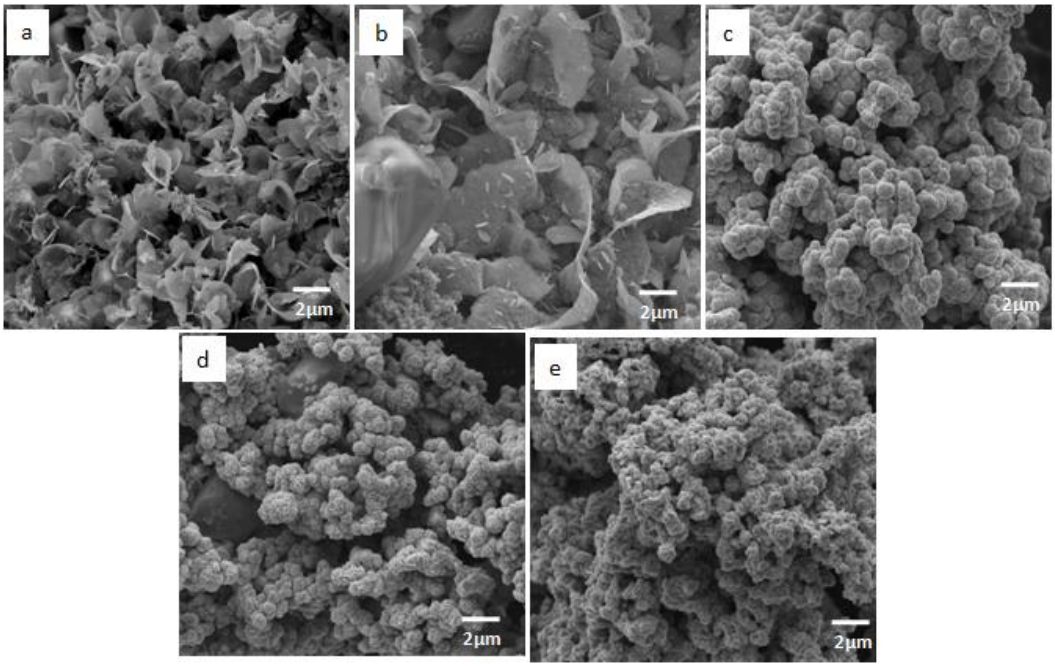

Figure 4.5: FESEM micrographs (15 000 × magnification) of products obtained at (a) 25.0 °C (b) 35.0 °C (c) 65.0 °C (d) 95.0 °C (e) 155.0 °C.

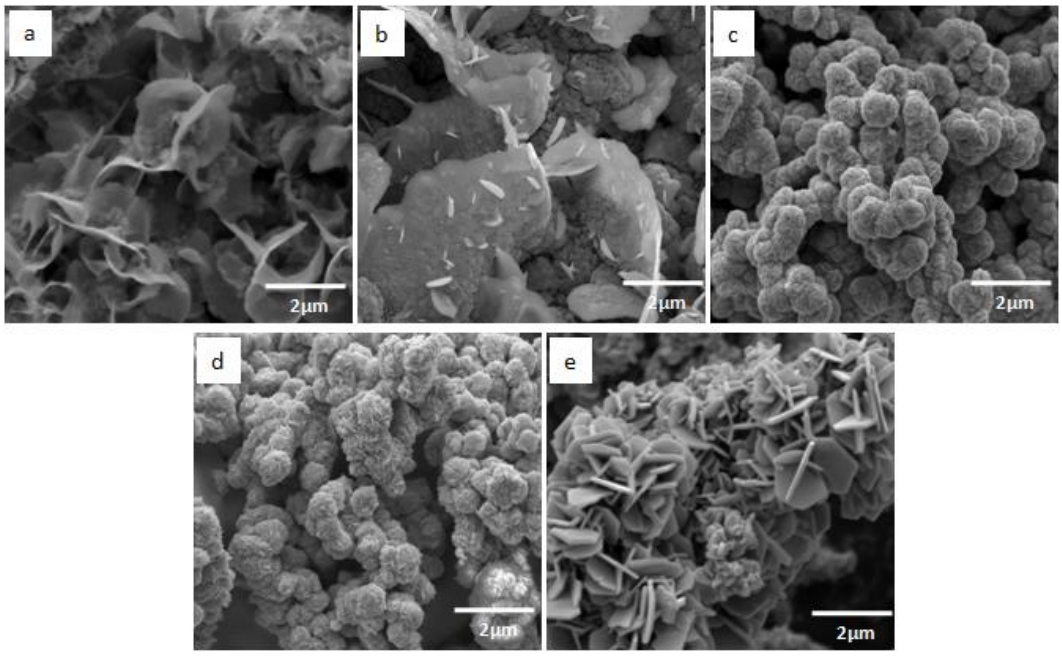

Figure 4.6: FESEM micrographs (30 000 × magnification) of products obtained at temperatures of (a) 25.0 °C (b) 35.0 °C (c) 65.0 °C (d) 95.0 °C (e) 155.0 °C.

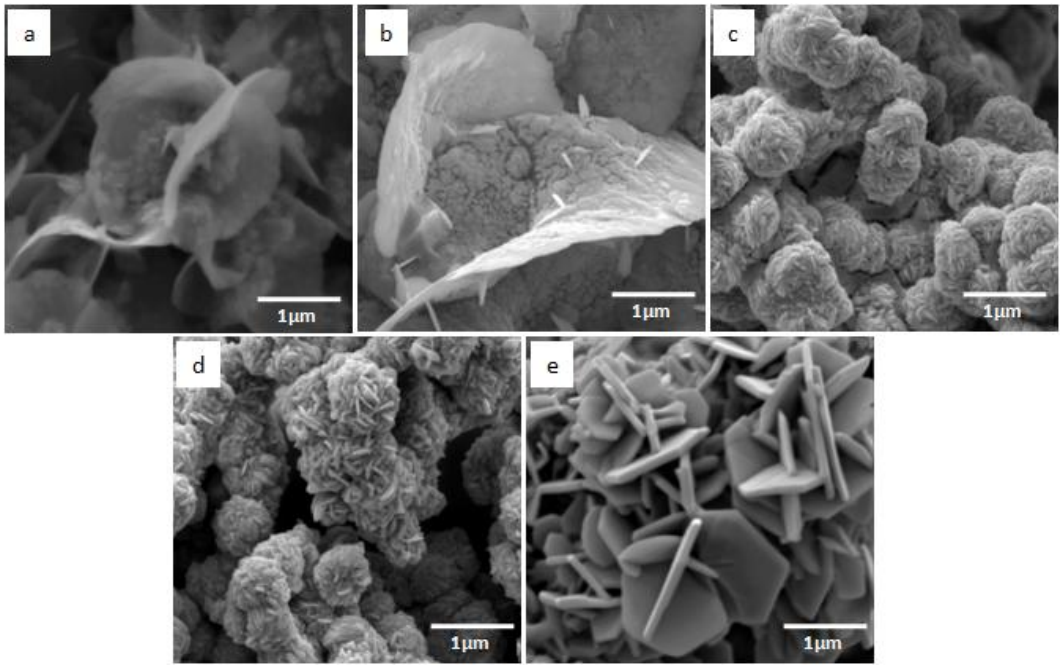

Figure 4.7: FESEM micrographs (60 000 × magnification) of products obtained at (a) 25.0 °C (b) 35.0 °C (c) 65.0 °C (d) 95.0 °C (e) 155.0 °C.

4.1.4 Discussion

The investigations on the effects of synthesis temperature, CuS is found to be formed for the entire range of studied temperatures (25-155 °C). From PXRD, pure phase CuS can only be found at 155 °C. This indicates that 155 °C might be the optimum temperature to prepare CuS as mixed phases of $Na_2Cu(SO_4)_2(H_2O)_2$, $CuSO_4$,and S_8 were observed for other synthesis temperatures (25-95 °C). The XRF and EDX analyses also show that the product at 155 °C have the calculated atomic Cu: S mol ratio of 1: 1, which is in good correlation with the stoichiometric of *covellite* (CuS). On the other hand, the products formed at 25-95 °C show relatively same atomic ratio of Cu: S on the surface, but the XRF results implied a significant difference in Cu: S atomic ratio. This might due to the presence of the mixed phase products which give rise to the unusual Cu: S atomic ratio in the bulk. With reference to the result of FESEM, the only single morphology (hexagonal nanoplate) found in the product synthesized at 155 °C signified that it is complementary to the PXRD result where only single hexagonal phase of *covellite* is identified. This proves that the results from PXRD, FESEM, XRF, and EDX are in good agreement. The assorted morphologies observed in the range of 25-95 °C might correspond to the mixed phases found in the PXRD.

In comparison to the former investigations carried out by other research groups, synthesis temperature was found to influence the phase purity (Wan, et al., 2004), morphology (Cheng, et al., 2010; Roy, et al., 2008; Wang, et al., 2009; Zhang, et al., 2006; Zou, Zhang, Zhang, Zhao, Xu, et al., 2007), crystal size (Gautam & Mukherjee, 2006; Qin, et al., 2005), crystallinity (Wu, Yu, Chen, Liu, & Liu, 2006; Zhang, Qiao, et al., 2004), and yield (Zhang, Qiao, et al., 2004) of the copper sulfides formed. In the research conducted

by *Wan et al.,* they demonstrated that the most suitable temperature range for the fabrication of CuS hollow sphere was 100-150 °C and the sample recovered below 50 °C consisted of a mixed phase (Wan, et al., 2004). On the contrary, *Z. Cheng et al.* indicated that increasing synthesis temperature is favorable for the formation of the flower-like CuS nanoarchitectures by employing copper sulfate, carbon bisulfide, poly (N-vinyl-2-pyrrolidone) and sodium hydroxide as the starting materials (Cheng, et al., 2010). For the work done by *Qin et al.*, they discovered that increasing the synthesis temperature most likely resulted in the faster growth of the crystal size when copper sulfide was prepared using copper nitrate, thiourea, with a mixed solution of ethanol and water (Qin, et al., 2005). While, some researchers have implied that the crystallinity and the yield of the obtained copper sulfide can be enhanced with higher synthesis temperature (Zhang, Qiao, et al., 2004). However, in this work, synthesis temperature is found to influence the phase purity and the morphology of the end products synthesized. Higher temperature favors the formation of phase pure compound as more energy is supplied to the system which aids in higher diffusion rates of ions. As a result, this accelerates the crystal growth and reaction rate of copper sulfide formation. This can be associated to the phenomenon of *Ostwald Ripening* where this involves the dissolution of small crystals or sol particles and the redeposition of the dissolved species on the surfaces of larger crystals or sol particles. This process happens due to the higher surface energy which is possessed by the smaller particles, hence a higher total Gibbs energy, than larger particles. This gives rise to an apparent higher solubility of smaller particles compared to the larger ones (IUPAC, 2007).

Proposed Crystal Growth Mechanism

Covellite mineral (CuS) is always regarded as a copper (II) sulfide system. This simple assignment is inaccurate due to the Cu-S bonds are somehow covalent rather than ionic in character. X-ray studies showed different Cu environments are present in the system. The crystal structure of *covellite* can be assigned as a mixed valence formula $(Cu^{+})_2(Cu^{2+})(S^{2-})(S_2)^{2-}$ where both Cu(I) and Cu(II) are present in the system (Goble, 1985). A mechanism describing the formation and crystal growth of CuS (*covellite*) has been proposed based on the information obtained from the temperature and time effects measured in this study. CuS (*covellite*) is a thermodynamically stable compound that can be formed at room temperature. This fact is evidenced by PXRD quantification analysis where CuS was found from the product formed at all synthesis temperatures. As observed from the quantification table (**Table 4.1**), mixture of CuS and other compounds ($Na_2Cu(SO_4)_2(H_2O)_2$, $CuSO_4$, and S_8) were found at synthesis temperature from 25 to 95 °C. Since CuS is the only end product obtained at 155 °C, this suggests that activated pathway which requires excessive heat from the higher synthesis temperature has led to the formation of phase pure CuS.

The hydrolysis of thiosulfate will generate sulfur species that can react with Cu(II) to produce Cu_xS. However, this is a very slow process at ambient conditions and it might take around a week to produce a black-green $Cu_{2-x}S$ at room temperature and ambient pressure (Yang & Xiang, 2005). *Ni et al.* (Ni, et al., 2004; Ni, et al., 2004) has found that the hydrolysis of $Na_2S_2O_3$ could be facilitated by microwave irradiation, probably by the resulting heating effect. For these reasons, we applied higher temperature to accelerate the hydrolysis of $Na_2S_2O_3$ in order to attain a phase pure copper sulfide. *Qin et al.* (Qin, et al., 2005) have reported that copper nitrate was found to be the best candidate to demonstrate

the process of crystal growth and morphology evolutions among other copper sources. *Y. C. Zhang et al.* (Zhang, Qiao, et al., 2004) have demonstrated a similar route to produce copper sulfides using copper sulfate and sodium thiosulfate. Based on their work, the formation of *covellite,* CuS was described by the following steps:

$$Cu^{2+} + S_2O_3^{2-} + 2H_2O \rightarrow [Cu(S_2O_3)(H_2O)_2] \quad (1)$$

$$Cu^{2+} + 2S_2O_3^{2-} \rightarrow [Cu(S_2O_3)_2]^{2-} \quad (2)$$

$$[Cu(S_2O_3)(H_2O)_2] \rightarrow CuS\downarrow + SO_4^{2-} + 2H^+ + H_2O \quad (3)$$

$$[Cu(S_2O_3)_2]^{2-} + 6H_2O \rightarrow CuS\downarrow + SO_4^{2-} + 12H^+ \quad (4)$$

It was also mentioned in their work that $S_2O_3^{2-}$ would disproportionate to produce S^{2-} ions in aqueous solution under the hydrothermal condition at appropriate temperatures (e.g. 150 °C), which can readily combine with the Cu^{2+} ions to form CuS nanocrystallites.

$$Cu^{2+} + S^{2-} \rightarrow CuS\downarrow \qquad [pK_{sp}\,(CuS) = 35.2] \quad (5)$$

However, in our work, we believe that there are four possible pathways that can lead to the formation of CuS as summarized in **Figure 4.8**. Both of Cu(I) and Cu(II) will be taking part in the reaction. Since the initial copper source used was copper(II) nitrate, the transformation of Cu(II) to Cu(I) are expected to be the redox reactions between the hydrolysis of thiosulfate and its hydrolyzed species. The calculated redox potential with its respective redox reactions are displayed as below:

$$2Cu^{2+} + 2S_2O_3^{2-} \rightarrow 2Cu^+ + S_4O_6^{2-} \qquad [\Delta E^\theta = +0.24] \quad (6)$$

$$16Cu^{2+} + 8H_2S \rightarrow 16Cu^+ + S_8 + 16H^+ \qquad [\Delta E^\theta = +0.30] \quad (7)$$

Besides that, NO_2 generated from the nitrate salt will also contribute to the reduction of Cu(II) to Cu(I). The reaction and its calculated redox potential are displayed as the following:

$$Cu^{2+} + NO_2 + H_2O \rightarrow Cu^{+} + 2NO_3^{-} + 2H^{+} \quad [\Delta E^{\theta} = +0.96] \qquad (8)$$

The calculated redox potential show positive values for all reactions stated above. This strongly indicates that the reduction of Cu(II) to Cu(I) occurs in situ where both the Cu(II) and Cu(I) species are reacting with S species. Hence, the mechanism discussed below are related to both Cu species and led to the formation of final crystal system, CuS.

The main species in directing the pathways is $S_2O_3^{2-}$, which was deliberated from the main precursor ($Na_2S_2O_3$), followed by the $S_4O_6^{2-}$ and SO_4^{2-} and S^{2-} species. The $S_4O_6^{2-}$ species was mostly transformed from the main precursor, $Na_2S_2O_3$ during the reduction of Cu(II) to Cu(I) (Equation 6). Whilst, the SO_4^{2-} species was produced either by direct disproportionation of $S_2O_3^{2-}$ ion (Equation 9) or indirect disproportionation as proposed by *Y.C. Zhang et al.* (Zhang, Qiao, et al., 2004) (Equation 3, 4).

$$S_2O_3^{2-} + H_2O \rightarrow H_2S + SO_4^{2-} \qquad (9)$$

The generated SO_4^{2-} species will then react with Cu^{2+} ion to form copper sulfate ($CuSO_4$) and sodium-copper-sulfate [Krohnite, $Na_2Cu(SO_4)_2$] intermediate in which the crystal structures of both of these intermediates are shown in **Table 2** at 25°C and 35°C. Both the copper-thiosulfate and copper-sulfate complexes will then undergo transformation with the heat energy supplied to form the final CuS product.

Additionally, the formation of CuS can also be directed by the S^{2-} containing reagents (Routes 4.1, 4.2, and 4.3 in **Figure 4.8**). H_2S species is generated during the disproportionation of $S_2O_3^{2-}$ ion as shown in Equation 9. The H_2S species will then undergo

acid dissociation to form HS^- and S^{2-} species (Equation 11, 13) which can combine with Cu^{2+} ion to form CuS (Equation 10, 12, 14).

$$Cu^{2+} + H_2S \rightarrow CuS + 2H^+ \quad (10)$$

$$H_2S \leftrightarrow HS^- + H^+ \quad (11)$$

$$[Cu(H_2O)_5]^{2+} + HS^- \rightarrow [Cu(H_2O)_5(SH)]^+ \rightarrow CuS + 5H_2O + H^+ \quad (12)$$

$$HS^- \leftrightarrow S^{2-} + H^+ \quad (13)$$

$$Cu^{2+} + S^{2-} \rightarrow CuS \quad (14)$$

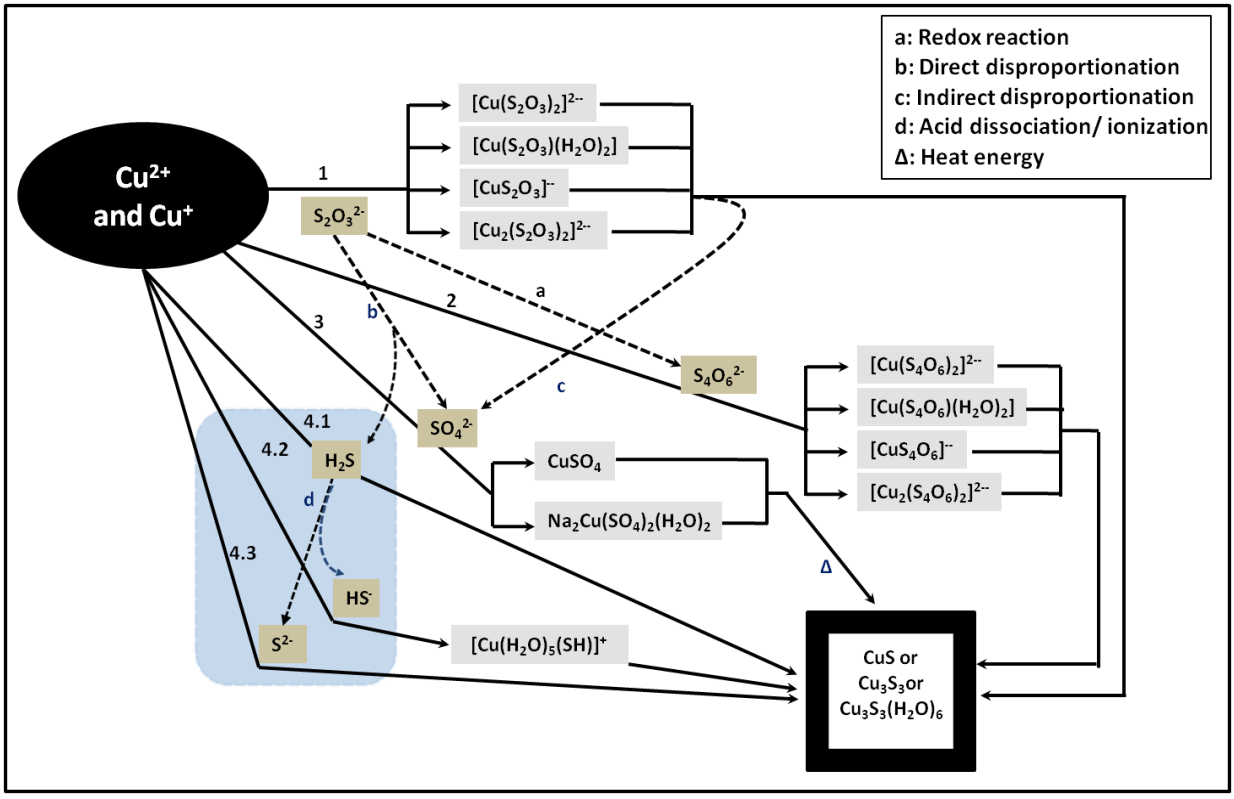

Figure 4.8: Overview of proposed mechanism in the formation of CuS.

4. 2 Effects of Cu: S Mole Ratio

The colour intensity of the reactant mixtures for hydrothermal reaction was recorded. It can be seen that the colour changes from milky green to milky yellow, followed by clear yellow solution, and cloudy white solution as depicted in **Figure 4.9** when the Cu: S (copper nitrate : sodium thiosulfate) mole ratio is increased. The pH of the reaction mixtures were also recorded (as tabulated in **Table 4.4**) before they were sealed in the Teflon tubes.

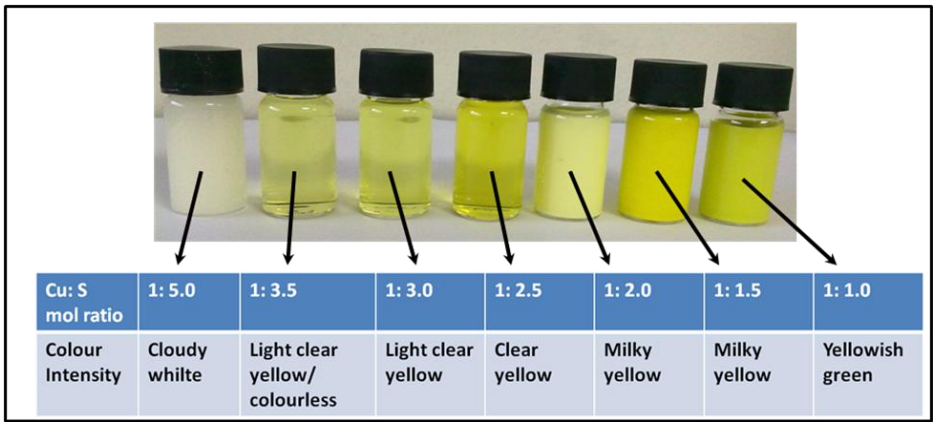

Figure 4.9: Colour intensity of the reactant mixtures at different Cu: S mole ratio.

Table 4.4: pH readings of the reaction mixtures at different Cu: S mole ratio.

Cu: S mol ratio	***1: 5.0***	***1: 3.5***	***1: 3.0***	***1: 2.5***	***1: 2.0***	***1: 1.5***	***1: 1.0***
pH (1st)	*5.979*	*8.359*	*8.060*	*8.095*	*6.611*	*3.994*	*3.786*
pH (2nd)	*6.024*	*8.246*	*8.025*	*8.118*	*6.800*	*3.965*	*3.765*
pH (3rd)	*6.064*	*8.062*	*8.035*	*8.073*	*6.864*	*3.952*	*3.757*
pH (ave)	***6.022***	***8.223***	***8.040***	***8.095***	***6.758***	***3.970***	***3.769***

4. 2. 1 Powder X-ray Diffraction

Figure 4.10 shows the PXRD patterns of the as-obtained products at 155.0 °C for 12 hours via hydrothermal treatment with various copper nitrate to sodium thiosulfate (abbreviated

as Cu: S) mol ratio. All observed diffraction peaks could be indexed to the phase formed accordingly. When Cu: S mol ratio was 1: 1, a pale greenish crystalline compound which can be indexed to natrochalcite, $NaCu_2(SO_4)(H_2O)$ with PDF 45-1364 (**Figure 4.10a**) formed during the reaction. For mol ratio of Cu: S = 1: 1.5, a black crystalline product was obtained with its characteristic peaks (**Figure 4.10b**) were fitted to rhombohedral *digenite*, Cu_9S_5 with PDF 047-1748 (a= 3.93Å, b= 48.14Å). Meanwhile, a black crystalline product was formed when the hydrothermal synthesis was subjected to mol ratio of Cu: S =1: 2. Its PXRD pattern as shown in **Figure 4.10(c)** indicated the formation of crystalline CuS which can be well indexed to hexagonal *covellite*, CuS (PDF 06-464, a= 3.792 Å, c= 16.34 Å). All the characteristic peaks in the hexagonal *covellite* diffraction pattern correspond to the phase pure CuS in the space group of *P63/ mmc*. For all of the powder mentioned above, no crystalline impurity peak can be detected in the pattern indicating the high purity of the products formed. When the sulfur ratio was increased to 2.5 (Cu: S = 1: 2.5), formation of a black crystalline compound which resulted in a phase mixture (CuS and S_8) is obtained (**Figure 4.10d**). All the characteristic peaks in its pattern are corresponded to hexagonal *covellite* (PDF 06-464, a= 3.792 Å, c= 16.34 Å) and face-centered orthorhombic sulfur, S_8 (PDF 89-2600, a= 10.437 Å, b= 12.845 Å, c= 24.369 Å, a/ b= 0.81253 Å, b/ c= 1.89716 Å). Similar trend is also observed for the powder synthesized at sulfur ratio of 3.0, 3.5 and 5.0 where their diffractograms are shown in **Figures 4.10e, f** and **g** respectively.

In order to investigate the relative percentage of CuS to S_8 in the phase mixture powders, *Rietveld* quantification analysis has been done and the fitting of the respective diffractograms are attached in *Appendix C*. The quantification results are shown in **Table 4.5** and the *Rietveld* refinement analysis of the samples produced under Cu: S mole ratio section. For Cu: S = 1: 2.0, 79 % CuS and 21 % S_8 are found in the synthesized powder.

For Cu: S = 1: 3.0, a decrease in CuS percentage with 64 % and an increase in S_8 with 36 % are shown. Similarly for S ratio of 3.5 and 5.0, the decrease in the CuS and increase in the S_8 content are also detected. In short, the trend observed is that as the ratio of S is raised from 2.5 to 5.0 during the synthesis, the S_8 content tends to be increased. Conversely, the CuS amount that obtained in the final synthesized powder has decreased. It can be clearly observed from the trend of the *Rietveld* quantification analysis (shown in **Figure 4.11** for simplicity purpose) that when the mol ratio of S was increased more than 2 (Cu: S= 1: 2), a phase mixture was obtained. In comparison to the relative percentage of CuS to S_8, the face-centered orthorhombic sulfur (S_8) is in appreciating percentage, while hexagonal *covellite* (CuS) shows a depreciating percentage content.

Table 4.5: Rietveld quantification analysis for products found with different Cu: S mole ratio[†].

Sample ID	Mole Ratio Cu: S	Rietveld Quantitative Analysis
H06	1: 1.0	100 % $NaCu_2(SO_4)(H_2O)$ (ICSD73265)
H07	1: 1.5	PDF047-1748: Cu_9S_5
H05	1: 2.0	100 % CuS (ICSD63327)
H08	1: 2.5	79 % CuS (ICSD63327) 21 % S_8 (ICSD412328)
H09	1: 3.0	64 % CuS (ICSD63327) 36 % S_8 (ICSD412328)
H10	1: 3.5	56 % CuS (ICSD63327) 44 % S_8 (ICSD412328)
H11	1: 5.0	45 % CuS (ICSD63327) 55 % S_8 (ICSD412328)

[†]*The syntheses were done with synthesis temperature fixed at 155 °C and synthesis time for 12 hours.*

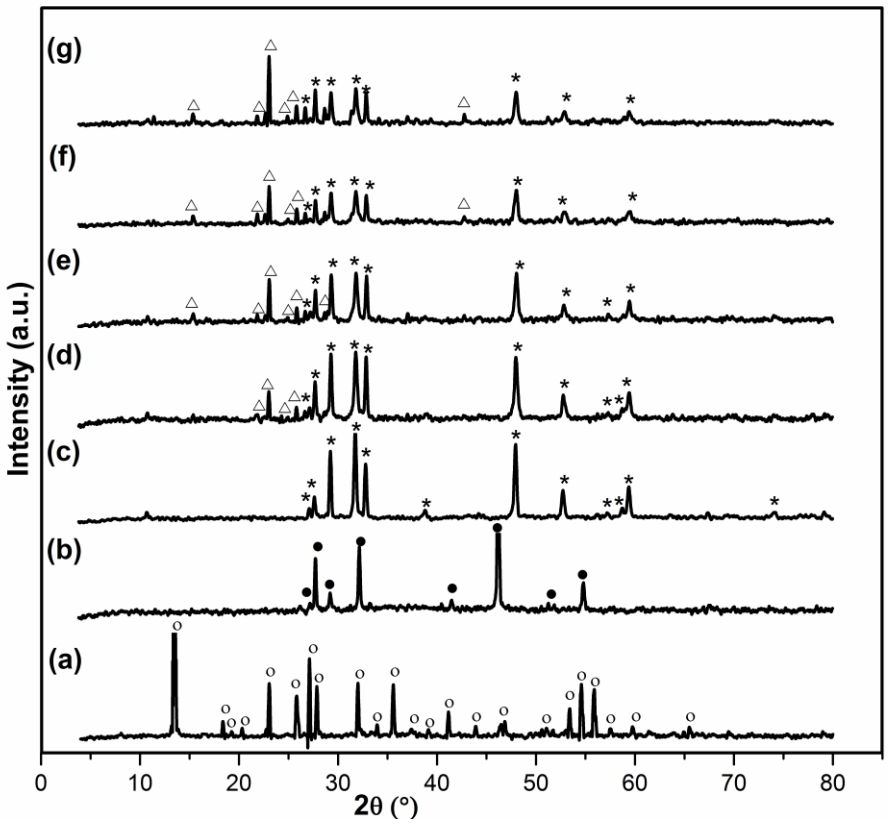

Figure 4.10: Powder XRD patterns of the products obtained with different Cu: S mole ratio: (a) 1: 1 (b) 1: 1.5 (c) 1: 2 (d) 1: 2.5 (e) 1: 3 (f) 1: 3.5 (g) 1: 5
* denotes the characteristic peaks of hexagonal *covellite* (CuS- PDF 06-0464);
Δ denotes the characteristic peaks of face-centered orthorhombic sulfur (S_8- PDF 86-2600);
• denotes the characteristic peaks of rhombohedral digenite (Cu_9S_5- PDF 047-1748);
o denotes the characteristic peaks of natrochalcite ($NaCu_2SO_4H_2O$-PDF 45-1364).

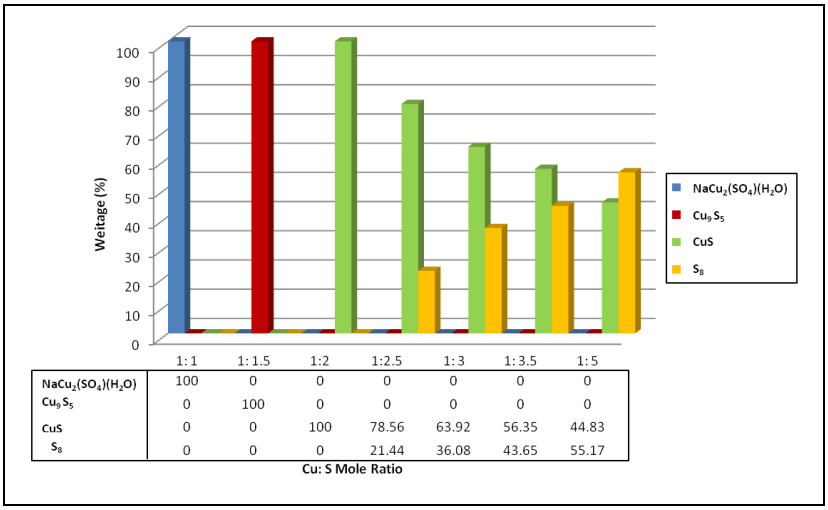

	1:1	1:1.5	1:2	1:2.5	1:3	1:3.5	1:5
$NaCu_2(SO_4)(H_2O)$	100	0	0	0	0	0	0
Cu_9S_5	0	100	0	0	0	0	0
CuS	0	0	100	78.56	63.92	56.35	44.83
S_8	0	0	0	21.44	36.08	43.65	55.17

Figure 4.11: Crystal compounds formed at different Cu: S mole ratio.

4. 2. 2 X-ray Fluorescence Spectroscopy and Energy Dispersive X-ray Spectrometry

XRF and EDX techniques were applied to probe the atomic composition of the elements present in the products. The EDX spectra for each sample in this section are attached in *Appendix D*. The chemical analysis of the samples prepared at different Cu: S synthesis mole ratio is tabulated in **Table 4.6** and **Table 4.7**. The representative of the graphical forms is shown in **Figure 4.12** and **Figure 4.13** respectively. From **Figure 4.12**, it can be observed that the sulfur composition increased when the synthesis sulfur ratio was increased from 1 to 5. This indicates that as the synthesis Cu: S mole ratio increases, higher sulfur content can be found in the bulk of the sample formed. On the other hand, from the EDX analysis shown in **Figure 4.13**, the surface sulfur content is comparatively lower than copper when the synthesis mole ratio of Cu: S is varied from 1: 1 to 1: 1.5 initially. As we increase the Cu: S synthesis mole ratio further from 1: 2 to 1: 5, the sulfur contents on the surface increases and it is significantly higher than the copper content on the surface. In comparison among the PXRD, EDX, and XRF analyses, the higher bulk sulfur content suggests that the crystalline S_8 is mainly located in the bulk of the material rather than on the surface. A very important point to be highlighted here, for the phase pure copper sulfides, (i.e., *digenite* synthesized at synthesis mole ratio of Cu: S = 1: 1.5 and *covellite* prepared at synthesis mole ratio of Cu: S = 1: 2) it is found that the calculated mole ratio from XRF and EDX analyses of *digenite* (Cu_9S_5) give 1: 0.64 and 1: 0.56 respectively. Whilst for *covellite* (CuS), XRF and EDX analyses show calculated mole ratio of 1: 1.04 and 1: 1.07 respectively. These results agree very well with the stoichiometric formulae of the 2 crystal structures (*digenite* and *covellite*) which are determined by PXRD analysis previously.

Table 4.6: XRF analysis of samples formed at different Cu: S mole ratio.

Sample ID	Synthesis Mole Ratio(Cu:S)	Element	Conc. (wt %)	No. of mole†	Calculated Atomic ratio (Cu / S)†	Cu: S†
H06	1: 1.0	Cu S	77.41 22.59	1.22×10^{-2} 7.05×10^{-3}	1.73	1: 0.58
H07	1: 1.5	Cu S	75.50 24.50	1.19×10^{-2} 7.64×10^{-3}	1.55	1: 0.64
H05	1: 2.0	Cu S	65.20 34.80	1.03×10^{-2} 1.09×10^{-2}	0.95	1: 1.04
H08	1: 2.5	Cu S	50.60 49.40	7.96×10^{-3} 1.54×10^{-2}	0.52	1: 1.19
H09	1: 3.0	Cu S	43.30 56.70	6.81×10^{-3} 1.77×10^{-2}	0.39	1: 2.60
H10	1: 3.5	Cu S	35.00 65.00	5.51×10^{-3} 2.02×10^{-2}	0.27	1: 3.68
H11	1: 5.0	Cu S	28.08 71.92	4.42×10^{-3} 2.24×10^{-2}	0.20	1: 5.08

†*For example of calculation, please refer Appendix B.*

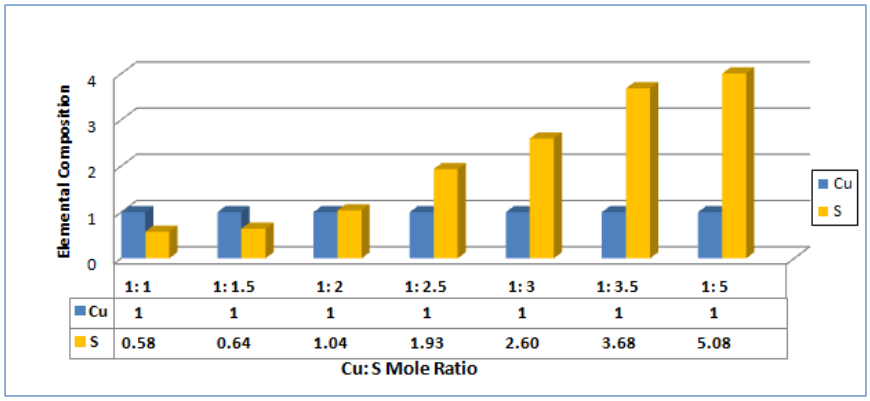

Figure 4.12: XRF analysis of products formed at different Cu: S mole ratio.

Table 4.7: EDX analysis of samples formed at different Cu: S mole ratio.

Sample ID	Synthesis Mole Ratio (Cu:S)	Element	Conc. (at%-A)	Conc. (at%-B)	Conc. (at%-average)†	Calculated Atomic ratio (Cu / S)†	Cu: S†
H06	1: 1.0	Cu S	16.30 9.80	24.70 10.60	20.50 10.20	0.32	1: 0.50
H07	1: 1.5	Cu S	63.20 36.80	65.30 34.70	64.30 35.70	1.80	1: 0.56
H05	1: 2.0	Cu S	48.50 51.50	48.10 51.90	48.30 51.70	0.93	1: 1.07
H08	1: 2.5	Cu S	51.54 48.46	49.30 50.70	50.42 49.58	1.02	1: 0.98
H09	1: 3.0	Cu S	49.16 50.84	46.09 53.91	47.63 52.38	0.91	1: 1.10
H10	1: 3.5	Cu S	47.56 52.44	44.19 55.81	45.88 54.13	0.85	1: 1.18
H11	1: 5.0	Cu S	48.71 51.29	56.74 43.26	52.73 47.28	1.12	1: 0.90

†*For example of calculation, please refer Appendix B.*

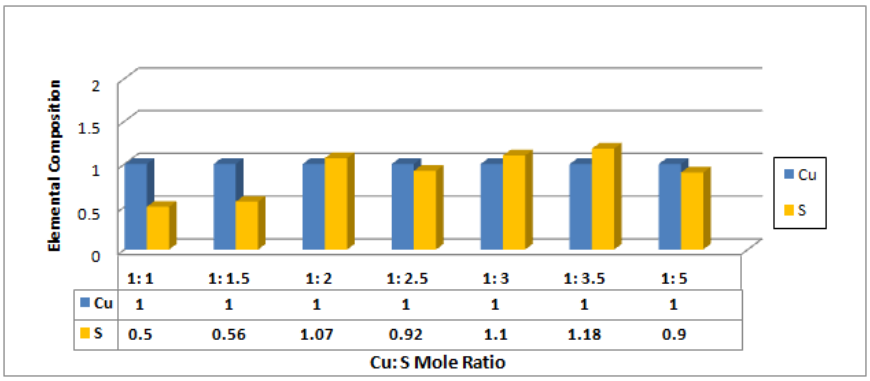

Figure 4.13: EDX analysis of products formed at different Cu: S mole ratio.

4. 2. 3 Field Emission Scanning Electron Microscopy

Figures 4.14, 4.15, & **4.16** illustrate the change in morphology of the products at three different FESEM magnifications. Overall, all the powders generated from different Cu: S mole ratio show highly agglomerated structures with different morphology. **Figure 4.14(a)**

depicts the morphology of the powder which was formed with Cu: S mole ratio of 1: 1. The powder shows irregular plate-like structure with width of *ca.* 50-100 nm, length in the range of micron size, and thickness of *ca.* 20-100 nm. When Cu: S mole ratio was increased to 1: 1.5, the particles are aggregated closed to one another, yet the shape of each particle could still be distinguishable (**Figure 4.14b**). A close up view (**Figures 4.15b and 4.16b**) indicates that the plate-like structure was not found but the particles display an irregular circular shape with diameter of ca. 20-50 nm, and thickness of *ca.* 5- 10 nm. The average size of the particle found with Cu: S mole ratio of 1: 1.5 is significantly smaller than the particle found with 1: 1. For Cu: S mole ratio of 1: 2 was applied to the system, we cannot observe any of the circular or plate-like structure in the product as depicted in **Figure 4.14c**. Higher magnified images in **Figures 4.15c** and **4.16c** indicate that the highly agglomerated particles were essentially built up by several irregular hexagonal shape nanoplates which assembled, and interlaced perpendicular among each other. The hexagonal nanoplates have a mean edge length of *ca.* 1-1.5 μm and an average thickness of *ca.* 50-100 nm. The single hexagonal morphology found in this powder corresponds well with the single hexagonal phase of *covellite* determined by PXRD. In the micrographs as shown in **Figure 4.16c**, it can be seen that some of the hexagonal shape particles exhibit eroded piece of hexagonal structure. Similar hexagonal shape can be observed for the powder synthesized at mole ratio of Cu: S =1: 2.5 and 1: 3 as shown in **Figure 4.15d** and **4.15e** respectively. The particle in Figure 4.15d exhibits larger diameter in comparison to the particle found in **Figure 4.15c** and **e**. However, when the mole ratio of Cu: S was further increased to 1: 3.5, two different structures can be distinguished from the micrograph as shown in **Figure 4.14**. Clusters of thicker hexagonal shaped particles appear to cover large, amorphous solid masses. Similar morphology was observed for the product

prepared at mole ratio of Cu: S of 1: 5 (**Figure 4.14g**), thus indicating that this morphology results from phase mixtures rich in S_8. These thick hexagonal microplates tend to fuse among each other, building big agglomerates.

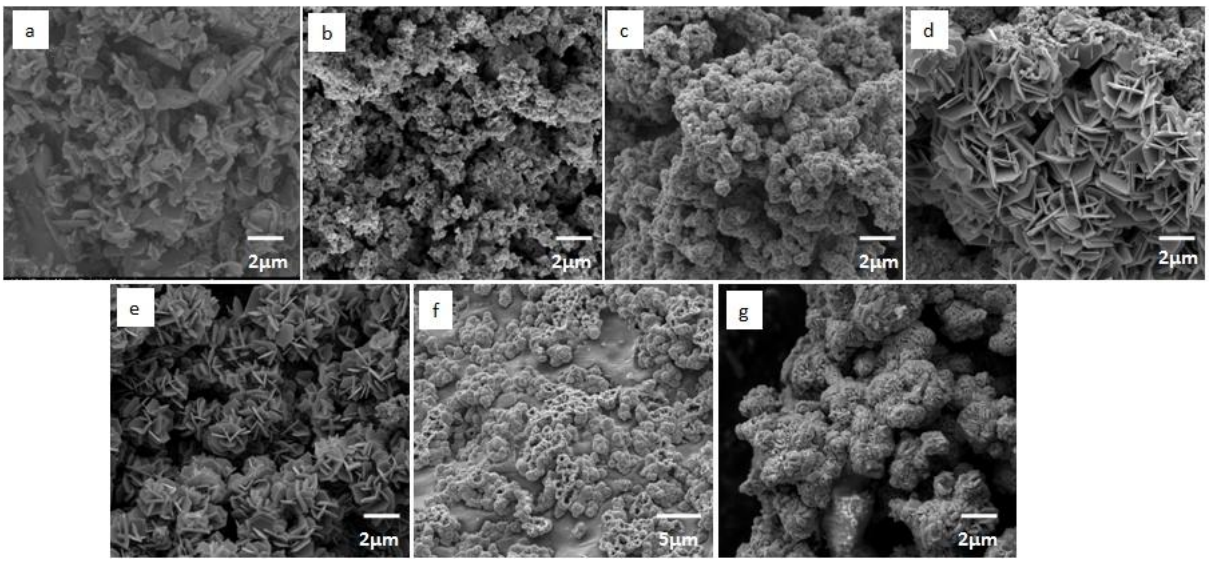

Figure 4.14: FESEM micrographs (15 000 × magnification) of products obtained with Cu: S mole ratio of (a) 1: 1.0 (b) 1: 1.5 (c) 1: 2.0 (d) 1: 2.5 (e) 1: 3.0 (f) 1: 3.5 (g) 1: 5.0

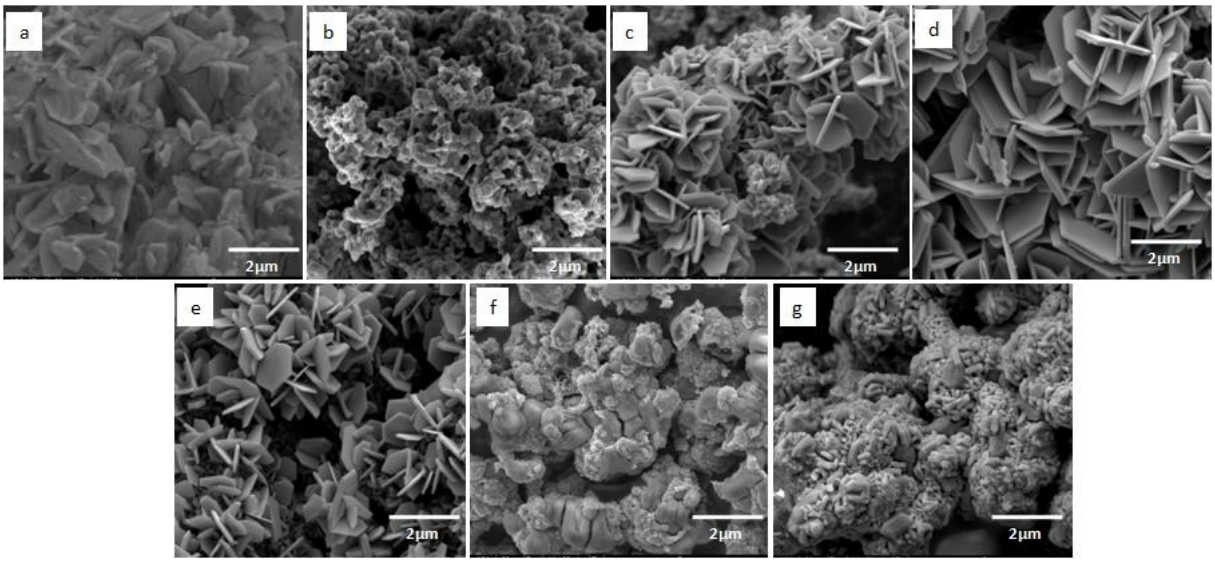

Figure 4.15: FESEM micrographs (30 000 × magnification) of products obtained with Cu: S mole ratio of (a) 1: 1.0 (b) 1: 1.5 (c) 1: 2.0 (d) 1: 2.5 (e) 1: 3.0 (f) 1: 3.5 (g) 1: 5.0

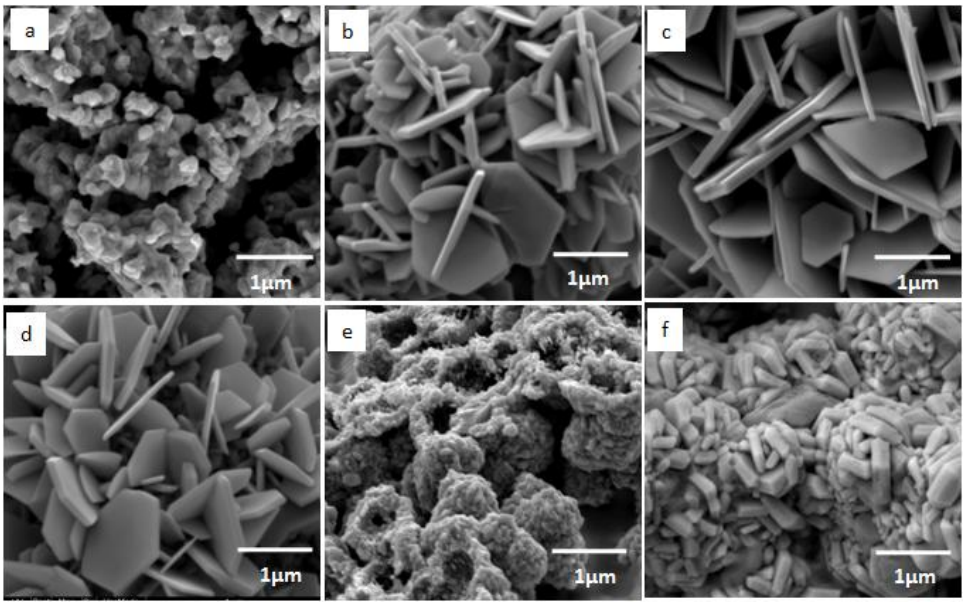

Figure 4.16: FESEM micrographs (60 000 × magnification) of products obtained with Cu: S mole ratio of (a) 1: 1.5 (b) 1: 2.0 (c) 1: 2.5 (d) 1: 3.0 (e) 1: 3.5 (f) 1: 5.0

4. 2. 4 Discussion

It can be seen that the color of reactant mixtures changed from milky green to milky yellow, clear yellow and finally to cloudy white solution when the Cu: S mol ratio have been raised from 1: 1 to 1: 5. Such color change can be related to the conversion of different complexes formed. This can be speculated when the system is in Cu: S of 1: 1 mol ratio, all $S_2O_3^{2-}$ ions are exhausted in the reaction. This leads to the formation of sulfur-deficient compound-natrochalcite which was confirmed from the PXRD analysis. When Cu: S mol ratio was increased to 1: 1.5, the supplied $S_2O_3^{2-}$ ions are just sufficient to form a sulfur-deficient copper sulfide compound (Cu_9S_5). On raising Cu: S mol ratio to 1: 2, the existing Cu^{2+} ions are adequate to form a stoichiometric balanced copper sulfide compound (*covellite*) with the hydrolyzed $S_2O_3^{2-}$ ions. When the system was further increased from 1:2.5 to 1: 5 Cu: S mol ratio, it was found that cyclooctasulfur was present in addition of covellite from the PXRD patterns, indicating that the $S_2O_3^{2-}$ ion might present in excess in the system.

From the PXRD analysis, it can be noted that three phase pure crystalline products were identified, *i.e. natrochalcite*, *digenite*, and *covellite* at Cu: S mole ratio of 1: 1, 1: 1.5, and 1: 2 respectively. While, the products in the range of Cu: S mole ratio from 1: 2.5 to 1: 5 consist of mixed phase of *covellite* and cyclooctasulfur. This signifies that the formation of pure phase product is most favorable at Cu: S mole ratio of 1: 1, 1: 1.5, and 1: 2 by employing copper(II) nitrate and sodium thiosulfate as the reactants. The XRF and EDX results also confirmed that both of the products (*digenite* and *covellite*) prepared at Cu: S mole of 1: 1.5 and 1: 2 respectively are in good agreement with the PXRD results. In the meantime, the XRF results show a steady increase of sulfur atomic ratio for the products prepared from Cu: S mol ratio of 1: 1 to 1: 5. This is evidenced by the PXRD quantification analysis where cyclooctasulfur increases for Cu: S mole ratio in the range of 1: 2.5 to 1: 5. Yet, the EDX analysis shows that the copper and sulfur atomic ratio is almost 1: 1 for the products synthesized at Cu: S mol ratio of 1: 2.5 to 1: 5. This suggests that the content of sulfur is more pronounced in the bulk rather than on the surface. From the perspective of morphology, it can be spotted that single morphology (plate-, circular-, and hexagonal-like structures) were found for products synthesized at Cu: S mole ratio of 1: 1, 1: 1.5, and 1: 2 respectively. This correlates well with the single phase (*natrochalcite, digenite,* and *covellite*) observed from PXRD. Products formed at Cu: S mol ratio of 1: 2.5 and 1: 3 also shows single morphology (hexagonal nanoplate) from FESEM, which is contrary to the mixed phase of covellite and cyclooctasulfur found from PXRD. The disappearance of the second morphology in the products at 1: 2.5 and 1: 3 Cu: S mole ratio might due to the minute amount of cyclooctasulfur grow in the products. Meanwhile, two different morphologies (clusters of micron-range hexagonal shaped particles on the solid masses)

were observed for products formed at 1: 3.5 and 1: 5 Cu: S mole ratio. This FESEM result matches well with the PXRD result where mixed phase of CuS and S_8 were found.

Previous works have investigated the effect of the variation of the ratio of copper to sulfur precursors, and also found that this parameter plays an important role in determining the product phase composition (An, et al., 2008; Ghezelbash & Korgel, 2005; Li, et al., 2009; Wan, et al., 2004; Zhang, Hu, et al., 2004). *Fei Li et al.* have confirmed that phase pure covellite was observed at the molar ratio of (copper nitrate: sulfur powder) Cu: S = 1: 2 and 1: 3 in ethylene glycol during the reaction. A mixed phase of Cu_2S and $Cu_{1.96}S$ was found with molar ratio of Cu: S = 2: 1; while mixed phase of CuS and $Cu_{7.2}S_4$ was observed with molar ratio of Cu: S = 1: 1 (Li, et al., 2009). *C. An et al.* have shown that the effect of precursor mole ratio might lead to the formation of a phase pure or a mixed phase product. In their experiments, copper acetate and sodium thiosulfate in a solution of ethylene glycol and mixed surfactants of sodium oleate and hexadecylamine were selected as the precursors in the hydrothermal reaction where a phase pure hexagonal CuS nanocrystals can only be obtained with copper acetate to sodium thiosulfate mole ratio of 1: 6. They showed that when Cu: S mole ratio was changed to 1: 1; 1: 4; 2: 1; and 3: 1, a phase mixture of $Cu_{1.65}S$ with minor amount of CuS; Cu_2S with minor amount of CuS; Cu_2S and $Cu_{1.97}S$; and dominant metallic Cu with $Cu_{31}S_{16}$ were formed respectively (An, et al., 2008). In the studies conducted by *Ghezelbash and Korgel*, copper acetylacetonate and sulfur powder were added to o-dichlorobenzene, oleyamine, and ocetonic acid during the preparation. These investigators obtained a mixture of CuS and $Cu_{1.8}S$ with Cu: S (copper acetylacetonate: sulfur powder) mole ratio of 1: 1; while single phase of CuS and $Cu_{1.8}S$ were formed with Cu: S mole ratio of 1: 2 and 2: 1 respectively (Ghezelbash & Korgel, 2005). *S. Wan and coworkers* have revealed that a phase pure covellite can only be found

by reacting CuCl with S powder in ethylene glycol at 1: 1 ratio (Wan, et al., 2004). Synthesis with Cu: S mol ratio of 1: 2 as well as 2: 1 mol ratio yielded mixed phases of unknown compound. A group of researchers have demonstrated that a phase pure hexagonal *covellite* can be formed by reacting equimolar amounts of copper sulfate and sodium thiosulfate in water via hydrothermal reaction (Zhang, Hu, et al., 2004). In our work, we are able to produce pure phases of *covellite* and *digenite* by adjusting the mole ratio of copper nitrate to sodium thiosulfate at 1: 2 and 1: 1.5 respectively via hydrothermal route without the use of any assisting agent. Therefore, it can be deduced that mole ratio of Cu: S precursor plays a very vital role in determining the crystal structures, phase purity and the morphology of the crystal compound formed.

4. 3 Effects of Synthesis Time

4. 3. 1 X-ray Diffraction

An investigation was carried out with different synthesis times (1, 3, 6, 8, and 12 hours) to determine the minimum time required to achieve phase pure *covellite* formation under Cu: S mole ratio of 1: 2 at 155.0 °C. The PXRD profiles (as shown in **Figure 4.17**) of products recovered at different synthesis times indicate that phase mixtures of *covellite* and cyclooctasulfur were found for the powder synthesized at 1 hour synthesis time (**Figure 4.17a**). On the contrary, only phase pure *covellite* was detected for the products prepared at 3, 6, 8, and 12 hours. In addition, it can be observed that at longer synthesis times, the reflections become sharper, indicating that more crystalline material is obtained. Therefore, it can be deduced that the crystallite size is growing with longer synthesis time.

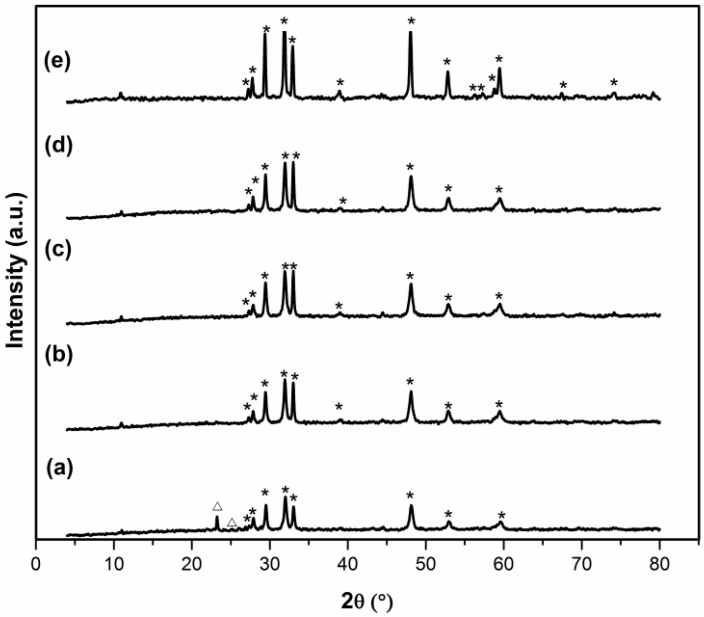

Figure 4.17: Powder XRD patterns of the products obtained with different synthesis time[†]:
(a) 1hour (b) 3 hours (c) 6 hours (d) 8 hours (e) 12 hours
* denotes the characteristic peaks of hexagonal *covellite* (CuS- PDF06-0464);
# denotes the characteristic peaks of face-centered orthorhombic sulfur (S_8- PDF86-2600).
[†]*The syntheses were done with synthesis temperature fixed at 155 °C and synthesis time for 12 hours.*

Hence, detailed analysis on the estimation of crystallite size of the products formed at different synthesis times was done. The crystallite size analysis is also known as peak profile analysis which is determined by Scherrer equation (Scherrer, 1918):

$$\beta(2\theta) = \frac{K\lambda}{L\cos\theta}$$

where β is FWHM in radians, K is the Scherrer constant (normally 0.94 for FWHM of spherical crystals with cubic symmetry), λ is the X-ray wavelength (0.15406 nm for CuK_{α}), L is the crystallite size, and θ is the Bragg angle corresponding to the maximum of the diffraction peak. The error analysis was also estimated to improve the accuracy of the reported readings. The approximation of the error analysis was done as below:

$$dL = \frac{K\lambda}{\beta}\left(\frac{\tan\theta}{\cos\theta}\right)d\theta$$

From the calculation, the products synthesized at 3, 6, 8, and 12 hours have crystallite size of (31.49 ± 1.44), (31.38 ± 1.44), (34.80 ± 1.59), and (44.94 ± 2.05) nm respectively as tabulated in **Table 4.8**. The corresponding peak fitting plots for each of these samples can be referred in *Appendix E*. From **Figure 4.18**, it is apparent that the crystallite size increases with longer synthesis time. This is consistent with the earlier deduction where crystal growth process is in favor when the synthesis time is prolonged.

Table 4.8: Data distribution of peak profile analysis.

Sample ID	Synthesis time (hours)	FWHM (°)	FWHM (rad)†	Angle (2θ)	Angle (θ)†	Cos θ	Crystallite size (nm)†	dL†
H13	3	0.274	0.00478	31.935	15.9675	0.9614	31.49	1.44
H14	6	0.275	0.00480	31.952	15.9760	0.9614	31.38	1.44
H15	8	0.248	0.00433	31.955	15.9775	0.9614	34.80	1.59
H05	12	0.192	0.00335	31.876	15.9380	0.9616	44.94	2.05

†*For further details of the calculations involved, please refer Appendix E.*

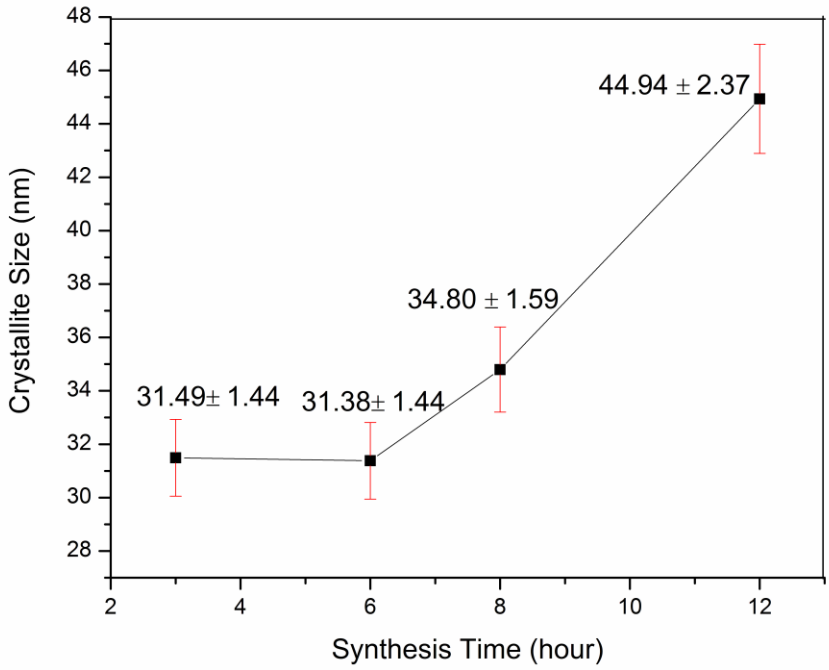

Figure 4.18: Crystallite size estimation for products synthesized at 3, 6, 8 and 12 hours.

4. 3. 2 X-ray Fluorescence Spectroscopy and Energy Dispersive X-ray Spectrometry

Table 4.9 and **Table 4.10** tabulate the XRF and EDX analyses done on the samples produced by varying the synthesis time parameter. The EDX spectra for each sample in this section are attached in *Appendix F*. **Figure 4.19** and **Figure 4.20** are redrawn from **Table 4.8** and **Table 4.9** for better illustration. From the XRF analysis, all the samples produced at all synthesis time show almost Cu: S mole ratio of 1: 1 except for the samples produced at 1 hour and 3 hours. The product at 1 hour synthesis time (H12) exhibits higher sulfur content (Cu: S mole ratio = 1: 1.87) which is in good agreement with PXRD analysis where there is extra S_8 (cyclooctasulfur) appear in the bulk of the sample. Furthermore, EDX analysis indicates that the product at 1 hour synthesis time has higher sulfur content on the surface with Cu: S mole ratio to be calculated as 1: 2.70. From the EDX analysis, all the samples produced demonstrate almost 1: 1 Cu: S mole ratio excluding the products formed

at 1 hour and 3 hours. Although the previous PXRD pattern indicates that the product at 3 hours synthesis time matches the phase of hexagonal *covellite*, both of the XRF and EDX analysis of this sample do not give the Cu: S mole ratio of 1: 1. The calculated Cu: S mole ratio of this sample (H13) is 1: 1.20 and 1: 0.73 from XRF and EDX analysis respectively. This unusual observation might be due to the trace presence of unreacted cyclooctasulfur in the product which is insignificant and below of sensitivity level to be detected in PXRD analysis. The EDX analysis also provides information that the total distribution of Cu and S elements of this sample (H13) is not even as there is more Cu relative to S at the surface.

Table 4.9: XRF analysis of samples formed at different synthesis times.

Sample ID	Time (hrs)	Element	Conc. (wt%)	No. of mole[†]	Calculated Atomic ratio (Cu / S)[†]	Cu: S[†]
H12	1	Cu S	51.46 48.54	8.10×10^{-3} 1.51×10^{-2}	0.54	1: 1.87
H13	3	Cu S	62.30 37.70	9.80×10^{-3} 1.18×10^{-2}	0.83	1: 1.20
H14	6	Cu S	63.30 36.10	9.96×10^{-3} 1.13×10^{-2}	0.88	1: 1.13
H15	8	Cu S	63.90 36.10	1.01×10^{-2} 1.13×10^{-2}	0.89	1: 1.12
H05	12	Cu S	65.20 34.80	1.03×10^{-2} 1.09×10^{-2}	0.95	1: 1.04

[†]*For example of calculation, please refer Appendix B.*

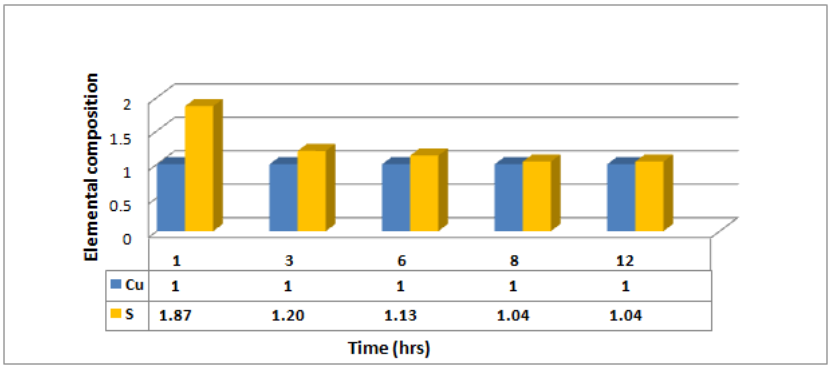

Figure 4.19: XRF analysis of products formed at different synthesis times.

Table 4.10: EDX analysis of samples formed at different synthesis times.

Sample ID	Time	Element	Conc. (±2.0 at%-A)	Conc. (±2.0 at%-B)	Conc. (±2.0 at%-ave.)†	Calculated Atomic ratio (Cu / S)†	Cu: S†
H12	1	Cu S	8.90 91.10	45.20 54.80	27.05 72.95	0.37	1: 2.70
H13	3	Cu S	64.95 35.05	50.96 49.04	57.96 42.05	1.38	1: 0.73
H14	6	Cu S	50.92 49.08	51.68 48.32	51.30 48.70	1.05	1 : 0.95
H15	8	Cu S	50.43 49.57	52.64 47.36	51.53 48.47	1.06	1: 0.94
H05	12	Cu S	48.47 51.53	48.06 51.94	48.27 51.73	0.93	1: 1.07

†*For example of calculation, please refer Appendix B.*

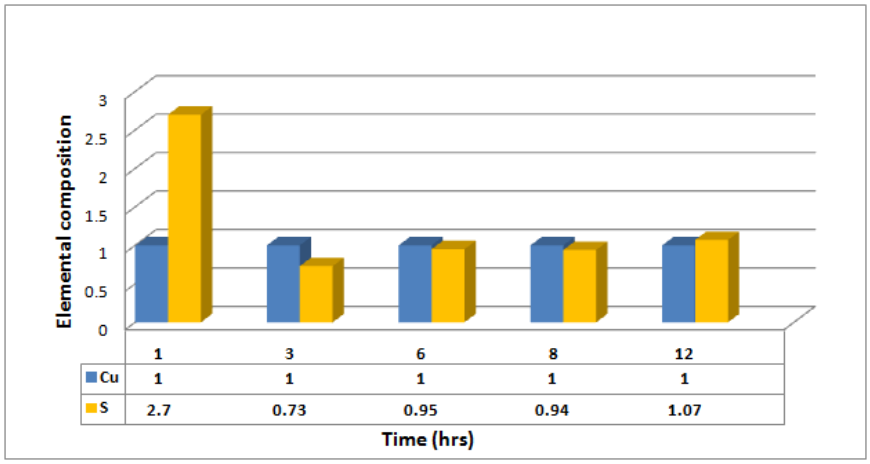

Figure 4.20: EDX analysis of products formed at different synthesis times.

4. 3. 3 Field Emission Scanning Electron Microscopy

The morphology of the products formed at different synthesis times is described correspondingly at three magnifications (15 000, 30 000, and 60 000 ×) in **Figures 4.21, 4.22,** and **4.23**. In general, the products formed at different synthesis times exhibit highly agglomerated structure, and the particles are not orderly arranged. It can be viewed that all the samples show almost similar morphology- a hexagonal nanoplate as a base structure.

As the synthesis time increases, it can be observed that the size of the particle increases in relative. For products formed at 3, 6, 8, and 12 hours synthesis time, apparent hexagonal nanoplate morphology can be observed (**Figure 4.22 b-e**). These hexagonal nanoplates are found to interlace perpendicular among each other. However, the size of these nanoplates is non-uniform, which ranges from 100 nm to 1 μm, whilst, the thickness of these nanoplates is *ca.* 10 nm. At 1 hour synthesis time, it is clearly seen that jagged hexagonal clusters with average diameter of *ca.* 100 nm, and thickness of *ca.* few tens nanometers. Some of these jagged hexagonal clusters exhibit large pores as depicted in **Figure 4.23**.On the other hand, the presence of cyclooctasulfur in the 1 hour reaction product is also evidenced by FESEM image (**Figure 4.24**). A second morphology was found in addition to the jagged hexagonal shaped *covellite*, suggesting that there were two distinguishable crystal phases in this powder. The jagged hexagonal nanoplates were found to stick on the 'egg-shaped' structure particle. This second morphology- 'egg-shaped' particle can be deduced as the cyclooctasulfur which is evidenced from the PXRD analysis discussed previously.

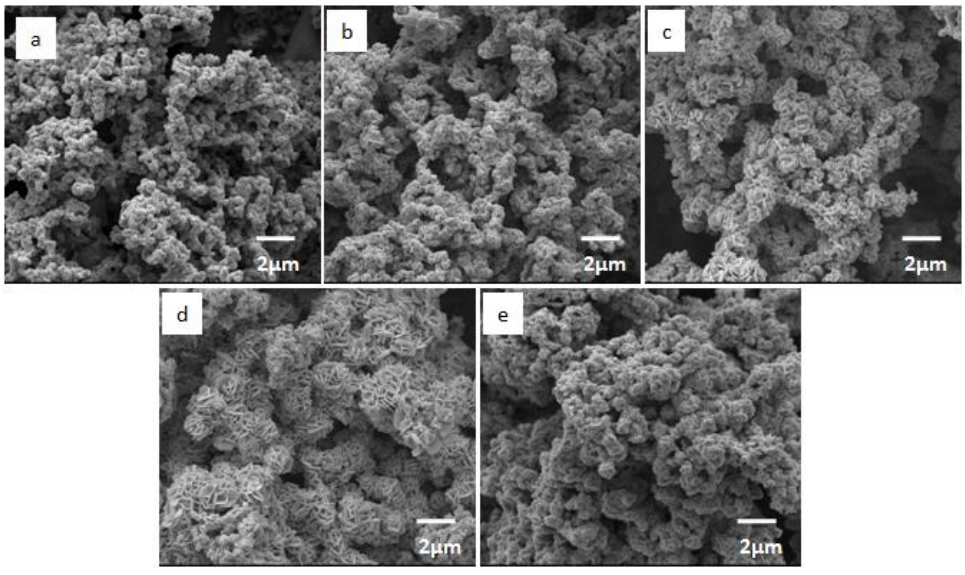

Figure 4.21: FESEM micrographs (15 000 × magnification) of products obtained at synthesis times of (a) 1 hour (b) 3 hours (c) 6 hours (d) 8 hours (e) 12 hours

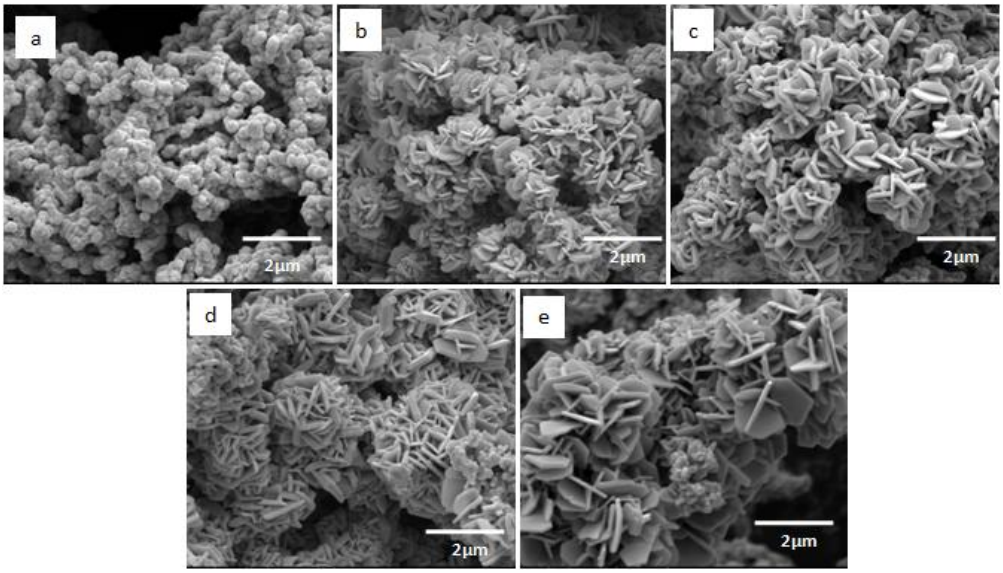

Figure 4.22: FESEM micrographs (30 000 × magnification) of products obtained at synthesis times of (a) 1 hour (b) 3 hours (c) 6 hours (d) 8 hours (e) 12 hours.

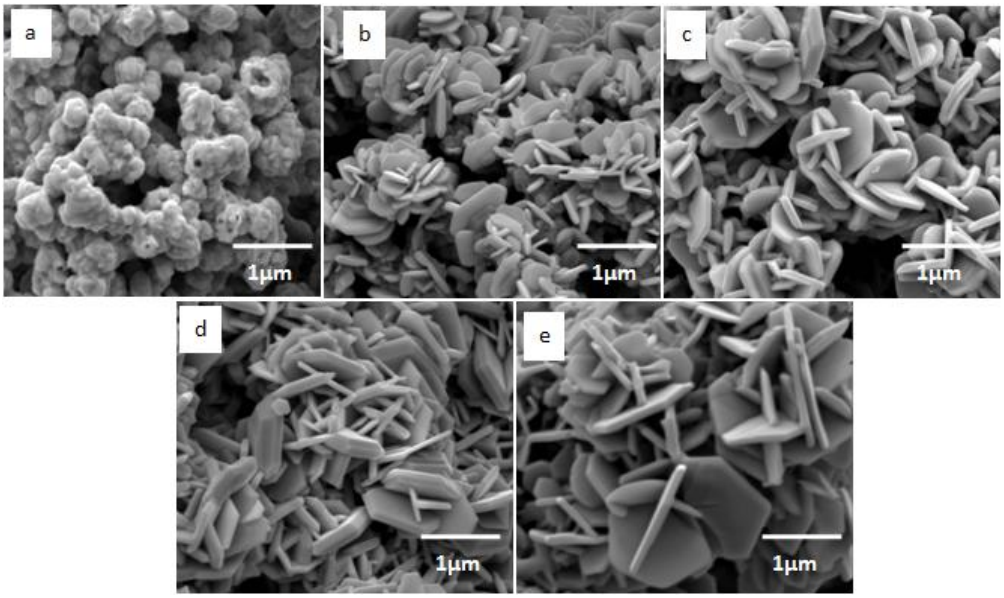

Figure 4.23: FESEM micrographs (60 000 × magnification) of products obtained at synthesis times of (a) 1 hour (b) 3 hours (c) 6 hours (d) 8 hours (e) 12 hours

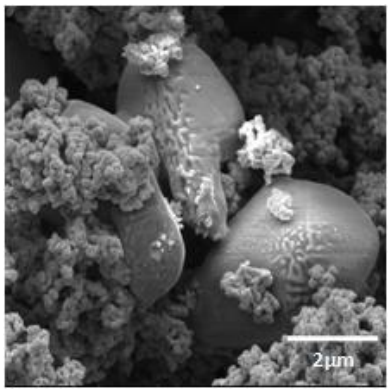

Figure 4.24: FESEM image of product formed at 1 hour.

4. 3. 4 Discussion

Generally, synthesis time plays a crucial role in dictating the yield, crystallinity, crystal size, phase purity, and morphology of the end products synthesized (Qin, et al., 2005; Tang, et al., 2004; Tezuka, et al., 2007; Zhang, Qiao, et al., 2004). These facts hold true for most of the hydrothermal processes. For instance, previous investigation conducted by *Qin et al.* revealed that crystallinity was improved and the crystal size of CuS grew larger with prolonging the synthesis time. They have also demonstrated that phase pure compound can be achieved when the synthesis time was prolonged (Qin, et al., 2005). Meanwhile, *Y. C. Zhang et al.* have shown that longer synthesis time can enhance the crystallinity and yields of the obtained CuS with reference to the amount of CuO used (Zhang, Qiao, et al., 2004). On the other hand, experiments conducted by *K. Tang et al.* indicated that synthesis time is a parameter influencing the phase purity and morphology of the final product formed. They found that longer synthesis time favors the purity as well as the crystallinity of the final product. Besides that, they have also observed that the percentage of trepang-like structures and the aggregation of the flake-like CuS were increased when the synthesis time was prolonged (Tang, et al., 2004). Another study done by *K. Tezuka et al.* using elemental

copper and sulfur as precursors verified that longer synthesis times are required to produce a phase pure CuS in order for a complete reaction to take place (Tezuka, et al., 2007).

In the present study, we manage to show that synthesis time has effect on the phase purity, crystallinity, and the crystallite size of the end product prepared. From the PXRD, as well as other complementary results from XRF, EDX and SEM, extra cyclooctasulfur present in addition of *covellite* at 1 hour synthesis time signifies that the reaction is incomplete. The presence of visible cyclooctasulfur in the product suggests that it is a possible transient phase from the coordination precursor which might due to the decomposition of $S_2O_3^{2-}$ ion into cyclooctasulfur. After that, the formation of phase pure CuS is accompanied by the disappearance of the intermediate (cyclooctasulfur) at 3 hour synthesis time reveals that the synthesis time must be no less than 3 hours in order to obtain phase pure CuS. Longer synthesis time favors the formation of phase pure compounds as it can aid in the complete transformation of the coordination precursors into CuS. On the other hand, it can be observed that the PXRD peaks of the products become sharper and narrower when the synthesis time is increased. This implies that the crystallinity and the crystal size of the products formed are enhanced as the synthesis time is extended. Further crystallite size estimation applying *Scherrer* Equation confirms that the crystallite size is growing with longer synthesis time. Prolonging the synthesis time can result in the further growth of the crystallite into a larger crystal which accounts for the reason why longer synthesis time favor larger crystallite size of the products. In comparison of the products formed from different synthesis time, the smaller crystallite formed from shorter synthesis time is expected to give a higher surface area. However, there are some drawbacks with the products prepared at shorter synthesis time. This includes the amount of yield produced as well as the separation issue. For products synthesized with shorter synthesis time, the

amount of yield obtained was very little and it is not cost effective to conduct the mercury sorption experiment. In addition, the separation of the final product from the filtrate was not as easy as compared to the product prepared with longer synthesis time. As a result, the sample prepared at 12 hours synthesis time was selected to perform mercury sorption experiment. Hence, different synthesis time influences the phase purity, crystallinity, and crystal size of the end products.

4. 4 Further Studies on Phase Pure Copper Sulfides (Cu_xS_y)

4. 4. 1 Properties of Phase Pure Copper Sulfides

(a) Elemental Mapping and Atomic Composition

It is vital to characterize the microstructural composition and elemental distribution in the materials prepared in order to further understand the properties and the relative spatial arrangement in these materials. Therefore, this important information is probed via EDX analysis. The FESEM micrograph and its corresponding elemental (Cu and S) map of *covellite* sample are displayed in **Figure 4.25**. The distribution of Cu is denoted with blue while S is represented by green dots. It can be noticed that the distribution of Cu and S are homogeneous on the surface of *covellite* sample. The deposition of Cu is evenly surrounded by S on the *covellite* sample. A detailed atomic composition of Cu and S was quantitatively determined by EDX analysis where various spots and areas of *covellite* sample were taken. The FESEM images and the graphs of the relative atomic composition of *covellite* are presented in **Figures 4.26** and **4.27**. The results indicate that the atomic composition of Cu and S collected at different spots and areas are quite closed to each other, reaching percentages of almost 50: 50. This reveals that the localized distribution of Cu and S is

consistent with the elemental map discussed earlier. In the meantime, it agrees well with the nominal stoichiometric of *covellite*, which is 1: 1 of Cu: S.

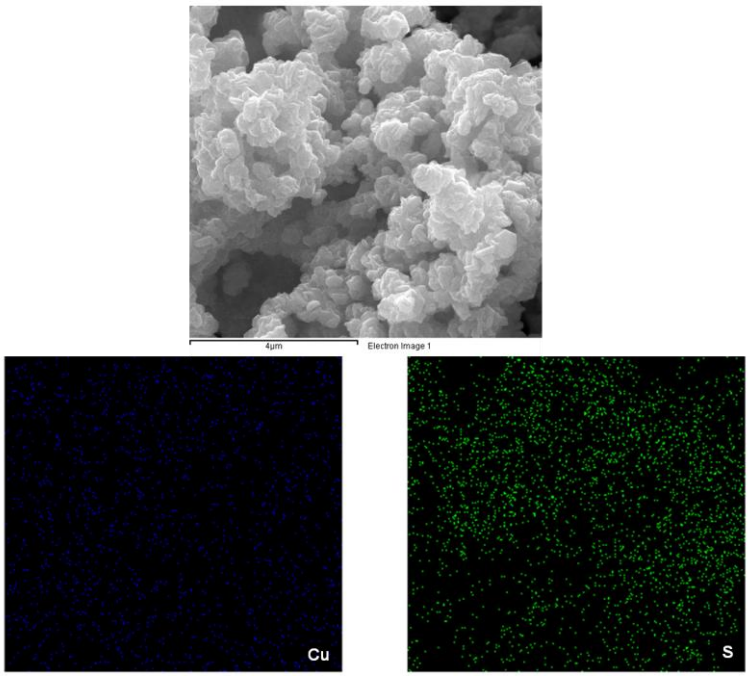

Figure 4.25: FESEM image and elemental map of *covellite*.

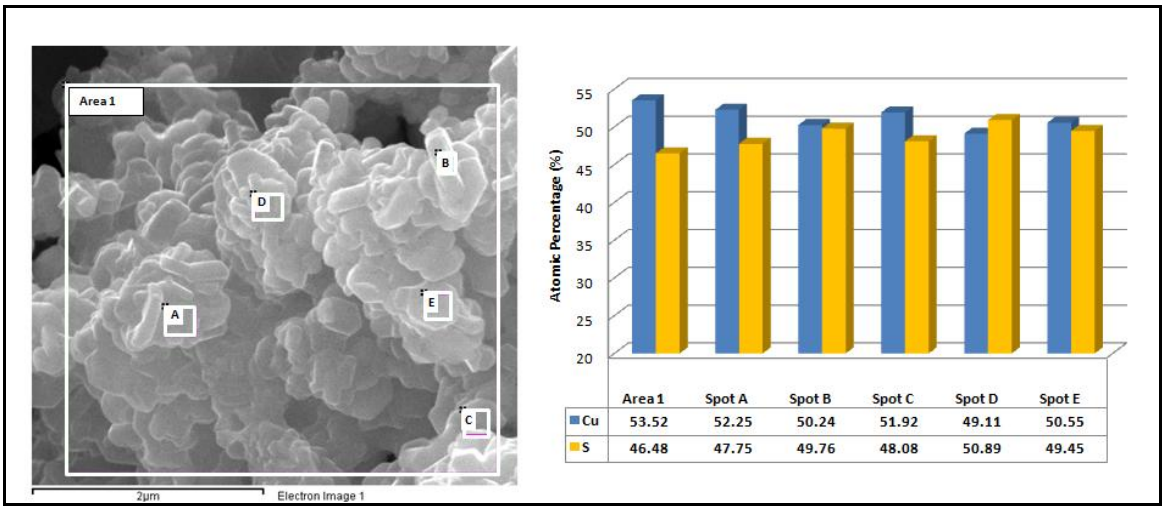

Figure 4.26: FESEM image and atomic composition of *covellite* (Area 1)[†].

[†]*The corresponding EDX spectra are attached in Appendix G.*

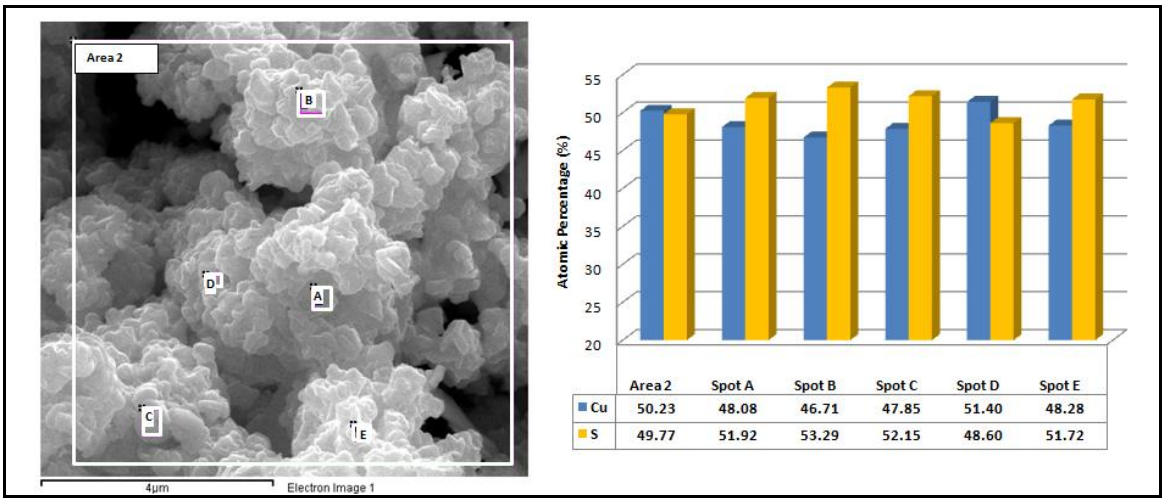

Figure 4.27: FESEM image and atomic composition of *covellite* (Area 2)[†].

[†]*The corresponding EDX spectra are attached in Appendix H.*

The FESEM image of *digenite* specimen and its respective elemental map (Cu and S) are depicted in **Figure 4.28**. It can be noted that Cu and S are evenly distributed on the surface of *digenite* sample. Similarly, *digenite* sample has homogeneous distribution of Cu and S as exhibited by *covellite*. Detailed atomic composition of *digenite* sample is shown in **Figures 4.29** and **4.30**. The relative atomic composition of *digenite* taken on different spots and areas demonstrates almost 65: 35 of Cu: S in average. This result is in good correlation with the nominal stoichiometric of digenite which 9: 5 of Cu: S.

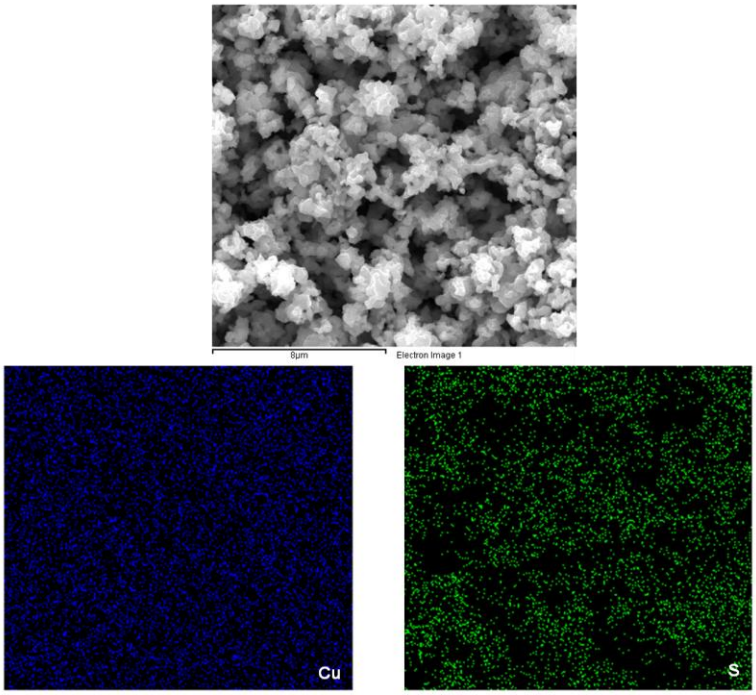

Figure 4.28: FESEM image and elemental map of *digenite*.

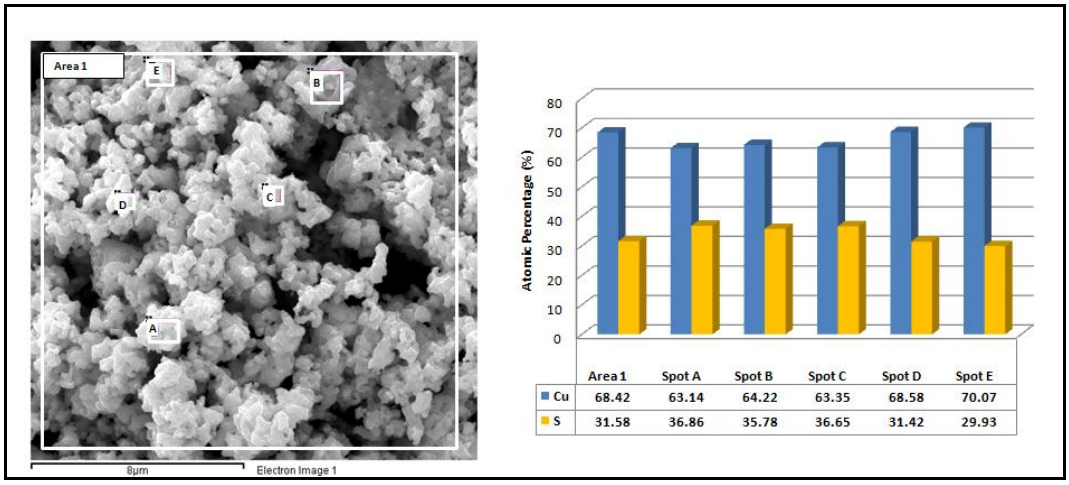

Figure 4.29: FESEM image and atomic composition of *digenite* at different spots (Area 1)[†].

[†]The corresponding EDX spectra are attached in Appendix I.

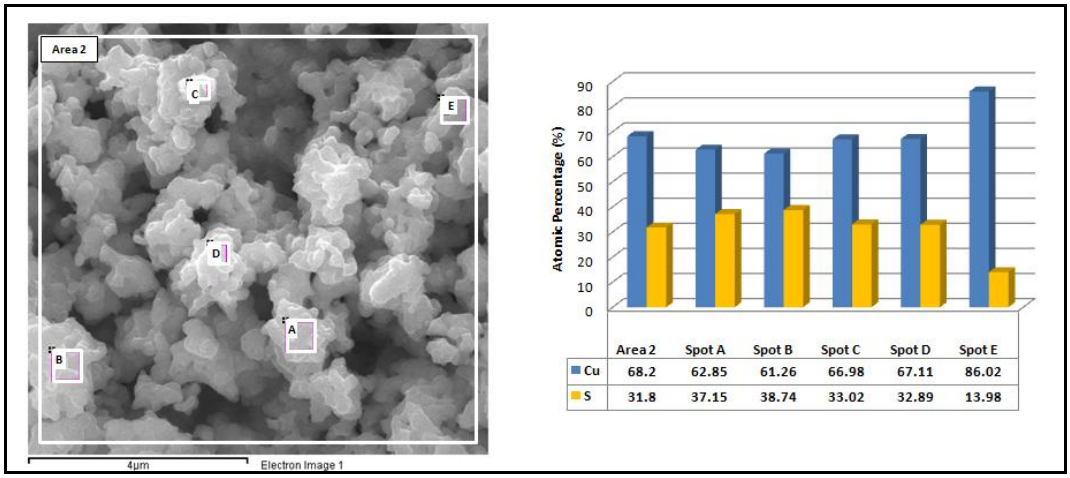

Figure 4.30: FESEM image and atomic composition of *digenite* at different spots (Area 2)[†].
[†]*The corresponding EDX spectra are attached in Appendix J.*

(b) Atomic Structure, and Microstructural Properties

The microstructure of the as-synthesized *covellite* is further studied with HRTEM technique. The electron micrographs captured on the *covellite* are depicted in **Figure 4.31**. It is obvious that CuS is found in bulk and highly agglomerated structure as observed in FESEM images previously. Nonetheless, the hexagonal nanoplates could hardly be speckled here due to the multilayer stacks of nanoplates formation. Meanwhile, the electron micrographs also exhibit highly crystalline framework of *covellite* which is in good correlation with the long range order material determined by powder XRD in previous section. Moreover, the lattice fringes of (101) and (102) revealed by the power spectrum are found to in good agreement with hexagonal *covellite* (PDF 06-0464) as discussed in powder XRD earlier.

In contrast, monoclinic *djurleite* ($Cu_{31}S_{16}$) is also found on the Fourier Transform pattern captured on the CuS sample as shown in **Figure 4.32(c).** The diffraction spots correspond to the d-spacings of monoclinic *djurleite* which can be indexed to PDF 42-564 can be determined from the respective power spectrum. This is because of the beam

damage (as shown in **Figure 4.32**) happened during the bombardment of the highly-focus electron beam onto the sample which results in the removing of sulfur from the specimen. As a result, the sample experienced structural changes and amorphisation, which lead to the formation of sulfur-deficient sulfide compounds like *djurleite*.

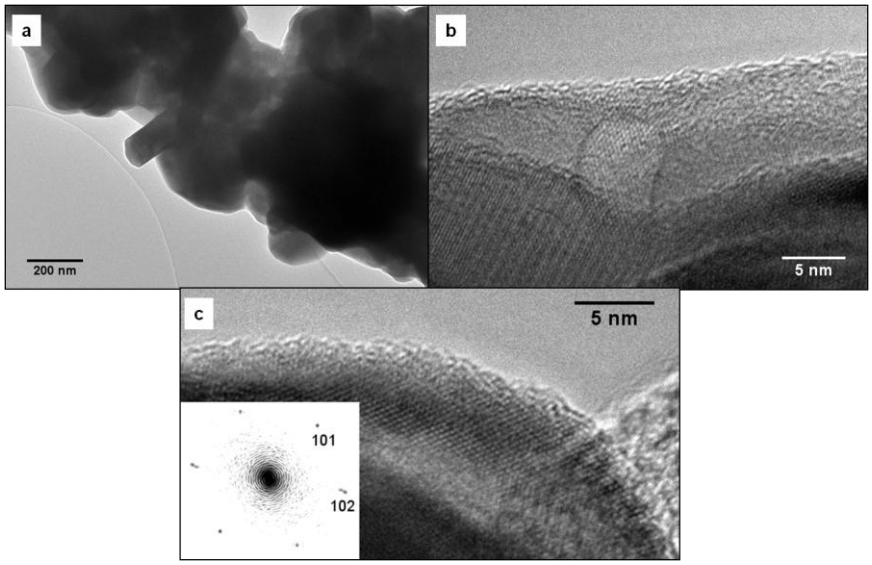

Figure 4.31: HRTEM images of (a) *covellite*, CuS in massive material (b) Cross-section of CuS nanoplate (c) Power spectrum shows the lattice fringes from CuS nanoplate.

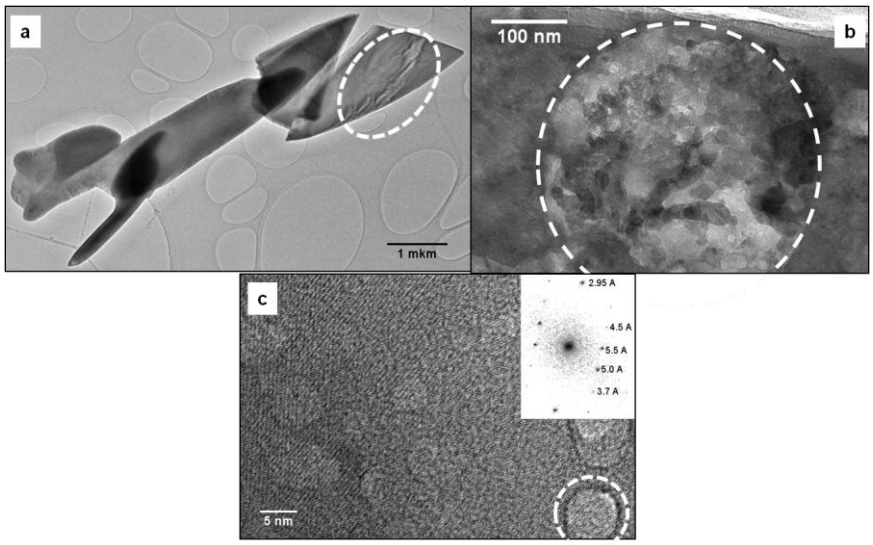

Figure 4.32: (a) Electron micrograph of CuS thin platelets under electron beam (beam damage shown in white-dotted line) (b) Beam damage (in white-dotted line) captured on CuS nanoplates (c) Beam damage taking under electron beam (in white-dotted lines); Fourier transform pattern shows d-spacings of monoclinic structure with large unit cell, *djurleite* ($Cu_{31}S_{16}$- PDF 42-564).

The HRTEM images of *digenite* are captured as displayed in **Figure 4.33**. The structure of *digenite* transmitted by the electron micrograph is analogous to the *covellite* where a highly agglomerated structure is observed. No distinct shape or morphology can be identified from the HRTEM micrographs. In this particular sample, no distinct lattice fringes can be distinguished for rhombohedral *digenite* (Cu_9S_5). Yet, the Fourier Transform of the micrograph (**Figure 4.34**) discloses that a highly crystalline area (assuming in [102] orientation) of the *digenite* is indeed consisted of lattice fringes which can be attributed to Cu_2S. Besides that, power spectrum of another HRTEM image (**Figure 4.35**) illustrates that another highly crystalline area of *digenite* composed of lattice fringes which can be assigned to CuS assuming in [211] orientation. This is due to the fact that most of the Cu_xS_y crystalline compounds have similar lattice distances and therefore it is difficult to identify precisely the numerous Cu_xS_y based on the TEM data. Furthermore, the 'evaporation' of sulfur during TEM measurement due to the unstable of the copper sulfides and beam damage has also contributed to the incompatible result collected. Therefore, the TEM results were inconclusive for *covellite* and *digenite* as the reasons provided in above. In fact, the identification of the samples by employing powder PXRD technique is more reliable as the majority of the copper sulfides showing indistinguishable lattice fringes in TEM analysis.

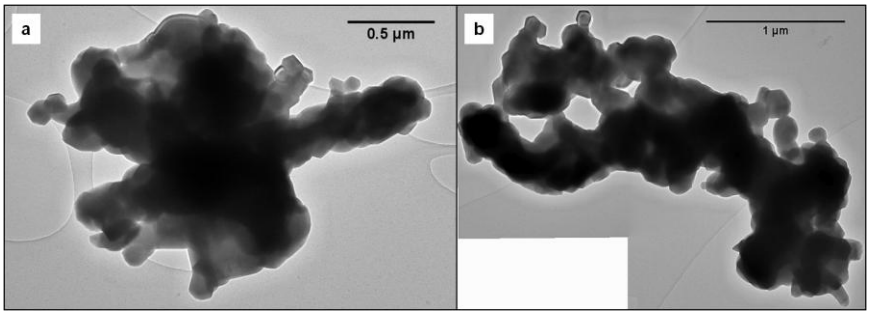

Figure 4.33: HRTEM images of *digenite* found in highly agglomerated structure.

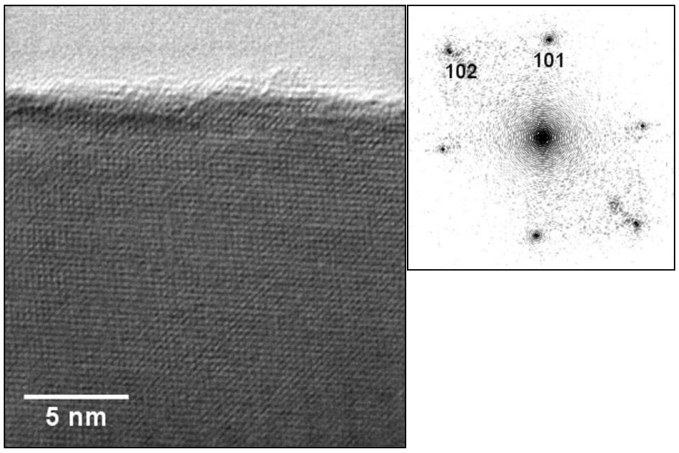

Figure 4.34: Electron micrograph of highly crystalline image captured on *digenite* sample. Power spectrum of the micrograph illustrates lattice fringes of Cu_2S assuming in [102] orientation.

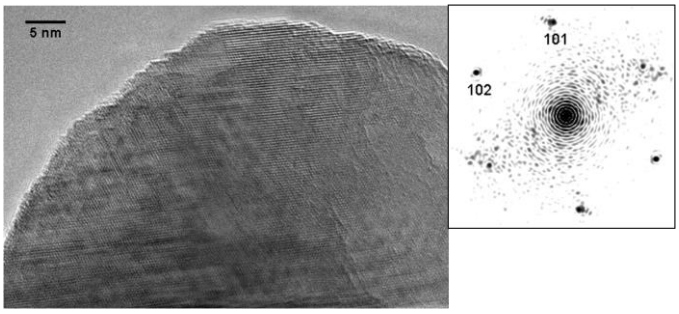

Figure 4.35: Electron micrograph of highly crystalline image captured on *digenite* sample. Power spectrum of the micrograph depicts lattice fringes of CuS assuming in [211] orientation.

(c) Surface Area and Porosity

Brunnauer-Emmet-Teller (BET) gas sorptometry measurement was used to further investigate the porous structure of the phase pure materials. The specific surface area, total pore volume, and the average pore diameter of CuS and C_9S_5 were determined. Both of the two phase pure compounds exhibit similar nitrogen adsorption/desorption isotherms as displayed in **Figures 4.36** and **4.37**. Both of the products display shape of isotherms which are convex to *p/p°* axis over its entire range with gradual curvature and show indistinct Point B. The characteristics of the shape of the isotherms are related to the reversible Type III isotherm but due to the significant appearance of hysteresis loops, they can be classified

as Type V isotherm. According to IUPAC (Sing, et al., 1985), the Type V isotherm is uncommon; the adsorbent-adsorbate interaction is weak and it is often obtained with certain porous adsorbents. From the viewpoint of hysteresis loops, it can be viewed that both of the isotherms do not exhibit any limiting adsorption at high *p/p°*. This can be regarded as the Type H3 loop which is normally observed with aggregates of plate-like particles giving rise to slit-shaped pores. This justification is consistent with the FESEM image (shown in **section 4.2.3**) where highly agglomerated plate-like structures were observed. **Table 4.11** tabulates the results of specific surface area, average pore size, and total pore volume of the phase pure samples. The BET surface area of CuS and Cu_9S_5 was calculated to be 15 and 3 m^2/g, while the total pore volume was 0.029 and 0.014 cm^3/g respectively. The average pore size was 7.63 and 20.58 nm for CuS and Cu_9S_5 correspondingly determined with *Barett-Joyner-Halenda* (BJH) method. The surface area of CuS is relatively higher than Cu_9S_5, however both of these materials can be regarded as materials with low surface area as compared to other high surface area materials such as zeolites, porous carbons, and amorphous silicas. The reason of CuS possesses higher surface area than Cu_9S_5 might be due to the perpendicular arrangement of the hexagonal platelets of CuS which gives rise to certain porosity during gas flow. In short, both of these materials can be considered as non-porous materials with low surface area as elucidated from the narrow hysteresis loops. Previous study carried out by *C. Wu et al.* have demonstrated that the BET surface area of the synthesized CuS nanotubes was 12 m^2/g by using copper nanowires, copper nitrate, ethylenediamine, and sodium hydroxide as precursors (Wu, et al., 2006). On the other hand, CuS prepared by *M. Li et al.* using copper sulfate, thiourea, and chitosan as a template possessed BET surface area of 31.72 m^2/g (Li, et al., 2010).

Table 4.11: Results of surface area and porosity for phase pure samples.

Sample ID	Remarks (phase identification from PXRD)	Surface area (m^2/g)	Multipoint BET (R^2)	Total pore volume (cm^3/g)	Average pore size (nm)
H05	Hexagonal phase *covellite* (CuS)	15	1.0000	2.882×10^{-2}	7.63
H07	Rhombohedral phase *digenite* (Cu_9S_5)	3	0.9941	1.417×10^{-2}	20.58

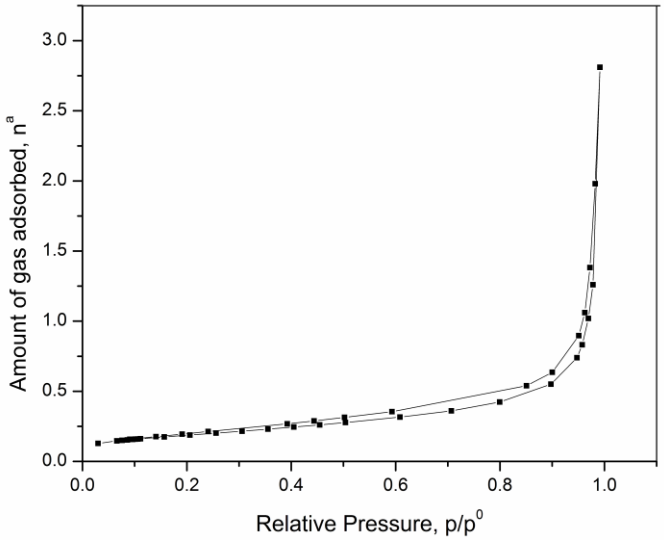

Figure 4.36: Nitrogen sorption isotherms of phase pure *covellite* (H05).

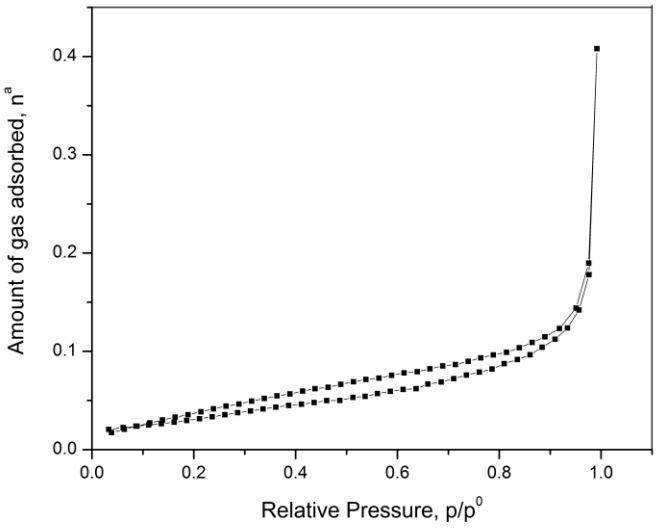

Figure 4.37: Nitrogen sorption isotherms of phase pure *digenite* (H07).

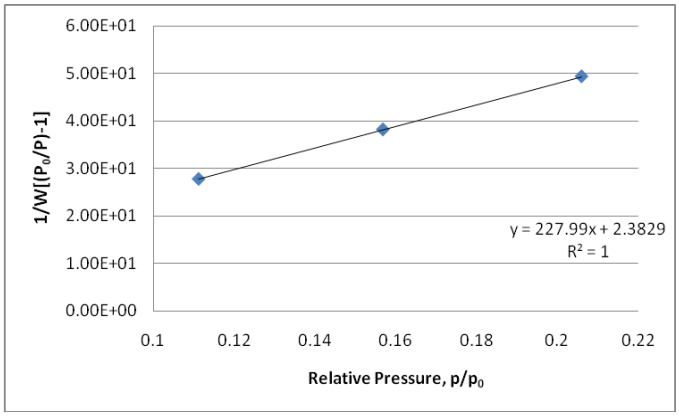

Figure 4.38: Multipoint BET measurement of phase pure *covellite* (H05).

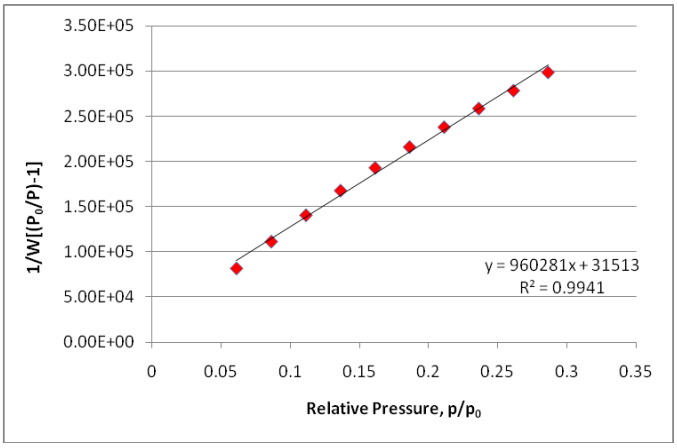

Figure 4.39: Multipoint BET measurement of phase pure *digenite* (H07).

(d) Thermal Stability

The thermal stability of the prepared phase pure materials (CuS and Cu_9S_5) was studied by employing TGA-MS and DSC analysis. The thermal studies for both of the materials were conducted in two different environments, *i.e.* A linear ramp from 298-873 K at a heating rate of 5 K/ min, under flow of 100 % Ar gas at 70 cm^3/ min; a linear ramp from 298 - 873 K at a heating rate of 5 K/ min, in the flow of 21 % O_2 gas (21 cm^3/ min) in Ar gas at 49 cm^3/ min. The first condition was chosen to verify if the samples analyzed are of phase pure compounds. The latter condition was selected to mimic the atmospheric condition with no interference from other atmospheric gases like carbon dioxide, or water vapor. The

gases evolved from the samples during the thermal treatment were analyzed by MS technique. The details of the DSC thermogram analysis are tabulated in **Table 4.12**.

Table 4.12: Transition temperature (T_{onset} & $T_{midpoint}$), and enthalpy of samples extracted from DSC curve at different heating atmosphere.

Sample	1st Transition		2nd Transition		3rd Transition		4th Transition	
	T_{onset} & $T_{midpoint}$ (K)	ΔH (J/g)	T_{onset} & $T_{midpoint}$ (K)	ΔH (J/g)	T_{onset} & $T_{midpoint}$ (K)	ΔH (J/g)	T_{onset} & $T_{midpoint}$ (K)	ΔH (J/g)
H05 in inert atm	T_{on}= 306 T_{mid} =335	-9.622 (endo)	T_{on}= 546 T_{mid} =573	-2.581 (endo)	T_{on}= 670 T_{mid} =706	-12.342 (endo)	NA	NA
H07 in inert atm	T_{on}= 362 T_{mid} =372	-0.184 (endo)	NA	NA	NA	NA	NA	NA
H05 in oxidic atm	T_{on}= 519 T_{mid} =586	4.764 (exo)	T_{on}= 597 T_{mid} =612	175.76 (exo)	T_{on}= 639 T_{mid} =652	10.448 (exo)	T_{on}= 767 T_{mid} =778	19.557 (exo)
H07 in oxidic atm	T_{on}= 560 T_{mid} =577	13.055 (exo)	T_{on}= 593 T_{mid} =632	184.46 (exo)	T_{on}= 767 T_{mid} =777	32.323 (exo)	NA	NA

Figure 4.40 shows the TGA-DSC, and Differential Thermalgravimetric (DTG) curves for phase pure CuS (H05) in a linear ramp from 298-873 K at a heating rate of 5K/ min, in the flow 100 % Ar gas at 70 cm^3/min. In this analysis, 9.500 mg of sample was subjected for thermal analysis. Generally, the decomposition of phase pure CuS (H05) can be divided into three major steps. The first and second mass loss can be attributed to the loss of moisture and water of crystallization in the range of 311-438 K and 490-621 K respectively. A corresponding shallow broad endotherm from DSC was observed at the 1st mass loss can be related to the moisture loss; whilst a well-defined endotherm at 2nd mass loss was associated to the loss of solvated or coordinated water. The loss of moisture and

crystallization of water which account for a total of 5.36 % can be viewed as endothermic reactions from DSC curve. These are evidenced by the MS result whereby two intense peaks at mass-to-charge ratio (m/z) of 18 corresponding to water were observed at 338 K and 571 K as shown in **Figure 4.43**. The third mass loss at 11.95 % occurred at 618-743 K can be correlated to the decomposition of CuS with the formation of copper deficient compounds. It can be seen from the DSC curve where an endothermic event has taken place with a large well-defined peak arose at 705 K. None of the mass spectrum was detected at this step. It was reported that *anilite* (Cu_7S_4) was formed from *covellite* in the temperature range 278-354 °C, followed by the decomposition to Cu_2S at temperature 500-615 °C when *covellite* was heating in an inert atmosphere (Brunetti, Piacente, & Scardala, 1994; Dunn & Muzenda, 2001). Additional thermal study was conducted to find that four endothermic peaks were observed at 280, 450, 550 and 830 °C were ascribed to the transformation of CuS into cubic *digenite* (Cu_9S_5), cubic *djurleite* ($Cu_{31}S_{16}$), and *chalcocite* (Cu_2S) and finally to copper (Dunn & Muzenda, 2001). Therefore, it is believed that the synthesized phase pure *covellite* (CuS) has been transformed to *anilite* at 490-621 K, followed by the decomposition to *chalcocite* at 622-743 K. All the steps involved have contributed to 17.31 % (1.6444 mg) mass loss.

Figure 4.41 illustrates the TGA-DSC, and DTG curves for phase pure Cu_9S_5 (H07) in a linear ramp from 298-873 K at a heating rate of 5K/ min, in the flow 100 % Ar gas at 70 cm^3/min. The stepwise decomposition of phase pure Cu_9S_5 (H07) in inert atmosphere can be categorized into two significant processes: melting, and crystal structure rearrangement. The 1st and 2nd mass loss which happened in the range of 302-351 K and 352-473 K can be correlated to the melting process of crystal digenite. A broad and a sharp

endotherm peaks were found at 345 and 371 K from DSC curve which indicates the melting of pure crystal. No MS peak was observed at these 2 steps, indicating that no gaseous / volatile compound was evolved and no moisture or water MS peak were found at these ranges of temperature. This is followed by a significant mass loss in the range of 474-681 K which can be ascribed by crystal structure rearrangement of the aforementioned compound. A large and broad exotherm shown from the DSC curve was observed and no MS peak was detected at this step as well. It is believed that *digenite* might have rearranged its structure to a more stable system at higher temperature. The total mass loss contributed by this sample (phase pure *digenite*- H07) was relatively insignificant compared to phase pure CuS (H05), which was only 1.11 % of the total mass 21.000 mg initially.

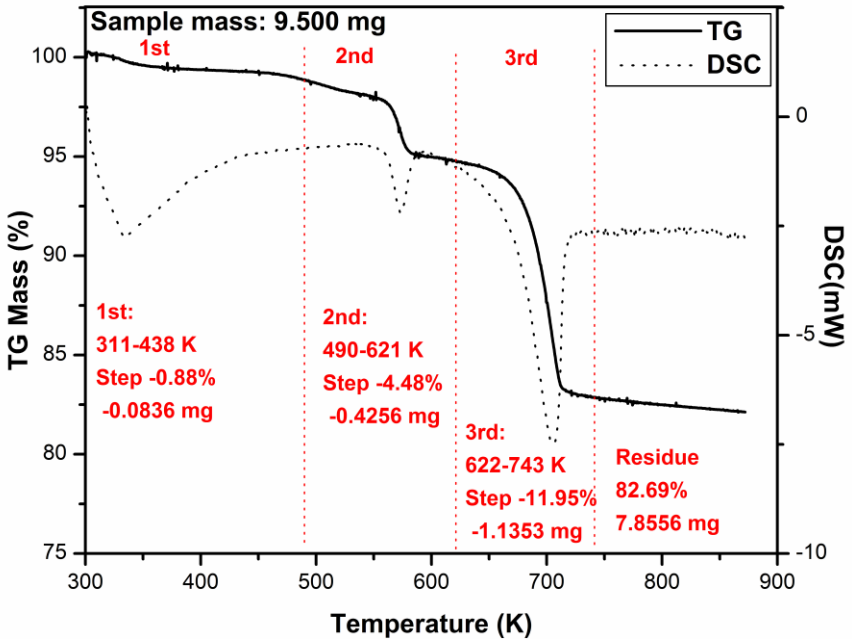

Figure 4.40: TGA-DSC curve of phase pure CuS (H05) in 100 % Ar gas heated up to 873 K at 5K/ min with flow rate of 70 cm^3/ min.

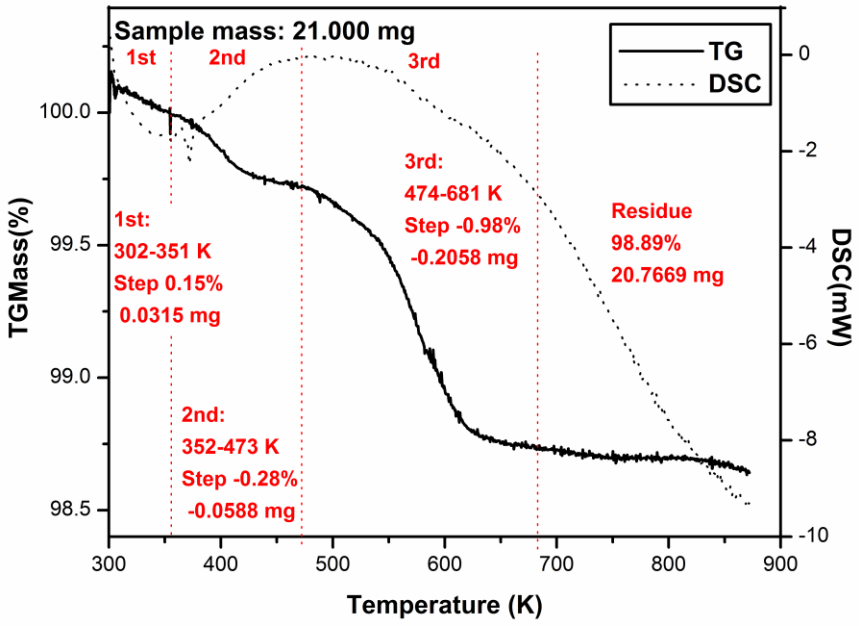

Figure 4.41: TGA-DSC curves of phase pure Cu_9S_5 (H07) in 100% Ar gas heated up to 873 K at 5 K/ min with flow rate of 70 cm^3/ min.

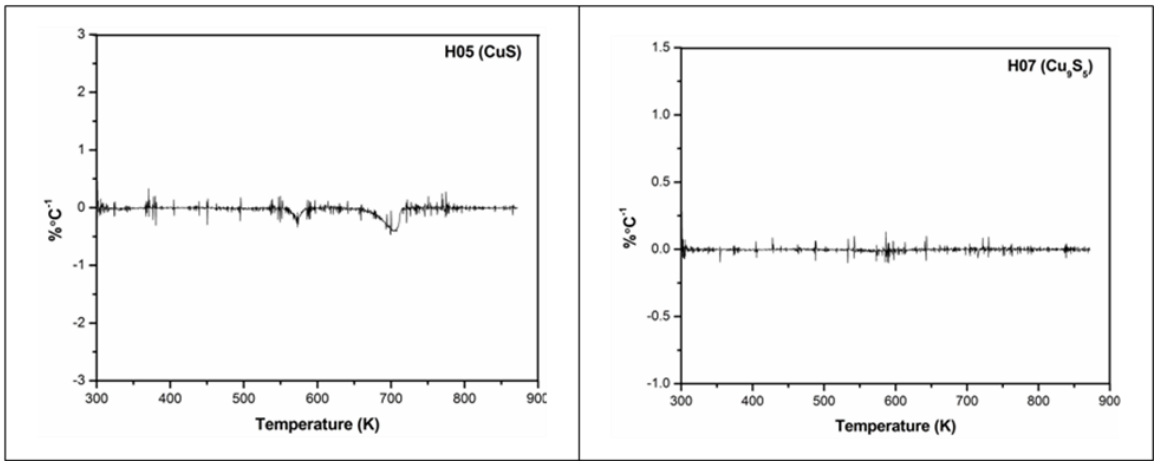

Figure 4.42: DTG curve of phase pure Cu_9S_5 (H07) in 100 % Ar gas heated up to 873 K at 5 K/ min with flow rate of 70 cm^3/ min.

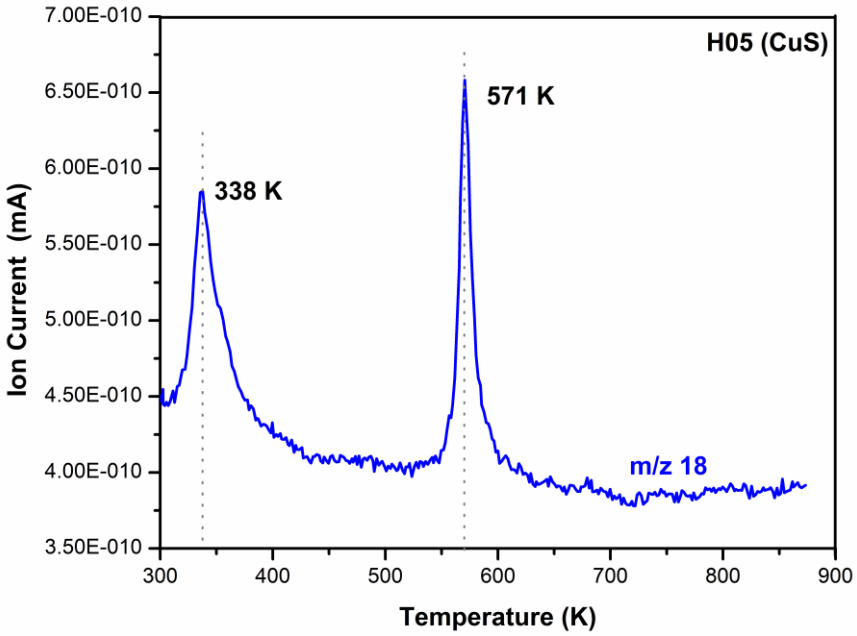

Figure 4.43: Evolution of compounds observed by mass spectroscopy with respect to the mass-to-charge ratio (m/z) for phase pure CuS.

On the other hand, both of the phase pure samples were found to have different thermal pattern (compared to the inert condition) when these materials were subjected under a linear ramp from 298-873 K at a heating rate of 5 K min^{-1}, in the flow of 21 % O_2 gas (21 cm^3/ min) and Ar gas (49 cm^3/ min). The DTG curve and the mass spectroscopy results of both of these samples under thermal oxidation are displayed in **Figures 4.45** and **4.46** respectively. The TGA-DSC curves of phase pure CuS (H05) under thermal oxidation is illustrated in **Figure 4.44**. For phase pure CuS (H05), it can be observed that an insignificant mass loss escorted by a broad exothermic drift occurred in the range of 302-520 K under oxidic atmosphere. This can be related to the decomposition of some of the *covellite* to *digenite*, with subsequent oxidation of the liberated sulfur besides the loss of moisture and water of crystallization at this stage. The MS signal where peak at m/z 18 was detected at 370 and 535 K. The following reactions were suggested where Reactions (1), (2) and (3) were recommended by *J. G. Dunn and C. Muzenda* (Dunn & Muzenda, 2001):

$$1.8CuS \rightarrow Cu_{1.8}S + 0.8S \quad (1)$$

$$2CuS + O_2 \rightarrow Cu_2S + SO_2 \quad (2)$$

$$0.8S + 0.8O_2 \rightarrow 0.8SO_2 \quad (3)$$

$$0.8S + 0.4O_2 \rightarrow 0.8SO \quad (4)$$

Reactions (1) and (2) are accounted for the mass loss while Reactions (3) and (4) are responsible for the exothermic peak. The lack of detection of SO and SO_2 might due to the minor liberation of these gases which were still below the detection limits of the equipment (Dunn & Muzenda, 2001). Meanwhile, a major mass loss accompanied by an exothermic peak occurred between 520-602 K which can be related to the oxidation of CuS to Cu_2S and Cu_2O. The following reactions were recommended by *J. G. Dunn and C. Muzenda* (Dunn & Muzenda, 2001), except for Reaction (6):

$$2CuS + O_2 \rightarrow Cu_2S + SO_2 \quad (5)$$

$$CuS + 0.5O_2 \rightarrow Cu_2S + SO \quad (6)$$

$$Cu_2S + 0.01O_2 \rightarrow Cu_{1.96}S + 0.02\ Cu_2O \quad (7)$$

$$Cu_2O + SO_2 + 0.5O_2 \rightarrow Cu_2SO_4 \quad (8)$$

$$Cu_2O + 2SO_2 + 1.5O_2 \rightarrow CuSO_4 \quad (9)$$

The detection of SO and SO_2 from the MS result coincides well with the suggested reactions where m/z of 48 and 64 which can be corresponded to SO and SO_2 respectively were found at 535 and 546 K. Between 603-635 K, an apparent mass gain happened associated with a significant exothermic peak. This event can be correlated to the further oxidation of the core sulfides with the increase in temperature. The reactions below were proposed based on the previous study done (Dunn & Muzenda, 2001):

$$Cu_2S + 1.5O_2 \rightarrow Cu_2O + SO_2 \quad (10)$$

$$Cu_2O + 2SO_2 + 1.5O_2 \rightarrow 2CuSO_4 \quad (11)$$

$$3Cu_2SO_4 \rightarrow 2Cu_2O + 2CuSO_4 + SO_2 \quad (12)$$

Finally, in the temperature range of 719-833 K, a gradual mass gain associated with a well-defined exothermic peak were observed. At this stage, it is believed that the solid state reaction occurs which causes melting and further rapid oxidation of the remaining sulfide as well as sulfation of the oxide formed. The following reactions were proposed according to *J. G. Dunn and C. Muzenda* (Dunn & Muzenda, 2001):

$$Cu_2S + 2CuSO_4 \rightarrow 2Cu_2O + 3SO_2 \quad (13)$$

$$2CuSO_4 \rightarrow CuO.CuSO_4 + SO_2 + 0.5O_2 \quad (14)$$

$$Cu_2O + 4CuSO_4 \rightarrow 3CuO.CuSO_4 + SO_2 \quad (15)$$

Again, a small MS peak at m/z of 64 was detected at 778 K which correlates well with the proposed reactions where SO_2 gas was evolved at this stage. All the aforementioned reactions were proposed based on the experimental observations by applying PXRD, and FTIR techniques done by the previous research team (Dunn & Muzenda, 2001).

Meanwhile, phase pure Cu_9S_5 (H07) was found to have a slightly different thermal oxidation behavior when it was subjected under oxidic atmosphere. The TGA-DSC curves of phase pure Cu_9S_5 (H07) under thermal oxidation is depicted in **Figure 4.45**. Overall, the thermal oxidation of Cu_9S_5 can be divided into 3 major steps. The 1st step occurred in the temperature range of 300-594 K, where a steady mass gain accompanied by an exothermic drift can be observed from the TGA-DSC curves. This event can be regarded as a slow

decomposition of Cu_9S_5 to Cu_2S with the subsequent oxidation of the liberated S. The reactions were suggested as the following:

$$Cu_9S_5 \rightarrow 4.5\ Cu_2S + 4S \quad (16)$$

$$Cu_2S + 1.5O_2 \rightarrow Cu_2O + SO_2 \quad (17)$$

$$Cu_2S + O_2 \rightarrow Cu_2O + SO \quad (18)$$

These reactions were evidenced by the MS results where m/z of 48 and 64 which correspond to SO and SO_2 were found at 535 and 546 K. This indicates that the suggested reactions are in good agreement with the MS results. Besides that, it can be noticed that a broad MS peak at m/z 18 which can be ascribed to water compounds arose at 400 K, implying that the loss of moisture from the material at this stage. The second event took place at 595-686 K where another gradual mass gain associated with a sharp exothermic peak can be identified from the curves. The mass gain and the exothermic peak can be related to the oxidation of the sulfides to sulfate compounds. The reactions responsible for this step were recommended as below:

$$Cu_2O + 2SO_2 + 1.5O_2 \rightarrow 2CuSO_4 \quad (19)$$

Only MS peak at m/z 18 corresponded to water molecule was detected at 632 K. This might due to the loss of remaining crystallization water from the sample which cannot be completely eliminated in the 1st stage. No MS peak at 48 and 64 was observed. This is followed by the 3rd step of the thermal oxidation where a further mass gain coupled with a sharp well-defined exotherm happened at 687-804 K. This can be regarded as the melting process and further sulfation of the oxide compounds. The following reactions were proposed:

$$2CuSO_4 \rightarrow CuO.CuSO_4 + SO_2 + 0.5O_2 \quad (20)$$

$$Cu_2O + 4CuSO_4 \rightarrow 3CuO.CuSO_4 + SO_2 \quad (21)$$

The evolution of SO_2 gases at this stage was supported with the MS result where peak at m/z 64 was found at 778 K as shown in **Figure 4.47**. In general, the thermal behavior of Cu_9S_5 was found to be slightly different from CuS in oxdic atmosphere as there was no mass loss during the entire thermal steps for Cu_9S_5. However, it can be noticed that the DSC curve for both of these materials are quite alike where 3 exothermic peaks were observed during the entire heating process in oxidic atmosphere. This shows that both of these materials might have undergone quite similar phase transformations and oxidation processes.

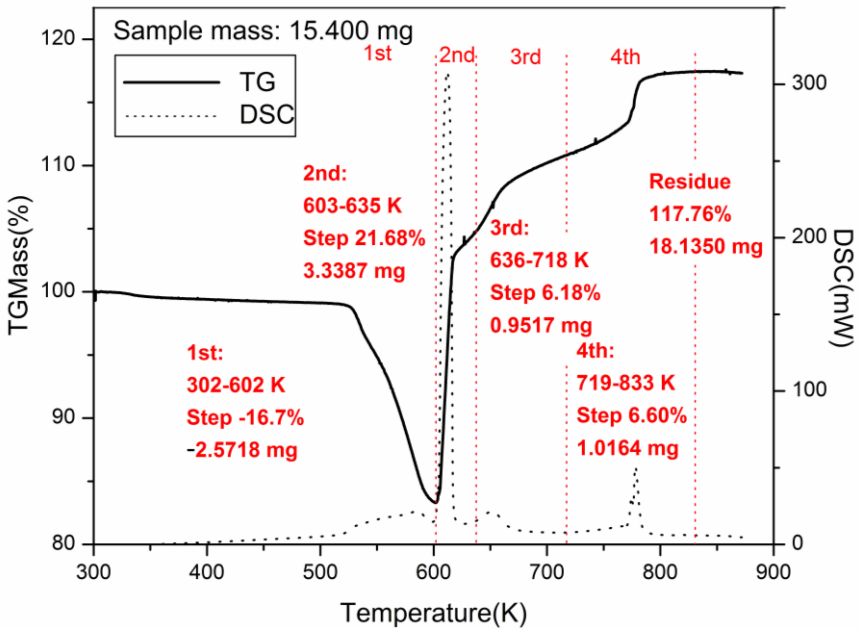

Figure 4.44: TGA-DSC curve of phase pure CuS (H05) in 21 % O_2 gas (21 cm^3/ min) and Ar gas (49 cm^3/ min) flow heated up to 873 K at 5 K/ min.

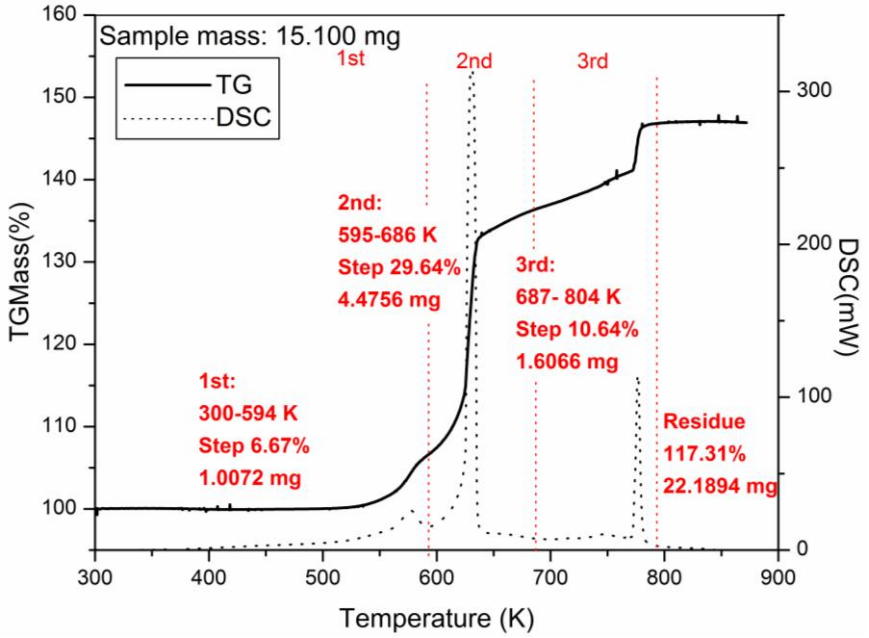

Figure 4.45: TGA-DSC curve of phase pure Cu_9S_5 (H07) in 21 % O_2 gas (21cm^3/ min) and Ar gas (49 cm^3/ min) flow heated up to 873 K at 5 K/ min.

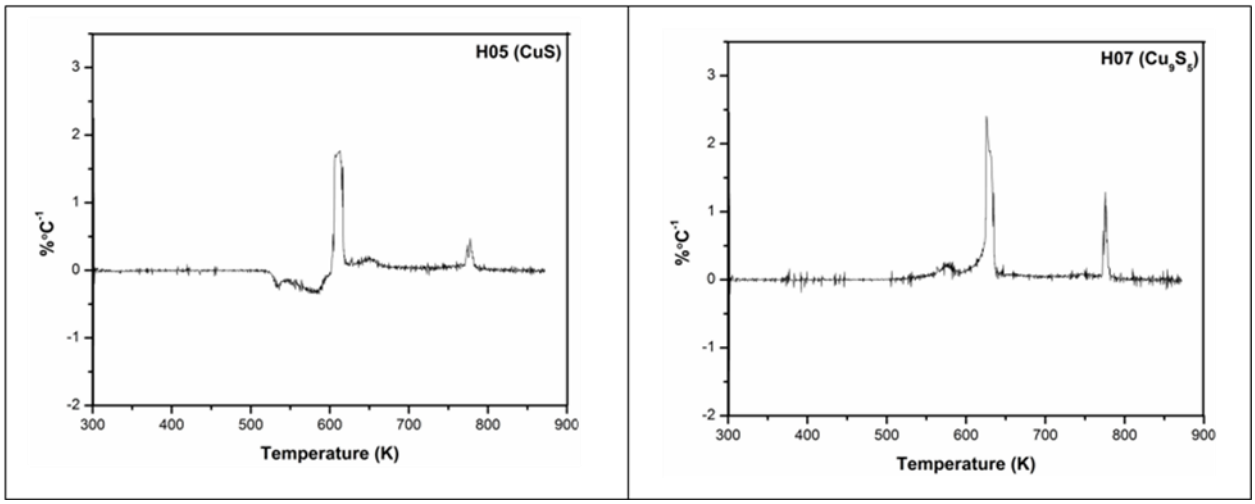

Figure 4.46: DTG curve of phase pure samples in 21 % O_2 gas (21 cm^3/ min) and Ar gas (49 cm^3/ min) flow heated up to 873 K at 5 K/ min.

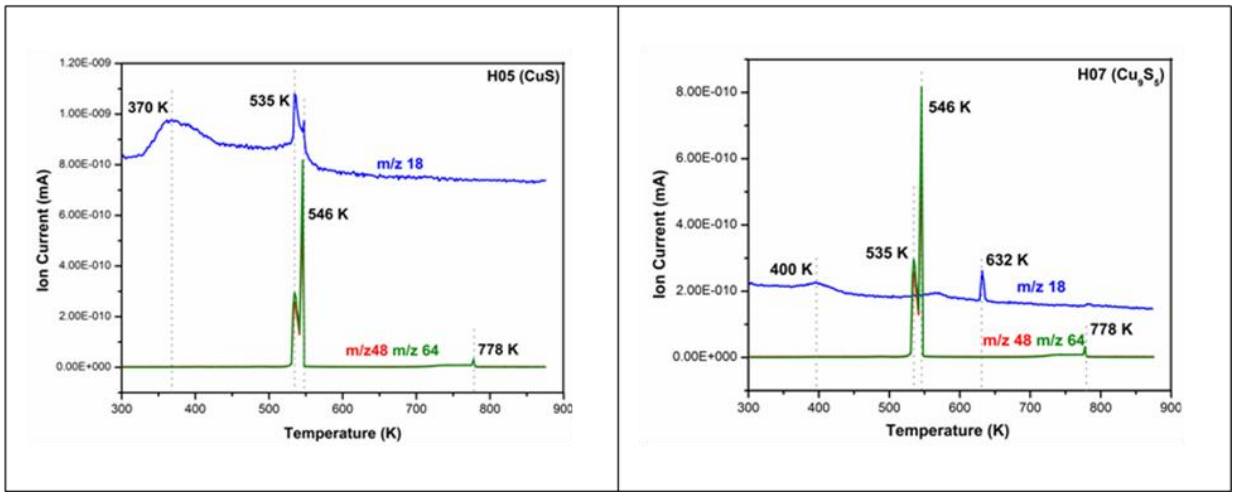

Figure 4.47: Evolution of compounds observed by mass spectroscopy with respect to the mass-to-charge ratio (m/z) for phase pure samples.

4. 4. 2 Application of Covellite in Mercury Removal

In order to assess the potential ability of phase pure covellite (CuS) in removing aqueous Hg(II), the sorption experiment was conducted at a wide range of pH which included pH 1, 4, 7, and 9. The experiments were carried out in a batch equilibrium system and the equilibrium data obtained was tabulated in **Table 4.13**. The experimental sorption data were fitted with linear regression equation of Langmuir isotherm as shown below:

$$\frac{C_e}{Q_e} = \frac{C_e}{Q_{max}} + \frac{1}{bQ_{max}}$$

where C_e is equilibrium concentration of the solution, Q_e is equilibrium sorption capacity, b is sorption equilibrium constant, and Q_{max} is the maximum sorption capacity or complete monolayer sorption capacity.

As we can view from **Table 4.13**, the linear regression analysis suggested that the experimental data fitted well with Langmuir isotherm with all the coefficient of correlation calculated, R^2, greater than 0.9900. These values reflect that the sorption of Hg(II) onto CuS follows the *Langmuir* behavior where a monolayer sorption will be reached upon the

reaction equilibrium. When the sorption equilibrium is reached, the maximum amount of Hg(II) sorbed onto CuS can be determined. The experimental data at different pH were plotted as shown in **Figure 4.48**. As we compare the Q_{max} at various pH, acidic pH (pH 1 and 4) exhibits the best performance among the other pHs in removing aqueous Hg(II) with values of 434.78 and 398.41 mg/ g respectively. When the pH was further increased to 7 and 9, the performance of Hg(II) removal drops significantly to 169.49 and 97.18 mg/ g respectively. This shows that the ability of phase pure CuS in removing aqueous Hg(II) is poor at basic pH.

Table 4.13: Equilibrium data fitted with *Langmuir* isotherm.

Temperature (°C)	pH	R^2	Slope	Intercept	Q_{max}	b
25	1	0.9985	0.0023	1.84×10^{-5}	434.78	124.84
	4	0.9979	0.0025	9.89×10^{-5}	398.41	25.38
	7	0.9952	0.0059	9.73×10^{-2}	169.49	0.06
	9	0.9926	0.0103	1.32×10^{-1}	97.18	0.07

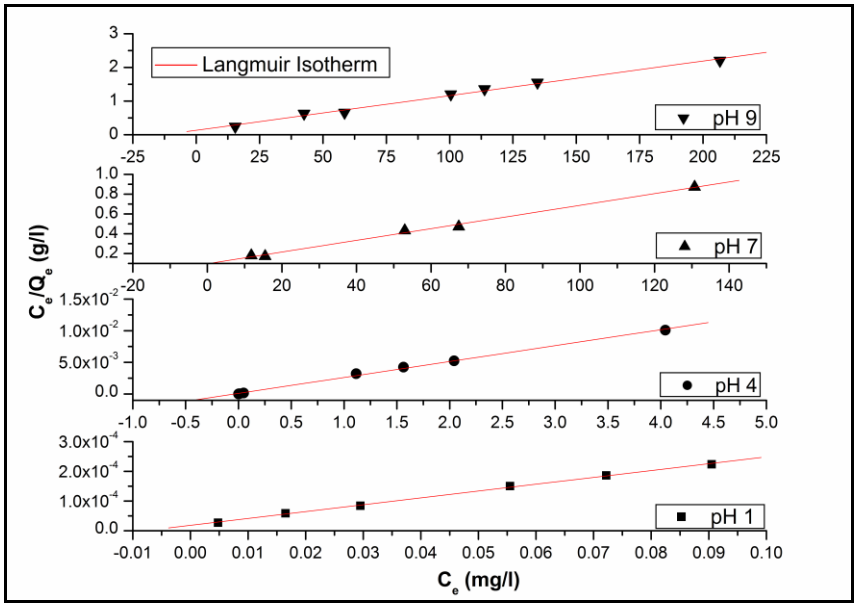

Figure 4.48: Linear plot of *Langmuir* isotherm at different pH.

Meanwhile, sorption equilibrium constant, *b*, is useful in evaluating the spontaneity of the reaction at different pH. This can be visualized by calculating thermodynamic parameter, $\Delta G°$ of the reaction as the equation is as shown below:

$$\Delta G° = -RT \ln b$$

where at 297.15 K: ΔG = -8.3145 × 297.15× *ln* (*b* × 200.59), molecular weight for Hg = 200.59 g/ mol. **Table 4.14** tabulates the calculated ΔG° at 25 °C for pH 1, 4, 7, and 9.The calculated ΔG° shows that the Hg(II) removal reaction is favorable at low pH due to the more negative value obtained. This calculation shows that the affinity of CuS in adsorbing mercury is favorable at low pH where Q_{max} determined previously also indicates that highest capacity falls at pH 1.

Table 4.14: Calculated ΔG° at different pH at 25 °C.

pH	ΔG° (kJ/mol) at 25°C
1	-25.09
4	-21.15
7	-6.19
9	-6.81

From the experimental data and the sorption isotherm fitting results, it is apparent that sorption of aqueous Hg(II) onto CuS are favored in a wide range of pH. With the good performance testing results demonstrated above, this further confirms the possibility and feasibility of CuS in removing aqueous Hg(II) particularly at acidic pH. The well-tested CuS can be modified accordingly to suit the desired applications in various sectors such as textile industry, oil and gas industry, wastewater industry, as well as environmental management.

4. 4. 3 Discussion

Phase pure copper sulfides have been prepared at 155 °C for 12 hours via hydrothermal route. Two phase pure copper sulfides were identified from the entire synthesis process, namely *covellite* and *digenite* which were formed at Cu: S mole ratio of 1: 2 and 1: 1.5 respectively. A series of characterization techniques such as powder PXRD, BET, FESEM, HRTEM, EDX, XRF, and TGA-MS/ DSC were employed to confirm the formation of these two phase pure materials besides probing the structural, chemical, and thermal properties of these products.

PXRD has identified that two phase pure materials which can be indexed to PDF 06-0464 (hexagonal *covellite*), and PDF 047-1748 (rhombohedral *digenite*) for products formed at 1: 2 and 1: 1.5 Cu: S mole ratio respectively. No crystalline impurity was detected from the PXRD diffractograms for both of these materials. SEM technique has demonstrated that both of the phase pure products have highly aggregated and agglomerated structure. Phase pure *covellite* displayed interlaced perpendicular hexagonal nanoplates, with a mean edge length of *ca.* 1-1.5 μm and an average thickness of *ca.* 50-100 nm. The single hexagonal morphology found in this powder corresponds well with the hexagonal phase of *covellite* determined by PXRD. Meanwhile, phase pure *digenite* exhibited circular nanoplates, with diameter of ca. 20-50 nm, and thickness of *ca.* 5-10 nm. Moreover, elemental composition determined by XRF and EDX showed values of 1: 1.04 and 1: 1.07 respectively for *covellite*; while 1: 0.64 and 1: 0.56 for *digenite*. This further supports the results from PXRD that the stoichiometric CuS and Cu_9S_5 are formed under this hydrothermal treatment.

Both of the phase-pure materials exhibit homogeneous distribution of Cu and S on the surface of the samples and this is further confirmed by the localized atomic composition

collected at several spots and areas on these samples. The lattice fringe fingerprinting (from HRTEM technique) applied to these two crystal systems have recognized a few Cu_xS_y crystal phases from these two compounds. The results were inconclusive due to the 'evaporation' of S and the similar lattice distances of the numerous Cu_xS_y. Therefore, this technique is less reliable in this study.

Furthermore, BET technique has determined that phase pure *covellite* and *digenite* possess surface area of 15 and 3 m^2/ g respectively. These two materials exhibit Type V isotherm due to the presence of significant hysteresis loop. The total pore volume were estimated as 2.882×10^{-2} and 1.417×10^{-2} cm^3/ g, while the average pore size were calculated to be 7.63 and 20.58 nm for *covellite* and *digenite* respectively. Both of these materials have very low surface area and are regarded as non-porous materials as elucidated from the narrow hysteresis loops of their N_2 isotherms.

In addition, TGA-MS has assisted the assumption of phase pure identity for both of the materials as this proves the absence of certain phases (sulfate) from these two materials during the heating in inert atmosphere. This further confirms the formation of phase pure *covellite* and *digenite*. The thermal behavior of these two materials was examined with TGA-MS and DSC in 21 % O_2 atmosphere. The DSC curves show that the overall thermal oxidation is an exothermic event for both of the materials which are in good agreement with the calculated ΔH. The thermal oxidation of CuS involves the decomposition of CuS to $Cu_{1.8}S$, followed by the oxidation of CuS to CuO, $CuSO_4$ and $CuO.CuSO_4$; while the thermal oxidation of Cu_9S_5 involves the decomposition of Cu_9S_5 to Cu_2S, followed by the oxidation reaction to become CuO, $CuSO_4$ and $CuO.CuSO_4$.

The performance testing of the most stable phase copper sulfide has been carried out in order to accomplish the goal of this research project which is to develop adsorbent

for trapping aqueous Hg(II). *Covellite*, is the most stable form copper sulfide, is found to be applicable in removing aqueous Hg(II) in a wide range of pH. The equilibrium data collected at 25 °C has revealed that the sorption of aqueous Hg(II) onto phase pure *covellite* obeys Langmuir model with R^2 over 0.9900 for experiments conducted at pH 1, 4, 7, and 9. The calculated maximum sorption capacity (Q_{max}) is found to decrease as pH increases. This explains that the mercury removal reaction by applying *covellite* is favorable in a wide range of pH, especially at low pH. To sum up, the phase pure materials have the potential ability in removing aqueous mercury (Hg^{2+}) based on the collected supporting preliminary performance assessment data. However, the practical application of this material in the environmental system has to be considered in terms of its selectivity towards other metal ions, recovery of the respective adsorbent after sorption, disposal of Hg- loaded adsorbent and economical cost of this material for industrial application. Nevertheless, we believe that all the considerations regarding the respective material can be easily solved with various modifications made on the material where necessary in the future.

4. 5 Phase Stability Studies of CuS

In the previous part, a single phase copper sulfide (*covellite*) has been successfully prepared and tested to have the potential as a mercury removing agent in aqueous system. However, this as-formed material was found to be not stable in the air at ambient temperature in which it has been transformed to a phase mixture of pentahydrate copper sulfate and copper sulfide instead of a phase pure *covellite* initially. Therefore, a systematic study has been carried out to study the phase transformation of this material with time. Besides that, the evidences of the phase transformations of this material will be elucidated by different characterization methods such as PXRD, EDX, and TGA-MS/ DSC.

4. 5. 1 Evidence of Phase Transformation

Figure 4.49 (a) shows the diffraction patterns of as-prepared product of CuS formed with Cu: S mole ratio of 1: 2 under 155.0 °C for 12 hours. The observed diffraction peaks of the phase pure CuS can be indexed to the hexagonal CuS, *covellite* (PDF 06-0464). No other crystalline impurity was detected, indicating that pure CuS is produced. However, the same product was found to consist of a phase mixture after 6 months of synthesis. **Figure 4.49 (b)** exhibits the PXRD pattern of the same product when it was placed at ambient condition in air after 6 months of synthesis. Additional crystalline phase of pentahydrate copper sulfate ($CuSO_4.5H_2O$) which can be indexed to PDF 77-1900 was observed besides the hexagonal *covellite* which was found earlier. *Rietveld* quantification analysis further confirmed that the phase-pure CuS has been transformed to a phase mixture of 67 % CuS and 33 % $CuSO_4.5H_2O$ as tabulated in **Table 4.15**.

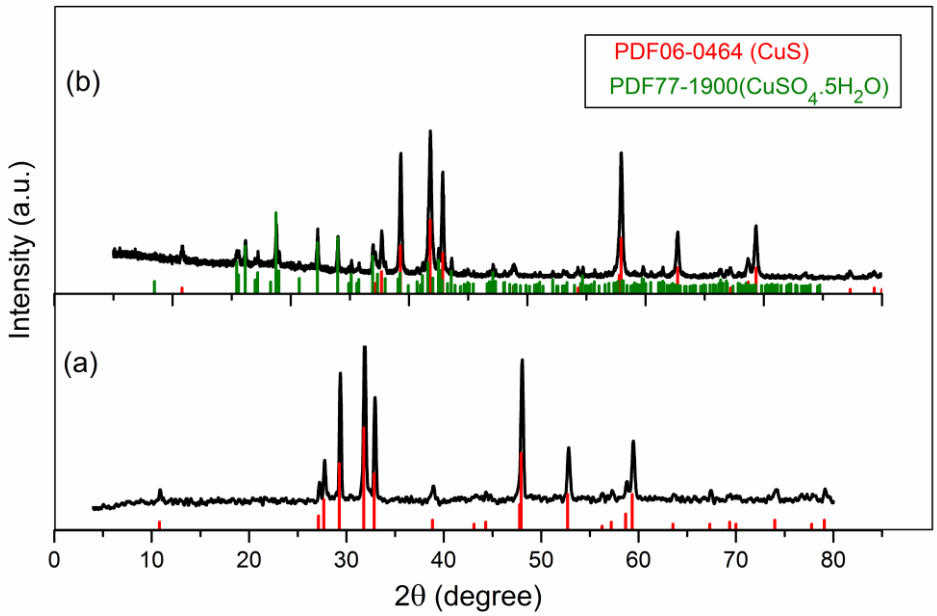

Figure 4.49: XRD patterns of the (a) single phase CuS and (b) phase transformed CuS.

Table 4.15: *Rietveld* quantification analysis for phase pure and phase transformed products.

Sample ID	Description	*Rietveld* quantitative analysis (ICSD)
H05	**Phase Pure CuS**	**100 % CuS (63327)**
-	**Phase transformed CuS**	**67 % CuS (36155)** **33 % $CuSO_4$. $5H_20$ (4305)**

EDX analysis has been done on two different spots and three main areas of the phase transformed sample. The FESEM images of the spots and areas captured were shown in **Figure 4.51**. **Figure 4.52** illustrates the atomic percentage of different element found in the spots and areas of the phase transformed sample. Overall, three main elements were found from the scans, *i.e.* copper, sulfur, and oxygen. Spot A consists of relatively same amount of copper and sulfur, which is ~ 40 % of the total atomic percentage. While oxygen element makes up the remaining atomic percentage (18.78 %) in spot A. Similarly, copper and sulfur elements have a fairly similar atomic percentage in spot B, *i.e.* 25 and 27.65 % respectively. The atomic percentage of oxygen in spot B (47.35 %) is the highest among all the spots and areas involved. For area C and D, quite alike atomic percentage of copper and sulfur are also observed. About 45 atomic percent is reported for copper and sulfur in area C, while about 37 % is found for copper and sulfur in area D. Meanwhile, the oxygen content in both area C and D is moderately high, which is 10.16 % and 26.29 % respectively. The copper element constitutes ~ 37 % and sulfur comprises of ~ 46 % in area E, whereas the oxygen content in area E is ~ 17 %. When the aforementioned EDX results of this phase transformed CuS are compared to the phase pure CuS, it can be seen that no oxygen content is found for phase-pure CuS. This proves that the phase-pure CuS has been oxidized when the EDX analysis was done after 6 months of synthesis.

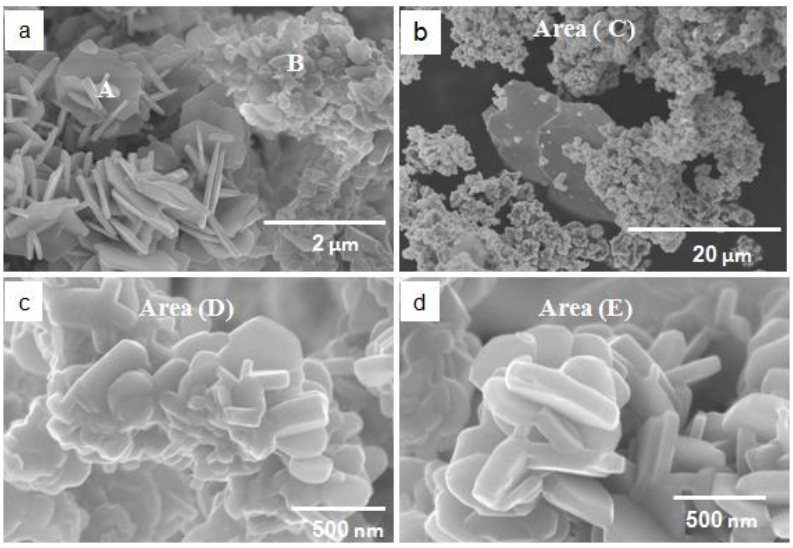

Figure 4.50: FESEM images of phase transformed CuS[†].

[†]The corresponding EDX spectra are attached in Appendix K.

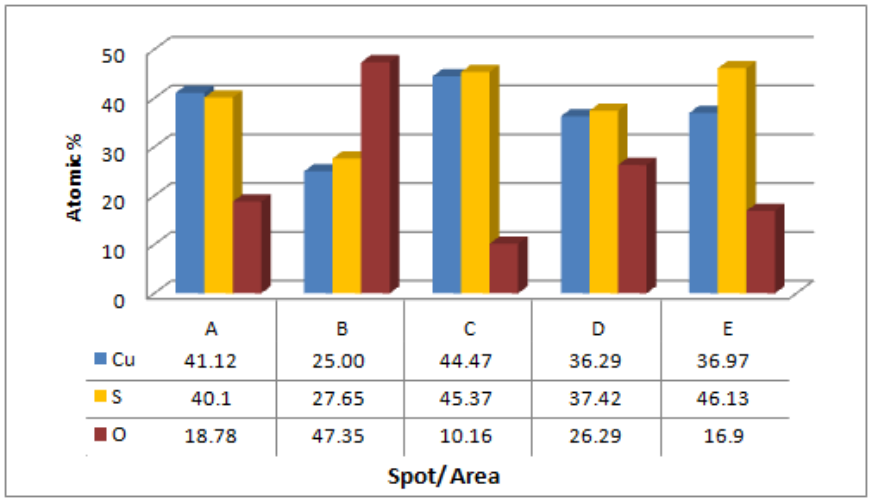

Figure 4.51: EDX analysis on different spots and areas of the phase transformed sample.

Prior to the information from the changes in crystal structure and elemental composition, thermalgravimetric analysis (TGA) was run to examine the deactivated sample under inert atmospehere. **Table 4.16** tabulates the details analysis of DSC thermogram. **Figure 4.52** exhibits TGA-DSC curves of the phase transformed copper sulfide which was subjected under heat treatment up to 773 K in 100 % Ar gas. **Figures 4.53** and **4.54** illustrate the DTG curve and MS results of this sample in inert atmosphere.

Table 4.16: Transition temperature (T_{onset} & $T_{midpoint}$), and enthalpy of phase transformed CuS extracted from DSC curve at inert atmosphere.

Sample	1st Transition		2nd Transition		3rd Transition	
	T_{onset} & $T_{midpoint}$ (K)	ΔH (J/g)	T_{onset} & $T_{midpoint}$ (K)	ΔH (J/g)	T_{onset} & $T_{midpoint}$ (K)	ΔH (J/g)
Phase transformed CuS in inert atm	T_{on}= 428 T_{mid} =438	-9.622 (endo)	T_{on}= 569 T_{mid} =591	-3.169 (endo)	T_{on}= 670 T_{mid} =712	-12.473 (endo)

It can be seen that the phase transformed CuS has undergone a quite similar thermal decomposition compared to phase pure CuS in inert atmosphere, except the facts that the liberation of SO_x gaseous products was detected and the shifts of DSC endothermic peaks in phase transformed CuS. In general, the stepwise decomposition of this material in inert atmosphere involved three major steps. For phase transformed CuS, the stepwise decomposition included loss of moisture, loss of crystallization water, thermal decomposition with the formation of gaseous products and mixture of coexisting CuS, CuO and $CuSO_4$ compounds. The first mass loss occurred at 303-512 K is due to the loss of moisture and crystallization water which accounted for 1.77 % from the total mass loss. This is confirmed by the Mass Spectroscopy (MS) result whereby a broad and a sharp peak of mass-to-charge ratio (m/z 18- H_2O) corresponding to water species (**Figure 4.54**) were detected at 337 and 437 K. This mass loss can be related to the evaporation of moisture at 337 K, and loss of crystallization water at 437 K. The second effect at 513-626 K with 7.76 % of mass loss can be related to the decomposition of the sample to form gaseous products. This is further evidenced by the MS results where two broad peaks of m/z 48- SO and m/z 64- SO_2 were identified at 591 K. The detection of the SO and SO_2 from the MS result indicates that the sample might consist of sulfate compounds which decomposed into

SO_x gaseous products when heating in inert atmosphere. In contrast, this cannot be observed in thermal decomposition of phase pure CuS under inert atmosphere. The third mass loss happened at 626-734 K can be related to the decomposition of the phase transformed CuS into copper deficient compound. For instance, *anilite*, *digenite*, *djurleite* and *etc*. which have been discussed previously in **section 4.4.1 (d)**. It can be seen from the DSC curve where an endothermic event has taken place with a large well-defined peak arose at 712 K. None of any mass spectrum arises at the third mass loss, indicating that no gaseous product was evolved at this stage. All these three stages have accounted for a total mass loss of 19.84 %. From the view of DTG or DSC in **Figures 4.52** and **4.53**, the three major mass loss of the phase transformed CuS heating in inert atmosphere produce an endothermic effect.

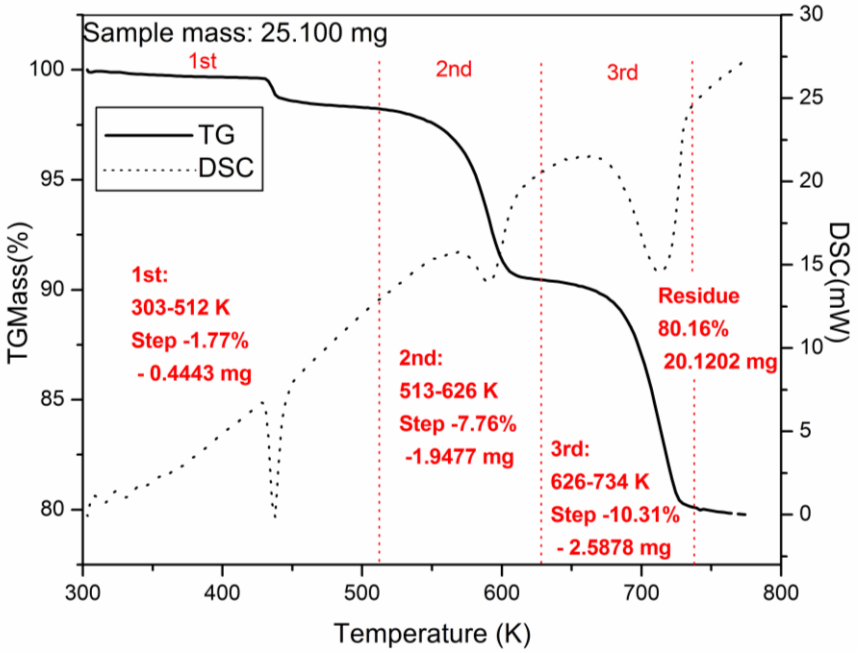

Figure 4.52: TGA-DSC curves of phase transformed CuS in 100 % Ar heated up to 773 K at 5 K/ min with flow rate of 100 mL/ min.

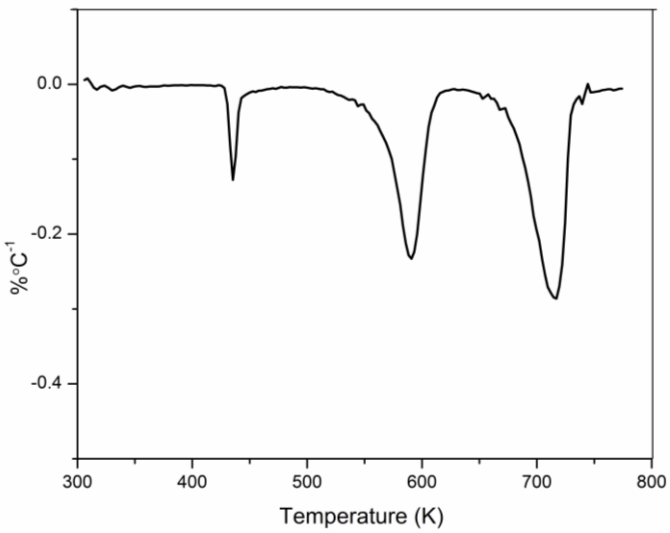

Figure 4.53: DTG curve of phase transformed CuS in 100 % Ar heated up to 773 K at 5 K/min with flow rate of 100 mL/ min.

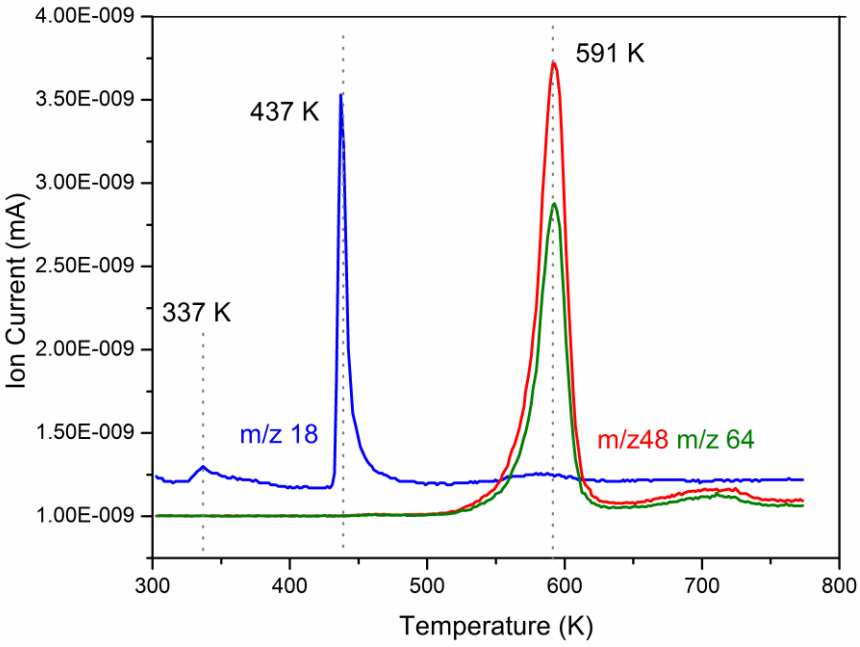

Figure 4.54: Evolution of compounds observed by mass spectroscopy with respect to the mass-to-charge ratio (m/z) for phase transformed CuS in 100 % Ar heated up to 773 K at 5 K/ min with flow rate of 100 mL/ min.

4. 5. 2 Phase Stability Studies of CuS over Time

In the preceding section, the single phase *covellite* was found to undergo a phase transformation process where various techniques, such as PXRD, EDX, TGA-MS/ DSC have proven that it has been transformed to a mixed phase of *covellite* and pentahydrate copper sulfate. Hence, a detailed investigation was carried out to study the phase stability of the as-prepared phase pure *covellite* with time. There were total of four experiments being done to investigate the effects of various parameters (oxygen, moisture, and temperature) towards the phase stability of covellite with time.

The powder PXRD profiles of the *covellite* sample drying at 50 °C, for 6 hours in the furnace are depicted in **Figure 4.55**. After the 1st week, the diffractogram indicates that the sample fits well with hexagonal phase covellite (CuS) which can be indexed to PDF 06-0464. No other sign of impurity can be observed from the diffractogram, implying high purity of the crystal compound formed. However, the as-obtained sample which can be recognized as hexagonal *covellite* (PDF 06-0464) initially was discovered to transform to a phase mixture of *covellite* and pentahydrate copper sulfate (assigned with asterisks) after 4 weeks. The characteristic peaks of pentahydrate copper sulfate (PDF 77-1900) become more intense after 12 weeks, indicating that a more pronounced amount of pentahydrate copper sulfate has been developed on the sample when compared to the sample after 4 weeks. There are several reasons being identified for this rapid transformation process. The drying process in the non-vacuum furnace reflects that the oxygen which present in the air might aid in oxidizing the sulfide to sulfate compound. In addition, the drying temperature of 50 °C is not high enough to eliminate the crystallization water which is still trapped in the sulfide compound. The TGA-MS analysis of phase pure *covellite* heating in oxidative

environment, which has been demonstrated in the previous section, provides an idea that crystallization water can only be removed at 370 and 535 K. This underlines the point that water of crystallization is still found in the crystalline framework of *covellite* and might contribute to the phase transformation process. Moreover, the drying temperature might also help in accelerating the phase transformation process of *covellite* to copper sulfate compound. This can be explained in the viewpoint of thermodynamics where *Gibbs free energy* can be defined as (Atkins & Paula, 2002):

$$\Delta G = \Delta H - T\Delta S$$

Since the phase transformation of *covellite* to copper sulfate is an oxidation process which has been identified as an exothermic event (as discussed in **Section 4.4.1d** Thermal Stability), therefore ΔH in this case is a negative value. Therefore, as the temperature increases, ΔG becomes more negative which implies that a more feasible reaction is taking place. In this experiment, the phase transformation can also be linked to kinetic phenomena where at elevated temperature, the system is able to react which leads to the formation of $CuSO_4$ nuclei. For the period of 1^{st} week, the $CuSO_4$ nuclei were too little to be detected by PXRD; however, the phase transformation was then promoted by the existence of these growing nuclei under ambient conditions.

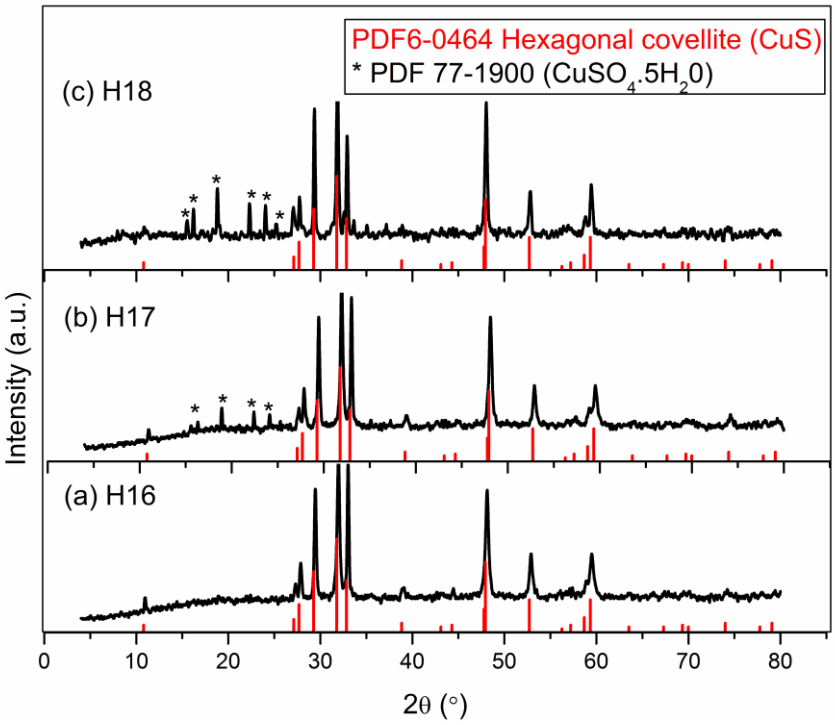

Figure 4.55: PXRD profiles of products dried in furnace after period (a) 1 week (b) 4 weeks (c) 12 weeks

Continued from the previous experiment, the following sample was prepared with a slightly different method whereby the sample was washed with deionized water and ethanol for several times before drying in the vacuum desiccator. The PXRD patterns of the products recovered at different time intervals are displayed in **Figure 4.56**. After a week, the sample was found to be a single phase *covellite* in which all the respective peaks of the sample can be corresponded to PDF 06-0464, hexagonal *covellite*. The similar patterns were detected for the sample after 4 weeks. However, it can be seen that extra peaks which can be arising from pentahydrate copper sulfate (PDF 77-1900), were identified for sample stored after 12 weeks. It is initially believed that the use of ethanol in the washing procedure might aid in drying process of the sample. However, the presence of a mixed phase compound after 12 weeks indicates that there is a possibility where there is still crystallization water which was trapped within the sulfide compound. This crystallization

water cannot be eliminated easily and oxidization mechanism is most likely dependent on the presence of water. It might happen because of the diffusion of moisture and oxygen in the air onto the surface of CuS. This again points out that the washing method might not be suitable to compensate the attack of moisture and oxygen towards the sample.

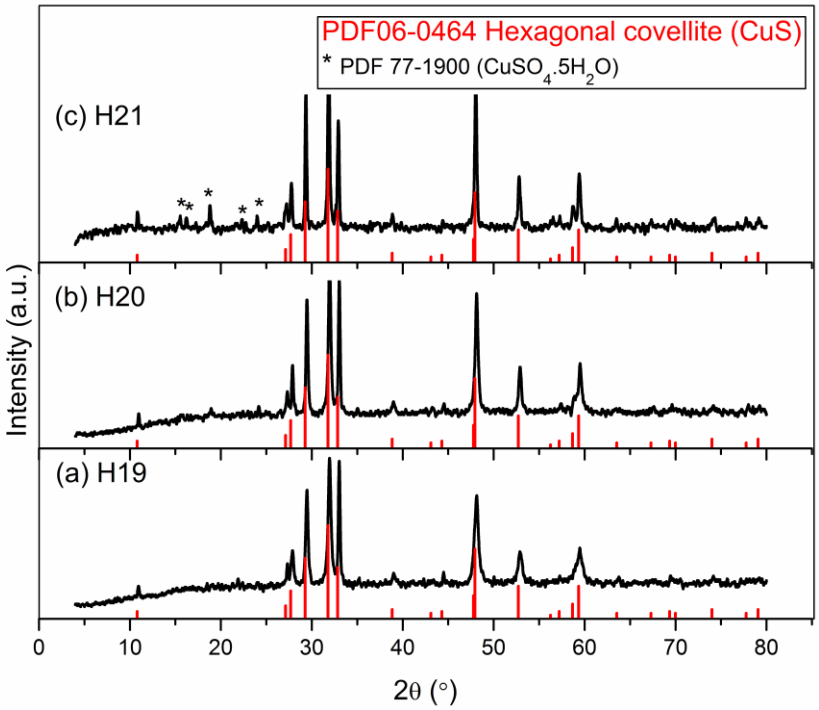

Figure 4.56: PXRD profiles of products washed with deionized water and ethanol after period (a) 1 week (b) 4 weeks (c) 12 weeks

The third experiment was the control study whereby the synthesized products was washed with batches of deionized water and dried in the vacuum desiccator without purging of nitrogen gas. After that, the products were stored in a cool and dark place for different time intervals. **Figure 4.57** shows the PXRD profiles of the products after 3 different time intervals, *i.e.* 1 week, 4 weeks, and 12 weeks. It can be observed from the PXRD profiles that all the salient peaks of the products prepared after 1 week and 4 weeks can be indexed to PDF 06-0464, hexagonal *covellite*. No other trace of crystalline impurity

was found. However, additional peaks which can be indexed to PDF 77-1900, pentahydrate copper sulfate, were observed after 12 weeks. This indicates that the phase pure *covellite* was degraded to a mixed-phase of *covellite* and pentahydrate copper sulfate after time interval of 12 weeks. With this experiment, it can be proven that the sample prepared employing this method is stable up to 4 weeks. After 12 weeks, it is believed that the moisture (from the air or the crystallization water might still present in the sample) has led to the phase transformation process whereby partial amount of copper sulfide was oxidized to form copper sulfate. Nevertheless, the rate of conversion of CuS to the mixture of CuS and $CuSO_4$ is very likely to be dependent on the storage conditions of the sample. The rate of transformation will be higher for the storage condition with higher humidity.

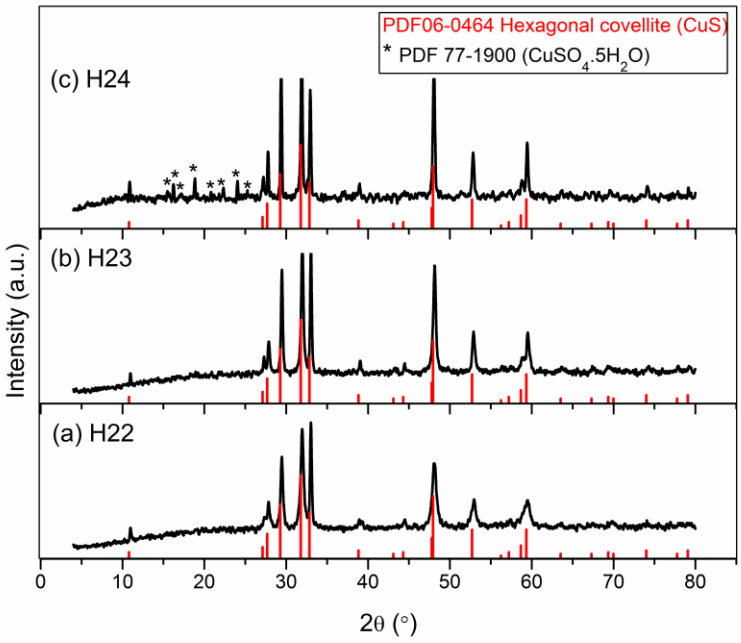

Figure 4.57: PXRD profiles of products under control study without purging of nitrogen gas after period (a) 1 week (b) 4 weeks (c) 12 weeks

On the contrary, another experiment was carried out as per the control study, but with additional nitrogen purging storage step. The additional step was done by purging the sample with purified nitrogen gas for 3 minutes before storage in the cool and dark place.

The PXRD patterns of the sample are illustrated in **Figure 4.58**. It can be noted that all the characteristic peaks can be well-fitted to PDF 06-0464, hexagonal *covellite*, and none of the crystalline impurity peaks was detected from the entire patterns. A very crucial point to be highlighted here which is the single phase *covellite* has not transformed to any other phase after 12 weeks, therefore we have extended the time intervals to 24 weeks. Interestingly, the sample exhibits the similar PXRD pattern and this again confirms that it is of a single phase hexagonal *covellite* as no additional peak arising from other compound. This experiment signifies that the purging of nitrogen gas on the sample is vital to prevent the sulfide compounds from further attack by moisture or oxygen in the environment. It can be understood that purging of purified nitrogen gas onto the sample provides a nitrogen blanket to avoid and eliminate the sample from the attack of moisture or oxygen. Consequently, the sample which was stored with nitrogen gas is proven to be the most efficient storage method among the others. The sample is stable and does not transform or oxidize to any other compound.

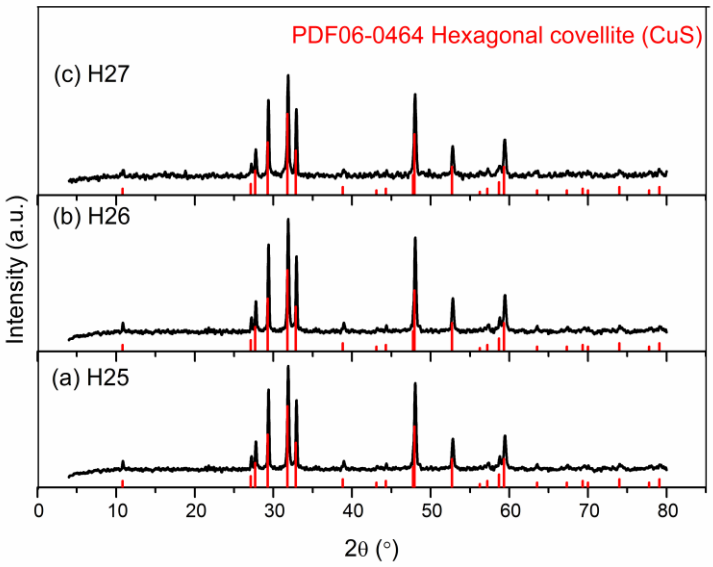

Figure 4.58: PXRD profiles of products under control study with purging of nitrogen gas after period (a) 1 week (b) 12 weeks (c) 24 weeks

4. 5. 3 Discussion

Covellite is well known as a stable compound among the other phases in copper sulfide family at room temperature. However, this phase pure *covellite* is found to transform into a mixed phase of *covellite* and pentahydrate copper sulfate after 6 months in our recent studies. This finding is strongly supported by the results from various techniques such as PXRD, EDX, and TGA-MS being done on the phase transformed sample which was initially a phase pure sample. From the discussion in the preceding section, PXRD has confirmed that a mixed phase of pentahydrate copper sulfate and *covellite* is present on the phase transformed sample. The EDX analysis done on various spots and areas on the phase transformed sample has indicated that oxygen element is found to present in large amount in the phase transformed sample in which it was not detected on a phase pure sample initially. Besides that, the detection of gaseous products such as sulfur monoxide (SO) and sulfur dioxide (SO_2) with their corresponding m/z values in the MS peaks during the heating of phase transformed sample in inert atmosphere has strongly pinpointed that the phase pure *covellite* was transformed to a phase mixture of *covellite* and pentahydrate copper sulfate.

To the best of our knowledge, to date, no systematic study has been done to investigate the stability of *covellite* over time. Therefore, in this present work, the phase stability study of *covellite* over time was carried out to find out the most suitable way to prepare and store *covellite* besides to identify that how stable is the material towards oxidation with time at ambient condition.

When most of the sulfide compounds are exposed to an oxidizing environment, the materials become chemically unstable. Majority of the sulfides are generally stable under

strongly reducing conditions, but the exposure of these materials to oxidizing conditions will destabilize them, and the sulfides will be destroyed via various oxidation mechanisms. The oxidation mechanisms of sulfides are analogous to those of pyrite but the reaction rates might be different. Sulfides such as *pyrite* (FeS_2), *marcasite* (FeS_2), *pyrrohotite* ($Fe_{1-z}S$), and *mackinawite* ($(Fe,Ni)_{1+x}S$) appear to be the most reactive sulfides, while other sulfides such as *covellite* (CuS), *millerite* (NiS) and *galena* (PbS) are commonly far less reactive than pyrite. This is because of the greater stability of their crystal structure and the lack of iron released from these less reactive sulfide compounds. On the other hand, sulfide compounds such as *cinnabar* (HgS) and *molybdenite* (MoS_2) are the least reactive sulfides. They are more resistant and persistent in oxidic environment (Lottermoser, 2010).

Since the oxidation mechanism is similar for all the sulfide compounds, a few factors which affect the *covellite* oxidation can be recognized as suggested with reference to the *pyrrhotite* oxidation. The first factor discussed on this particular topic is the crystal structure of the sulfide material. Various studies suggested that surface roughness and extended fractures can be associated to the susceptibility of sulfides to the oxidation processes (Belzile, Chen, Cai, & Li, 2004). A few research groups have suggested that the crystal structure of *pyrrhotite* can affect its oxidation rate. (Orlova, Stupnikov, & Krestan, 1989; Yakhontova, Nesterovich, & Grudev, 1983) On the contrary, no apparent correlation between *pyrrhotite* oxidation and its crystal structure was reported by *Janzen et al., 2000*. (Janzen, Nicholson, & Scharer, 2000) An unpublished result by *Belzile et al.* has indicated that monoclinic *pyrrhotite* could be less reactive than the hexagonal form. For *covellite*, with its hexagonal closed packed and covalently bonded layers of sulfur structure, we believe that it has a more stable crystal structure in relative to pyrite which is more vulnerable to the phase transformation process.

In addition, oxygen and moisture can also play a determining role in the oxidation process of sulfide compounds. Oxygen is the ultimate oxidizing agent for sulfides in environments where dissolved or gaseous oxygen is present. The oxidation process of *covellite* can proceed as follow:

$$CuS + O_2 + 2H_2O \rightarrow Cu^{2+} + SO_4^{2-} + 4H^+ + 4e^-$$

From our studies, *covellite* which was washed with deionized water and prepared with purging of nitrogen gas before storage in vacuum desiccator is found to be the best and most suitable method in preparing and storing the sulfide compound. In this particular experiment, the phase pure *covellite* has not transformed or oxidized to its oxide or sulfate compound even after 24 weeks. Meanwhile, the experiments which involve the different washing methods-deionized water; deionized water and ethanol respectively have demonstrated that the as- prepared *covellite* are stable up to 4 weeks. After 12 weeks, both of the samples have been transformed to a mixed phase of *covellite* and pentahydrate copper sulfate. The water molecule which is present in the sample or environment might have dissolved oxygen which can perturb the surface crystalline framework of *covellite*, resulting in the oxidation process occurring at the pseudo-liquid phase of the sulfide compound. Although *covellite* is well known for its stability at room temperature, we believe that the degradation of *covellite* is a kinetic process which depends on various experimental conditions in influencing the speed of phase transformation. The drying of *covellite* in vacuum desiccator at room temperature is not adequate to provide a thorough drying process in order to eliminate the water of crystallization in *covellite*. This can be explained with the TGA-MS analysis where m/z of water was found at 72 and 237 °C during the thermal oxidation of *covellite*. This means that the sulfide compound tends to react with the water of crystallization which is trapped in the *covellite* framework and

involve in the bond arrangement to become copper sulfate after a period of time. The oxidation of sulfide to sulfate compound is a simple redox process as represented by the following equation where the oxidation number of S has been changed from -2 to +6:

$$CuS + 2O_2 \rightarrow CuSO_4$$

Hence, it is remarkable that there is a direct correlation between the increase of oxidation rate with the growing relative humidity and concentration of oxygen in the environment where sulfides are stored.

On the other hand, *covellite* which was washed with deionized water and further drying at 50 °C for 6 hours in the furnace has been oxidized after 4 weeks. This can be considered the most discontented method among the other methods in preparing and storing the sulfide compounds as the *covellite* has experienced the most rapid phase transformation process. According to the previous work reported by *Williamson and Rimstidt, 1994* (Williamson & Rimstidt, 1994), *pyrrhotite* oxidation is a temperature dependent process which follows *Arrhenius* behavior. Prior to this discovery, *Stegar, 1982* (Steger, 1982), has found that an increase in temperature of *pyrrhotite* oxidation process can enhance the rate of oxygen diffusion and therefore lead to the formation of ferric oxide and ferric sulfate products. In our investigation, we found that the oxidation rate of *covellite* have been accelerated at elevated temperature with the formation of copper sulfate compound at the shortest time interval compared to other preparation methods. Furthermore, the elevated drying temperature in this experiment also speeds up the oxidation process according to the discussion based on the thermodynamics viewpoint. This underlines the fact that temperature has a pronounced effect in *covellite* oxidation.

Nevertheless, the oxidation mechanism involve in the oxidation of covellite cannot be totally elucidated in this study as more sophisticated X-ray techniques such as electron

(XES), photoelectron (XPS), and Auger electron spectroscopy (AES) are required to determine the species present during the oxidation process before any oxidation mechanism is proposed.

As a result, an appropriate handling and storage procedure for *covellite* (inclusive of other sulfide compounds) should be put into practice to avoid any unnecessary degradation of the sample. One possible approach of preventing the contact between *covellite* and oxygen or moisture is via the purging of N_2 or Ar gas before storage which is proven to be efficient as recommended in this study. Another logical way of limiting the contact between the sulfide compounds with oxygen or moisture is by adopting different types of dry and organic covers like clay, soil, peat, hay, straw, sawdust, sludge or compost that can prevent oxygen diffusion as suggested by *Belzile et al., 1997*; *Nicholson et al., 1989*; and *Blowes et al., 1994* (Eyles, 1997; Jambor & Blowes, 1994; Nicholson, Gillham, Cherry, & Reardon, 1989). Besides that, sulfides can also be stabilized with the addition of a binder (cement), neutralizers, bactericides or surfactants (Amaratunga, 1991; Hmidi & Amaratunga, 1998). On top of that, the oxidation of sulfides can be partially or totally inhibited through surface treatments with coating agents as suggested by *Lalvani et al., 1990, 1991*; *Belzile et al., 1997*; *Lan et al., 2002* (Belzile, Maki, Chen, & Goldsack, 1997; Lalvani, DeNeve, & Weston, 1990; Lalvani, DeNeve, & Weston, 1991; Lan, Huang, & Deng, 2002).

CHAPTER 5

CONCLUSION & RECOMMENDATIONS

5. 1 Concluding Remarks

The focus of this research study was to develop an adsorbent material which is capable of trapping mercury in aqueous system in response to the current worldwide mercury contamination contributed by both from natural and anthropogenic sources. The study on the synthesized adsorbent which encompasses the structural, chemical, and thermal properties was conducted. These are important as to give insight and understanding on the behavior of this potential adsorbent in reducing and controlling the mercury-related pollution issues.

In this current study, 2 phase pure copper sulfides (*digenite*- Cu_9S_5, and *covellite*-CuS) were successfully prepared without the aid of any assisting agent (organic solvent, acid, base, and surfactant) via hydrothermal route. Both of these copper sulfides were fabricated under the conditions of 12 hours at 155 °C with *digenite* formed at 1: 1.5, while *covellite* synthesized at 1: 2 Cu: S mole ratio. The phase pure identity of these copper sulfides has been proven by a series of characterization tools, namely PXRD, EDX, XRF, and TEM. PXRD has confirmed that hexagonal phase *covellite* with PDF 06-0464 was identified for product synthesized at Cu: S mole ratio of 1: 2, 155 °C for 12 hours, whilst it was identified as rhombohedral phase *digenite* with PDF 047-1748 for product synthesized at Cu: S mole ratio of 1: 1.5, 155 °C for 12 hours. Furthermore, the chemical analyses done on these phase pure products by employing XRF and EDX techniques indicate that both of these products are in good correlation with the PXRD results. The Cu: S mole ratio calculated from XRF and EDX showed values of 1: 1.04 and 1: 1.07 respectively for

covellite, while 1: 0.64 and 1: 0.56 for *digenite*. On the other hand, the structural and thermal behaviors of the phase pure products were further studied with FESEM, BET and TGA-MS/ DSC techniques. From FESEM, phase pure *covellite* exhibited distinctive hexagonal shape nanoplates which were arranged perpendicular to each other. Circular nanoplates were observed for phase pure *digenite* under the electron microscope. Both of these products were found to be highly agglomerated, therefore making the precise particle size measurement not viable in this case. The surface area, total pore volume, and average pore size of the phase pure copper sulfides were determined by BET analysis. The results revealed that the surface area of the synthesized phase pure *covellite* and *digenite* were 15 and 3 m^2/ g respectively. The total pore volume were determined as 2.882×10^{-2} and 1.417×10^{-2} cm^3/ g, while the average pore size were calculated to be 7.63 and 20.58 nm for *covellite* and *digenite* respectively. Both of the phase pure materials can be regarded as practically non-porous, particularly that for *digenite*. Porosity is developed for *covellite* due to its perpendicular arrangement of the hexagonal platelets. It is expected that *covellite* would benefit for its fluid flow and low pressure drop as the hexagonal platelets would generate loose packing for voidage.

Three synthesis parameters have been systematically investigated during the formation of copper sulfides. These 3 parameters (synthesis temperature, Cu: S mole ratio, and synthesis time) were found to have pronounced effects in determining the phase purity, crystal phase, morphology, and crystallite size of the final products formed. Synthesis temperature and Cu: S mole ratio are found to play a vital role in determining the phase purity, crystallography and morphology of the products synthesized, while synthesis time has pronounced effects on the crystallite size of the final products formed. All the products fabricated at different synthesis parameters were well-characterized with PXRD, SEM,

EDX, and XRF techniques. In addition, systematic study on the crystal growth mechanism over a series of synthesis temperature was also carried out. Several mechanistic pathways leading to the final formation of *covellite* was proposed and 4 species ($S_2O_3^{2-}$, $S_4O_6^{2-}$, SO_4^{2-}, and S^{2-} species) were proposed to be responsible for the formation of *covellite*.

In addition, the thermal analysis done on *covellite* and *digenite* disclosed that these materials are of phase pure identity due to the absence of certain phases (sulfate or oxide) during heating in inert atmosphere. On the other hand, these two materials underwent exothermic reaction in oxidic atmosphere and the thermal oxidation of these two materials involves primarily 3 steps: loss of moisture and solvated water, decomposition to other copper sulfide compounds, and oxidation of sulfide compounds to form copper oxide, copper sulfate or mixture of these two compounds.

Most importantly, a preliminary study done on assessing the potential ability of CuS in removing mercury in aqueous system has proven that the as- synthesized CuS has good potential in trapping Hg(II) in aqueous system. In this performance testing experiment, only *covellite* was subjected for the subsequent assessment as *covellite* is renowned as the most stable form in copper sulfides family. From the sorption isotherm fitting results and experimental sorption data, it was found that the experimental data fitted well with Langmuir isotherm and the sorption of Hg(II) onto CuS in aqueous system are favored in a wide range of pHs. This shows that the synthesized CuS is applicable to remove mercury in aqueous system particularly at acidic pH and this has successfully achieved the goal of this research study.

Covellite is well known for its stability at room temperature over the entire copper sulfides family. Unexpectedly, the as-synthesized phase pure covellite was found to transform to a mixed phase of *covellite* and pentahydrate copper sulfate after a certain

period. This discovery was supported with various observations from PXRD, EDX, and TGA-MS techniques. From PXRD, additional crystal phase which can be indexed to PDF 77-1900, pentahydrate copper sulfate ($CuSO_4.5H_2O$) was found on the phase transformed sample. This was further confirmed by *Rietveld* quantification analysis where phase mixture of 67 % CuS and 33 % $CuSO_4.5H_2O$ was determined from the phase transformed sample after 6 months. This was followed by EDX analysis where O element was found besides Cu, and S elements on the different spots and areas of the phase transformed sample. Some of the spots and areas even exhibited high atomic percentage of O element. Moreover, TGA-MS analysis performed on phase transformed sample indicated that water molecule, sulfur monoxide, and sulfur dioxides were present when the sample was subjected for heating under inert environment. This designated the presence of sulfate on the phase transformed sample which was in good agreement with the PXRD, and EDX analysis. Thus, a phase stability study was carried out to investigate the most suitable way to prepare and store *covellite* besides to find out the stability of *covellite* over time at ambient condition. It was discovered that *covellite* with the common washing and storage method described in the research methodology section was stable up to 4 weeks, but oxidized to a mixed phase of *covellite* and pentahydrate copper sulfate after 12 weeks. Three factors have been recognized to have contributed to the degradation of phase pure *covellite* at ambient condition, namely humidity, oxidic condition, and elevated drying temperature. However, a promising method to prevent the phase transformation of *covellite* was introduced to combat with the aforementioned factors. *Covellite* with the purging and blanketing of nitrogen gas before storage are found to be the best method in preserving *covellite* from further oxidation.

In a nutshell, a complete coverage from the effects of 3 synthesis parameters (synthesis temperature, Cu: S mole ratio, and synthesis time), structural and chemical properties of phase pure copper sulfides, preliminary performance testing of *covellite*, as well as the phase stability studies of *covellite* have been summarized in this Section. The suggestion for future work is disclosed in the next Section.

5. 2 Recommendations

A few drawbacks were recognized for the properties of the copper sulfides synthesized which include low surface area and stability issues. Most of the copper sulfides prepared were of low surface area compared to other porous materials like zeolite, carbons, and etc. Modifications can be made to achieve higher surface area in this material and the discussions are disclosed below. On the other hand, since most of the naturally occurrence sulfides are not stable to air humidity at ambient condition; copper sulfide faces the same stability issue. Hence, there are still many research opportunities in this particular research discipline.

For hydrothermal synthesis, there are a few modifications on the synthesis parameters can be done as suggested in the following:

- **Different copper sources** (elemental copper, copper (II) sulfate, copper (II) carbonate, copper (II) chloride, copper acetate, copper citrate, copper oxalate, and etc.) may control the crystal phase, morphology, and the textural properties of the product synthesized.
- **Different sulfur sources** (elemental sulfur, sodium sulfide, potassium sulfide, sodium tetrasulfide, potassium tetrasulfide, and etc.) may influence the crystal phase, morphology, and the textural properties of the final product formed.

- **Different assisting agents** (ethanol, ethylene glycol, aqueous ammonia, surfactants, and etc.) may affect the textural properties, particle size and surface area of the copper sulfides formed.

By varying the synthesis parameters as stated above, it can be expected that copper sulfides with different structural, chemical, and thermal properties can be produced. Moreover, further characterization analysis can be done on the phase pure samples, such as X-Ray Photoelectron Spectroscopy (XPS). The elemental and chemical state compositions can be determined in the top 30 Å. A more precise determination of the type of species present in the sample can be made directly from the kinetic energies of the ejected photoelectrons (Brundle, et al., 1992).

With respect to the goal of this research study which is to develop an adsorbent for mercury removal in aqueous system, the design and the preparation of the materials with the most effective size and surface area are prominent. The main critical aspect in the design of CuS adsorbent for mercury removal in aqueous system is the surface area of the particular powder since the experimental data fitted well with the Langmuir isotherm. This reflects that the sorption of Hg(II) onto CuS follows the Langmuir manner where a monolayer sorption will be reached upon the reaction equilibrium. Therefore, two approaches are discussed in the later part in order to enhance surface area of CuS for optimized mercury removal efficiency.

First, the surface area of CuS can be enhanced by reducing the particle size of the synthesized material at nano-sized range. This can be achieved by template synthesis through hydrothermal route. A more aligned, less agglomerated distribution of particle can be produced by using surfactants such as sodium dodecyl sulfate (SDS), 4-dodecylbenzenesulfonic acid (SDBS), cetyl trimethyl ammonium bromide (CTAB), and so

on. With template synthesis, narrow particle size ranged, nano-sized and higher surface area material can be obtained. Besides that, the desired material can also be prepared through precipitation method by controlling the synthesis parameters which include reaction temperature, pH, aging, and so on.

Another approach for attaining higher surface area property can be done by introducing support to the as-prepared CuS. The support material can be alumina or silica which is of high surface area. The silica can be produced by sol-gel process, precipitation or flame hydrolysis. Different types of silica can be produced with the aforementioned methods. For instance, silica gel can be produced by sol-gel process, precipitated silica is generated from precipitation method, while fumed silica is fabricated from flame hydrolysis technique. On the other hand, active aluminas are widely applied in most of the catalytic reactions compared to silicas as they are not only excellent support materials, yet active as catalysts in some reactions. Porous aluminas are manufactured by a controlled dehydration from aluminium hydroxide or aluminium oxide hydrates (Ertl, Knözinger, Schüth, & Weitkamp, 2008). With the supported system introduced to the CuS adsorbent, the surface area of this new system can be enhanced to maximum. On top of that, the manufacture cost of this supported copper sulfide system in large scale can be reduced as the amount of active material required is lowered with the introduction of supported system.

Last but not least, it is also recommended that the as-prepared copper sulfide should be kept under nitrogen blanket to avoid further degradation or oxidation of this material in the air. With the implementation of the future work suggested as above, it can be assured that further development of this project is viable to combat with the serious environmental problems addressed by mercury issues. Hence, a greener and mercury-free environment can be realistic in this case.